PUBLISHED BY IOP PUBLISHING FOR SISSA MEDIALAB

RECEIVED: *June 19, 2012*
ACCEPTED: *September 10, 2012*
PUBLISHED: *October 5, 2012*

LHC REFERENCE VOLUME

Performance of CMS muon reconstruction in pp collision events at $\sqrt{s} = 7$ TeV

The CMS collaboration

E-mail: cms-publication-committee-chair@cern.ch

ABSTRACT: The performance of muon reconstruction, identification, and triggering in CMS has been studied using $40\,\mathrm{pb}^{-1}$ of data collected in pp collisions at $\sqrt{s}$ = 7 TeV at the LHC in 2010. A few benchmark sets of selection criteria covering a wide range of physics analysis needs have been examined. For all considered selections, the efficiency to reconstruct and identify a muon with a transverse momentum p_{T} larger than a few GeV/c is above 95% over the whole region of pseudorapidity covered by the CMS muon system, $|\eta| < 2.4$, while the probability to misidentify a hadron as a muon is well below 1%. The efficiency to trigger on single muons with p_{T} above a few GeV/c is higher than 90% over the full η range, and typically substantially better. The overall momentum scale is measured to a precision of 0.2% with muons from Z decays. The transverse momentum resolution varies from 1% to 6% depending on pseudorapidity for muons with p_{T} below 100 GeV/c and, using cosmic rays, it is shown to be better than 10% in the central region up to $p_{\mathrm{T}} =$ 1 TeV/c. Observed distributions of all quantities are well reproduced by the Monte Carlo simulation.

KEYWORDS: Performance of High Energy Physics Detectors; Large detector-systems performance; Simulation methods and programs; Particle identification methods; Muon spectrometers; Particle tracking detectors; Particle tracking detectors (Gaseous detectors)

© CERN 2012 for the benefit of the CMS collaboration, published under the terms of the Creative Commons Attribution licence 3.0 by IOP Publishing Ltd and Sissa Medialab srl. Any further distribution of this work must maintain attribution to the author(s) and the published article's title, journal citation and DOI.

doi:10.1088/1748-0221/7/10/P10002

2012 JINST 7 P10002

Contents

1 Introduction **1**

2 Data and Monte Carlo samples **3**

3 Muon reconstruction and identification **6**

4 General comparisons between data and simulation **8**
- 4.1 Classification of muon sources in simulation 8
- 4.2 Kinematic distributions of muons 9
- 4.3 Muon identification variables 13

5 Muon reconstruction and identification efficiency **18**
- 5.1 Muon efficiency using the tag-and-probe method on dimuon resonances 19
  - 5.1.1 Method 19
  - 5.1.2 Results 20
  - 5.1.3 Systematic uncertainties 22
- 5.2 Reconstruction and identification efficiency for nearby muons 24
- 5.3 Muon identification probability for particles other than muons 25

6 Muon momentum scale and resolution **27**
- 6.1 Measurements at intermediate p_{T} 29
  - 6.1.1 Muon momentum scale 29
  - 6.1.2 Muon momentum resolution 33
  - 6.1.3 Momentum resolution of standalone muons 34
- 6.2 Measurements at high p_{T} 35
  - 6.2.1 Muon momentum resolution from cosmic-ray muon data 36
  - 6.2.2 Momentum scale from the cosmics endpoint method 38

7 Background from cosmic-ray and beam-halo muons **39**
- 7.1 Cosmic-ray muons 39
- 7.2 Beam-halo muons 43

8 Isolation **44**

9 Muon trigger **50**
- 9.1 Trigger efficiency using the tag-and-probe method on dimuon resonances 51
  - 9.1.1 Trigger efficiency for Soft Muons 52
  - 9.1.2 Trigger efficiency for Tight Muons 54
  - 9.1.3 Systematic uncertainties 56
  - 9.1.4 Efficiency of online muon isolation requirements 57
- 9.2 Muon trigger efficiencies from jet-triggered samples 57
- 9.3 Trigger rejection rates 62

2012 JINST 7 P10002

10 Conclusions 62

The CMS collaboration 68

1 Introduction

The primary aim of the Compact Muon Solenoid (CMS) Collaboration is to discover physics underlying electro-weak symmetry breaking with the favoured mechanism being the Higgs mechanism. Many diverse experimental signatures from other potential new physics should also be detectable. In order to cleanly detect these signatures the identification and precise energy measurement of muons, electrons, photons and jets over a large energy range and at high luminosities is essential.

In this paper we report on the performance of muon reconstruction, identification, and triggering evaluated using the data collected by the CMS detector at the Large Hadron Collider (LHC) at CERN during 2010. During that period the CMS experiment recorded a sample of events produced in proton-proton collisions at a centre-of-mass energy of $\sqrt{s} = 7\,\text{TeV}$ with an integrated luminosity of 40 pb^{-1}. Muon reconstruction in CMS has been previously studied in great detail using muons from cosmic rays [1, 2]. The first studies using 60 nb^{-1} of 2010 proton-proton collision data were reported in ref. [3].

A detailed description of the CMS detector can be found in ref. [4]. A schematic view of the detector is shown in figure 1. Muon reconstruction is performed using the all-silicon inner tracker at the centre of the detector immersed in a 3.8 T solenoidal magnetic field, and with up to four stations of gas-ionization muon detectors installed outside the solenoid and sandwiched between the layers of the steel return yoke. The inner tracker is composed of a pixel detector and a silicon strip tracker, and measures charged-particle trajectories in the pseudorapidity range $|\eta| < 2.5$.[1] The muon system covers the pseudorapidity region $|\eta| < 2.4$ and performs three main tasks: triggering on muons, identifying muons, and improving the momentum measurement and charge determination of high-p_{T} muons. Drift tube (DT) chambers and cathode strip chambers (CSC) detect muons in the η regions of $|\eta| < 1.2$ and $0.9 < |\eta| < 2.4$, respectively, and are complemented by a system of resistive plate chambers (RPC) covering the range of $|\eta| < 1.6$. The use of these different technologies defines three regions in the detector, referred to as barrel ($|\eta| < 0.9$), overlap ($0.9 < |\eta| < 1.2$), and endcap ($1.2 < |\eta| < 2.4$). Muon energy deposits in the electromagnetic calorimeter (ECAL), hadronic calorimeter (HCAL), and outer hadronic calorimeter (HO) are also used for muon identification purposes. An event in which four muons were reconstructed involving all main CMS subdetectors is shown in figure 2.

For the measurement of muons the single most important aspect is the choice of magnetic field configuration. The requirement of a good momentum resolution, specified to be $\sigma(p_{\text{T}})/p_{\text{T}} \sim 1\%$ at 100 GeV/c and $\sim 10\%$ at 1 TeV/c, without making stringent demands on spatial resolution and the

[1] A right-handed coordinate system is used in CMS, with the origin at the nominal collision point, the x axis pointing to the centre of the LHC ring, the y axis pointing up (perpendicular to the LHC plane), and the z axis along the anticlockwise-beam direction. The pseudorapidity η is defined as $\eta = -\ln\tan(\theta/2)$, where $\cos\theta = p_z/p$. The radius r is the distance from the z axis; the azimuthal angle ϕ is the angle relative to the positive x axis measured in the x-y plane.

2012 JINST 7 P10002

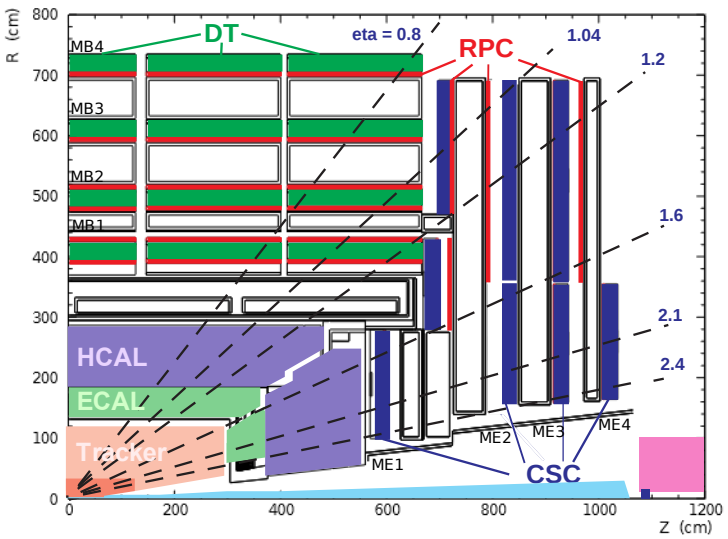

Figure 1. Longitudinal layout of one quadrant of the CMS detector. The four DT stations in the barrel (MB1–MB4, green), the four CSC stations in the endcap (ME1–ME4, blue), and the RPC stations (red) are shown.

alignment of muon chambers leads to the choice of a high magnetic field. CMS chose a high-field solenoid. The magnetic flux generated by the central field is large enough to saturate a sufficient amount of steel in the return yoke to allow the installation of four muon stations. This provides a good level of redundancy in the measurement of muons. The favourable length to radius ratio allows efficient muon measurement up to pseudorapidity of $|\eta| < 2.4$. The strong magnetic field also enables an efficient first-level trigger with an acceptable rate.

The CMS experiment uses a two-level trigger system. The Level-1 trigger, composed of custom hardware processors, selects events of interest using information from the calorimeters and muon detectors and reduces the read-out rate from the 20 MHz bunch-crossing frequency to a maximum of 100 kHz [5]. The high-level trigger (HLT) is software-based and further decreases the recorded event rate to around 300 Hz by using the full event information, including that from the inner tracker [6].

Several types of triggers implemented for the 2010 data taking have been used for the present studies. These are discussed in section 2, together with the resulting data and simulated samples. Muon reconstruction and identification algorithms are described in section 3. The measured distributions of various kinematic variables of selected muons are compared with simulation in section 4. Section 5 presents muon reconstruction and identification efficiencies for exclusive samples of prompt muons, kaons, pions, and protons. Section 6 summarizes the results on muon momentum scale and resolution for different muon momentum ranges. Backgrounds from cosmic rays and beam-halo muons are discussed in section 7. Section 8 describes the performance of different isolation algorithms. Muon trigger performance is discussed in section 9. Section 10 gives a summary of our conclusions.

2012 JINST 7 P10002

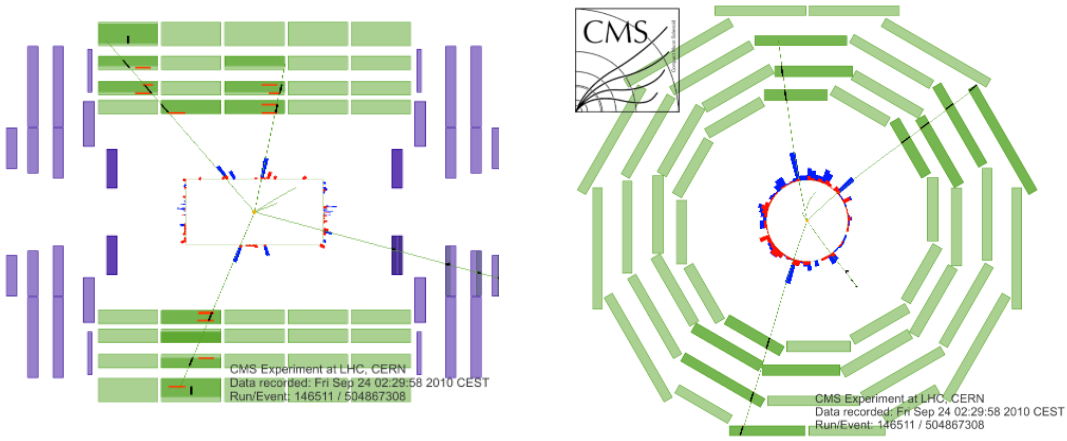

(a) (b)

Figure 2. (a) The longitudinal (r-z) and b) the transverse (r-ϕ) views of a collision event in which four muons were reconstructed. The green (thin) curves in the inner cylinder represent tracks of charged particles reconstructed in the inner tracker with transverse momentum $p_{\mathrm{T}} > 1\,\mathrm{GeV}/c$; those extending to the muon system represent tracks of muons reconstructed using hits in both inner tracker and the muon system. Three muons were identified by the DTs and RPCs, the fourth one by the CSCs. Short black stubs in the muon system show fitted muon-track segments; as the z position is not measured in the outer barrel station, the segments in it are drawn at the z centre of the wheel, with their directions perpendicular to the chamber. Short red (light) horizontal lines in the r-z view indicate positions of RPC hits; energy depositions in the ECAL and HCAL are shown as red (light) and blue (dark) bars, respectively.

2 Data and Monte Carlo samples

The data samples used for the muon performance studies reported in this paper were collected with the following types of triggers:

- *The zero-bias trigger*, defined by the coincidence of signals in two dedicated beam position monitors (Beam Position and Timing for LHC eXperiments, BPTX) in the same bunch crossing. Its rate was kept constant at around 20 Hz throughout the year by adjusting the prescale factor to compensate for the rising instantaneous luminosity. Events collected by this trigger do not suffer from any muon-detection bias at trigger level and are used to define an inclusive muon sample for the study of muon kinematic distributions as discussed in section 4.

- *Single-muon triggers.* Muon candidates are reconstructed at the trigger level using information from the muon detectors and the inner tracker. Events containing a muon candidate with online-reconstructed transverse momentum p_{T} greater than a predefined threshold (luminosity-dependent, $15\,\mathrm{GeV}/c$ or lower in the year 2010) are recorded. All muon triggers used in 2010 data taking covered the full muon detector acceptance corresponding to $|\eta| < 2.4$. These triggers were the main source of intermediate-p_{T} and high-p_{T} muons during 2010 data taking, efficiently selecting, e.g., muonic decays of W and Z bosons. Furthermore, to collect cosmic-ray data during breaks in LHC operation, a trigger requiring at least two

2012 JINST 7 P10002

loosely matched segments in the bottom half of the barrel muon system or a single segment in the endcap muon system was implemented. The triggers from the top half were disabled to avoid the need for special synchronization.

- *Muon-plus-track triggers.* To improve the efficiency of collecting J/ψ events, a specialized high-level trigger was implemented. This trigger selected events in which the muon track can be paired with an inner-tracker track of opposite charge yielding an invariant mass close to that of the J/ψ. To sample the efficiencies in the whole p_T region evenly, multiple instances of the trigger were deployed with different thresholds on the transverse momentum of the inner-tracker track. In addition, another set of specific J/ψ triggers was implemented, using only the muon system for the reconstruction of one of the two muons. The muon-plus-track triggers were used to measure identification and trigger efficiencies for low-p_T muons, as described in sections 5 and 9.

- *Jet and missing transverse energy ($\not{E}_T$) triggers.* Using calorimeter information, jets and missing transverse energy are reconstructed online. Triggers with different thresholds on jet transverse energy and $\not{E}_T$ were implemented. These events were used to select a sample of muons that was unbiased by the requirements of the muon trigger.

In addition, a loose *double-muon trigger* requiring two or more muon candidates reconstructed online and not applying any additional selection criteria was implemented, taking advantage of the relatively low luminosity during 2010 data taking. This trigger selected dimuons in the invariant mass region spanning more than three orders of magnitude, from a few hundred MeV/c^2 to a few hundred GeV/c^2, as shown in figure 3. The events collected with this trigger were used in both the detector commissioning and physics studies.

All collision data samples studied in this paper were filtered by requiring at least one well-reconstructed primary vertex to reduce the contamination from non-collision backgrounds. Techniques to further suppress the non-collision backgrounds according to the needs of physics analysis are discussed in section 7.

To compare the results obtained in data to predictions, a number of simulated samples were produced using Monte Carlo (MC) techniques. All MC samples were produced with the CTEQ6L [7] set of parton distribution functions and different event generators were used depending on the process considered. Samples of $t\bar{t}$ and QCD multijet events were generated using PYTHIA 6 [8] with the Z2 tune [9], as well as inclusive muon-enriched samples, in which only events containing at least one muon with transverse momentum greater than a given threshold were selected at generation level. Samples of prompt J/ψ mesons as well as J/ψ particles originating from the decays of b hadrons were generated with PYTHIA interfaced to EVTGEN [10]. Inclusive W and Z samples and non-resonant Drell-Yan events were produced using the POWHEG [11] event generator, interfaced with PYTHIA for the simulation of parton showering and hadronization processes. For W+jets and Z+jets samples with a given number of jets, the MADGRAPH [12] event generator was used, combined with PYTHIA for showering and hadronization.

Generated events were processed through a full GEANT4-based [13, 14] detector simulation, trigger emulation, and event reconstruction chain. A realistic misalignment scenario based on the knowledge of positions of different elements of the inner-tracker and muon systems was used to

2012 JINST 7 P10002

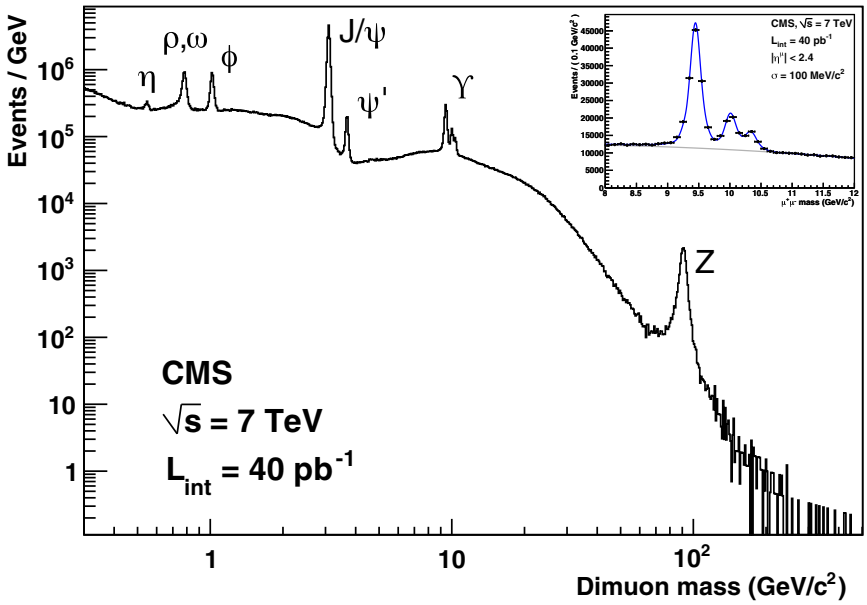

Figure 3. Invariant mass spectrum of dimuons in events collected with the loose double-muon trigger in 2010. The inset is a zoom of the 8–12 GeV/c^2 region, showing the three $\Upsilon(nS)$ peaks clearly resolved owing to a good mass resolution, about 100 MeV/c^2 in the entire pseudorapidity range and 70 MeV/c^2 when both muons are within the range $|\eta| < 1$.

describe the detector geometry. The positions of the tracker modules were evaluated by applying the track-based alignment procedure to a sample of 2.2 million cosmic-ray muons and 3.3 million minimum-bias events collected in 2010. The residual uncertainties in the positions of individual tracker modules were measured to be smaller than 6 μm in the pixel detector and less than 10 μm in the silicon strip tracker. The procedure used to emulate the remaining misalignment effects in the simulation closely followed that employed to align the tracker using data, and used as input the module displacements determined from cosmic-ray data available at the time of the MC sample production. As a result, the simulated geometry of the tracker included coherent displacements and rotations of tracker modules that could bias the track reconstruction without affecting the local alignment precision. These coherent movements were estimated not to exceed 200 μm. The alignment precision for muon chambers was estimated by comparison with photogrammetry to be about 500 μm for DT chambers and between 300 and 600 μm (depending on the ring) for CSCs, in the r-ϕ plane. The misalignment scenario for the muon chambers used in the simulation was consistent with this precision.

Unless stated otherwise, additional proton-proton interactions in the same bunch crossing (pile-up) were not simulated because of their relatively small rate in 2010 (2.7 interactions on average). Such pile-up is expected to have a negligible effect on the results presented here.

2012 JINST 7 P10002

3 Muon reconstruction and identification

In the standard CMS reconstruction for pp collisions [2, 15], tracks are first reconstructed independently in the inner tracker (*tracker track*) and in the muon system (*standalone-muon track*). Based on these objects, two reconstruction approaches are used:

- *Global Muon reconstruction (outside-in).* For each standalone-muon track, a matching tracker track is found by comparing parameters of the two tracks propagated onto a common surface. A *global-muon track* is fitted combining hits from the tracker track and standalone-muon track, using the Kalman-filter technique [16]. At large transverse momenta, $p_{\mathrm{T}} \gtrsim 200\,\mathrm{GeV}/c$, the global-muon fit can improve the momentum resolution compared to the tracker-only fit [2, 15].

- *Tracker Muon reconstruction (inside-out).* In this approach, all tracker tracks with $p_{\mathrm{T}} > 0.5\,\mathrm{GeV}/c$ and total momentum $p > 2.5\,\mathrm{GeV}/c$ are considered as possible muon candidates and are extrapolated to the muon system taking into account the magnetic field, the average expected energy losses, and multiple Coulomb scattering in the detector material. If at least one muon segment (i.e., a short track stub made of DT or CSC hits) matches the extrapolated track, the corresponding tracker track qualifies as a Tracker Muon. Track-to-segment matching is performed in a local (chamber) coordinate system, where local x is the best-measured coordinate (in the r-ϕ plane) and local y is the coordinate orthogonal to it. The extrapolated track and the segment are considered to be matched if the distance between them in local x is less than 3 cm or if the value of the pull for local x is less than 4, where the pull is defined as the difference between the position of the matched segment and the position of the extrapolated track, divided by their combined uncertainties [2].

Tracker Muon reconstruction is more efficient than the Global Muon reconstruction at low momenta, $p \lesssim 5\,\mathrm{GeV}/c$, because it requires only a single muon segment in the muon system, whereas Global Muon reconstruction is designed to have high efficiency for muons penetrating through more than one muon station and typically requires segments in at least two muon stations.

Owing to the high efficiency of the tracker-track reconstruction [17] and the very high efficiency of reconstructing segments in the muon system, about 99% of muons produced in pp collisions within the geometrical acceptance of the muon system and having sufficiently high momentum are reconstructed either as a Global Muon or a Tracker Muon, and very often as both. Candidates found both by the Global Muon and the Tracker Muon approaches that share the same tracker track are merged into a single candidate. Muons reconstructed only as standalone-muon tracks have worse momentum resolution and higher admixture of cosmic-ray muons than the Global and Tracker Muons and are usually not used in physics analyses.

The combination of different algorithms provides robust and efficient muon reconstruction. Physics analyses can set the desired balance between identification efficiency and purity by applying a selection based on various muon identification variables. In this paper we study the performance of three basic muon identification algorithms:

- *Soft Muon selection.* This selection requires the candidate to be a Tracker Muon, with the additional requirement that a muon segment is matched in both x and y coordinates with

2012 JINST 7 P10002

the extrapolated tracker track, such that the pull for local x and y is less than 3. Segments that form a better match with a different tracker track are not considered. These additional requirements are optimized for low p_{T} ($< 10\,\mathrm{GeV}/c$) muons. This selection is used in quarkonia and B-physics analyses in CMS [18].

- *Tight Muon selection.* For this selection, the candidate must be reconstructed outside-in as a Global Muon with the $\chi^2/d.o.f.$ of the global-muon track fit less than 10 and at least one muon chamber hit included in the global-muon track fit. In addition, its corresponding tracker track is required to be matched to muon segments in at least two muon stations (this implies that the muon is also reconstructed inside-out as a Tracker Muon), use more than 10 inner-tracker hits (including at least one pixel hit), and have a transverse impact parameter $|d_{\mathrm{xy}}| < 2$ mm with respect to the primary vertex. With this selection, the rate of muons from decays in flight is significantly reduced (see section 4), at the price of a few percent loss in efficiency for prompt muons such as those from W and Z decays (see section 5). The Tight Muon selection is used in many physics analyses in CMS, in particular in the measurements of inclusive W and Z cross sections [19, 20].

- *Particle-Flow Muon selection.* The CMS particle-flow event reconstruction algorithm [21] combines information from all CMS subdetectors to identify and reconstruct individual particles like electrons, hadrons or muons. For muons, the particle-flow approach applies particular selection criteria to the muon candidates reconstructed with the Global and Tracker Muon algorithms described above. Depending on the environment of the muon (for example, whether it is isolated or not) the selection criteria are adjusted making use of information from other subdetectors (for example, the energy deposition in the calorimeters). In general, the selection is optimized in order to identify muons within jets with high efficiency, while maintaining a low rate for the misidentification of charged hadrons as muons. The details of the particle-flow muon selection are described in ref. [22].

The default algorithm for muon momentum assignment in CMS is called the "sigma switch". This algorithm chooses from the momentum estimates given by the tracker-only fit and by the global fit. The global fit is chosen when both fits yield muon p_{T} above $200\,\mathrm{GeV}/c$ and give the charge-to-momentum ratios q/p that agree to within $2\sigma_{q/p}$ of the tracker-only fit; in all other cases the tracker-only fit is taken.

In addition, CMS has developed specialized algorithms for high-p_{T} muon reconstruction and momentum assignment. As the muon passes through the steel of the magnet return yoke, multiple scattering and radiative processes can alter the muon trajectory. While the former is not so important for high-momentum muons, the latter can result in large energy losses and can also produce electromagnetic showers giving rise to additional hits in the muon chambers. As a consequence, the estimate of the muon momentum at the production vertex can be significantly different from its true value. Therefore, several different strategies for including information from the muon system have been developed and studied using cosmic rays [2]:

- *Tracker-Plus-First-Muon-Station (TPFMS) fit.* This algorithm refits the global-muon track ignoring hits in all muon stations except the innermost one containing hits, for reduced sensitivity to possible showering deeper in the muon system.

2012 JINST 7 P10002

- *The Picky fit.* This algorithm again starts with the hit list of the global-muon track, but, in chambers appearing to have hits from showers (determined by the hit occupancy of the chamber), retains only the hits that, based on a χ^2 comparison, are compatible with the extrapolated trajectory.

To further improve the resolution at high p_{T}, mainly by reducing the tails of the momentum resolution distribution, combinations of the above can be used. In particular, the *Tune P* algorithm chooses, on a muon-by-muon basis, between the tracker-only, TPFMS, and Picky fits. The algorithm starts with the Picky fit, then switches to the tracker-only fit if the goodness of fit of the latter is significantly better. Then it compares the goodness of fit of the chosen track with that of TPFMS; TPFMS is chosen if it is found to be better. For high-p_{T} muons, TPFMS and Picky algorithms are selected by Tune P in most of the cases, in approximately equal amounts, while the tracker-only fit is selected only in a few percent of events. For most analyses of the 2010 LHC data involving high-p_{T} muons, Tune P was used for the determination of the muon momentum.

4 General comparisons between data and simulation

In this section we present data-to-simulation comparisons for two samples of muons: 1) a fully inclusive sample of low-p_{T} muons collected with the zero-bias trigger, and 2) an inclusive sample of intermediate- and high-p_{T} muons collected with the single-muon trigger requiring a minimum transverse momentum of 15 GeV/c.

Events collected with the zero-bias trigger were required to contain at least one reconstructed primary vertex within 24 cm of the geometric centre of the detector along the beamline and within a transverse distance from the beam axis of less than 2 cm. The efficiency of this requirement for simulated pp collisions having at least one reconstructed muon was found to be 99%. About 14 million minimum-bias events were thus selected from a total data sample of events corresponding to 0.47 nb^{-1} of integrated luminosity; the contamination from cosmic-ray muons in the sample was estimated to be negligible. The corresponding MC sample consists of about 36 million minimum-bias events generated using PYTHIA.

The sample of events collected with the single-muon trigger with the p_{T} threshold of 15 GeV/c consists of about 20 million events corresponding to an integrated luminosity of 31 pb^{-1}. Monte Carlo samples used for the comparison correspond to about 10 times larger integrated luminosity and include the simulation of QCD processes, quarkonia production, electroweak processes such as W and Z boson production, non-resonant Drell-Yan processes, and top-pair production. The total cross sections for W and Z production were rescaled to match the next-to-next-to-leading-order (NNLO) calculations; the cross sections for b-hadron and $\mathrm{t\bar{t}}$ production were rescaled to the next-to-leading-order (NLO) calculations (see section 4.2).

In both cases the simulation was normalized according to the integrated luminosity of the data sample. The uncertainty in the absolute value of luminosity was estimated to be 4% [23].

4.1 Classification of muon sources in simulation

In the range of $p_{\mathrm{T}} \lesssim 30$ GeV/c, the most abundant source of muons is semileptonic decays of heavy-flavour hadrons. This contribution is accompanied by a high rate of muon candidates arising from

2012 JINST 7 P10002

light-flavour hadron decays and hadron showers not fully contained in the calorimeters. The relative weights of these background contributions are quite sensitive to the details of the muon selection. Muons from decays of W and Z bosons dominate the p_{T} spectrum in the region $p_{\mathrm{T}} \gtrsim 30\,\mathrm{GeV}/c$.

In the simulation, for each reconstructed muon, the hits in the muon system can be associated unambiguously with the simulated particle that produced them. This allows the classification of reconstructed muons into the following categories:

- *Prompt muons.* Here the majority of muon chamber hits associated with the reconstructed muon candidate were produced by a muon, arising either from decays of W, Z, and promptly produced quarkonia states, or other sources such as Drell-Yan processes or top quark production. These individual sources are shown separately where appropriate.

- *Muons from heavy flavour.* Here the majority of muon chamber hits of the muon candidate were again produced by a muon, but the muon's parent particle was a beauty or charmed hadron, or a τ lepton. This class of events has been split according to the heaviest flavour generated in the event. Hence, *beauty* includes muons from direct b-hadron decays, from cascade b $\rightarrow$ c hadron decays, as well as cascade decays of τ leptons from b hadrons.

- *Muons from light flavour.* In this category, the majority of muon chamber hits of the muon candidate were produced by a muon arising from a decay in flight of light hadrons (π and K) or, less frequently, from the decay of particles produced in nuclear interactions in the detector material. This category includes hadrons whose tracks reconstructed in the tracker were mistakenly matched to the muon chamber hits.

- *Hadron punch-through.* Here the majority of muon chamber hits of the misidentified muon candidate were produced by a particle that was not a muon. "Punch-through" (i.e., hadron shower remnants penetrating through the calorimeters and reaching the muon system) is the most common source of these candidates, although "sail-through" (i.e., particles not undergoing nuclear interactions upstream of the muon system) is present as well.

- *Duplicate.* If one simulated particle gives rise to more than one reconstructed muon candidate, that with the largest number of matched hits is assigned to one of the above categories, and any others are labeled as "duplicate". Duplicate candidates can arise either from failures of the pattern recognition of the reconstruction software, or from patterns that mimic multiple candidates.

4.2 Kinematic distributions of muons

From the 2010 data sample of zero-bias events with a well-established primary vertex, we obtain 318 713 muon candidates passing the Soft Muon selection and 24 334 passing the Tight Muon selection. The overall ratio of the number of muon candidates in data to the prediction of the PYTHIA MC generator normalized to the same integrated luminosity is 1.05 for Soft Muons and 1.01 for Tight Muons.

The distributions of the muon transverse momentum p_{T} multiplied by its charge q, pseudorapidity η, and azimuthal angle ϕ for Soft and Tight Muons in zero-bias events are shown in figure 4. The pseudorapidity distribution is peaked in the forward region because there the minimum p_{T}

2012 JINST 7 P10002

Table 1. Composition by source of the low-p_T muon candidates reconstructed in zero-bias events, according to simulation for the Soft and Tight Muon selections.

Muon source	Soft Muons [%]	Tight Muons [%]
beauty	4.4	22.2
charm	8.3	21.9
light flavour	79.0	55.7
hadron punch-through	5.4	0.2
duplicate	2.9	<0.01
prompt	$\lesssim 0.1$	$\lesssim 0.1$

required to reach the muon stations is lower than in the barrel: in the endcaps the threshold in p_T is about 0.5 GeV/c, while in the barrel it is about 3–4 GeV/c. Overall, there is good agreement between data and simulation both in the number of events and in the shapes of the distributions. Some discrepancies result from imperfect simulation of local detector conditions, affecting for example the muon identification efficiency at low p_T, as shown in section 5. Furthermore, the leading-order QCD predictions by PYTHIA have large uncertainties.

Table 1 lists the sources of muons according to simulation. The majority of reconstructed muon candidates originate from decays in flight of pions and kaons ("light flavour"). This is particularly evident for Soft Muons, while Tight Muons have larger heavy-flavour components. For both selections the contribution of muons from heavy-flavour decays increases with p_T. The Tight Muon selection reduces the hadron punch-through contribution to 0.2% while it is about 5% in Soft Muons. The measurements of muon misidentification probabilities presented in section 5.3 confirm that the simulation correctly estimates the probability for light hadrons to be misidentified as muons.

Among all single-muon triggers used in 2010, the trigger with a p_T threshold of 15 GeV/c was the lowest-threshold unprescaled trigger during a period when most of the data, corresponding to an integrated luminosity of about 31 pb^{-1}, were collected. The kinematic distributions of muons collected with this trigger have been compared to the Monte Carlo expectations after applying a selection on the reconstructed muon p_T of 20 GeV/c, for which the trigger efficiency has reached the plateau. The Tight Muon selection applied in this kinematic range has a high efficiency for prompt muons, removing most of the background from light-hadron decays and hadron punch-through. After the Tight Muon selection, 824 007 muon candidates remain.

For comparison with these events, the beauty production cross section given by PYTHIA has been rescaled to the NLO QCD predictions [24, 25], which were shown to describe recent CMS measurements well [26, 27]. Without this rescaling, an excess in the predicted beauty component is observed in the inclusive p_T distribution for muon p_T lower than about 40 GeV/c, and also in the muon impact-parameter distribution for transverse distances characteristic of b-hadron decays. No corrections accounting for differences between the measured and expected muon trigger and identification efficiencies have been applied. Such corrections could lead to effects of up to 5%, depen-

2012 JINST 7 P10002

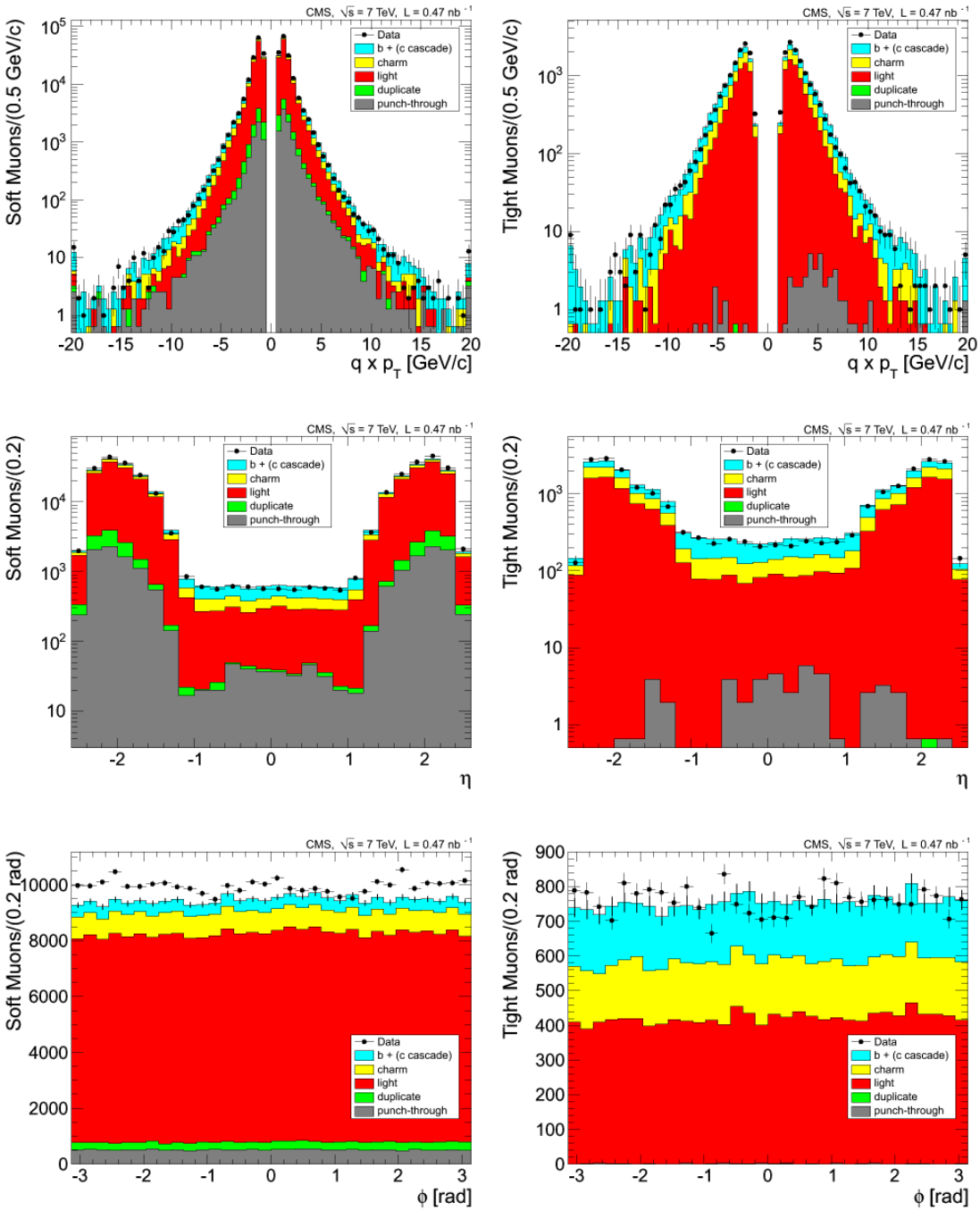

Figure 4. Distributions of kinematic variables for a sample of muons selected by the zero-bias trigger, for data (points) and for simulation subdivided into the different categories of contributing muons (histograms). The kinematic variables are the muon transverse momentum multiplied by the charge (top), pseudorapidity (middle), and azimuthal angle (bottom). For each variable, the left plot shows the distribution for Soft Muons, and the right plot that for Tight Muons. The first (last) bin in the $q \times p_{\mathrm{T}}$ distributions includes the underflow (the overflow). The error bars indicate the statistical uncertainty, for both data and MC samples.

2012 JINST 7 P10002

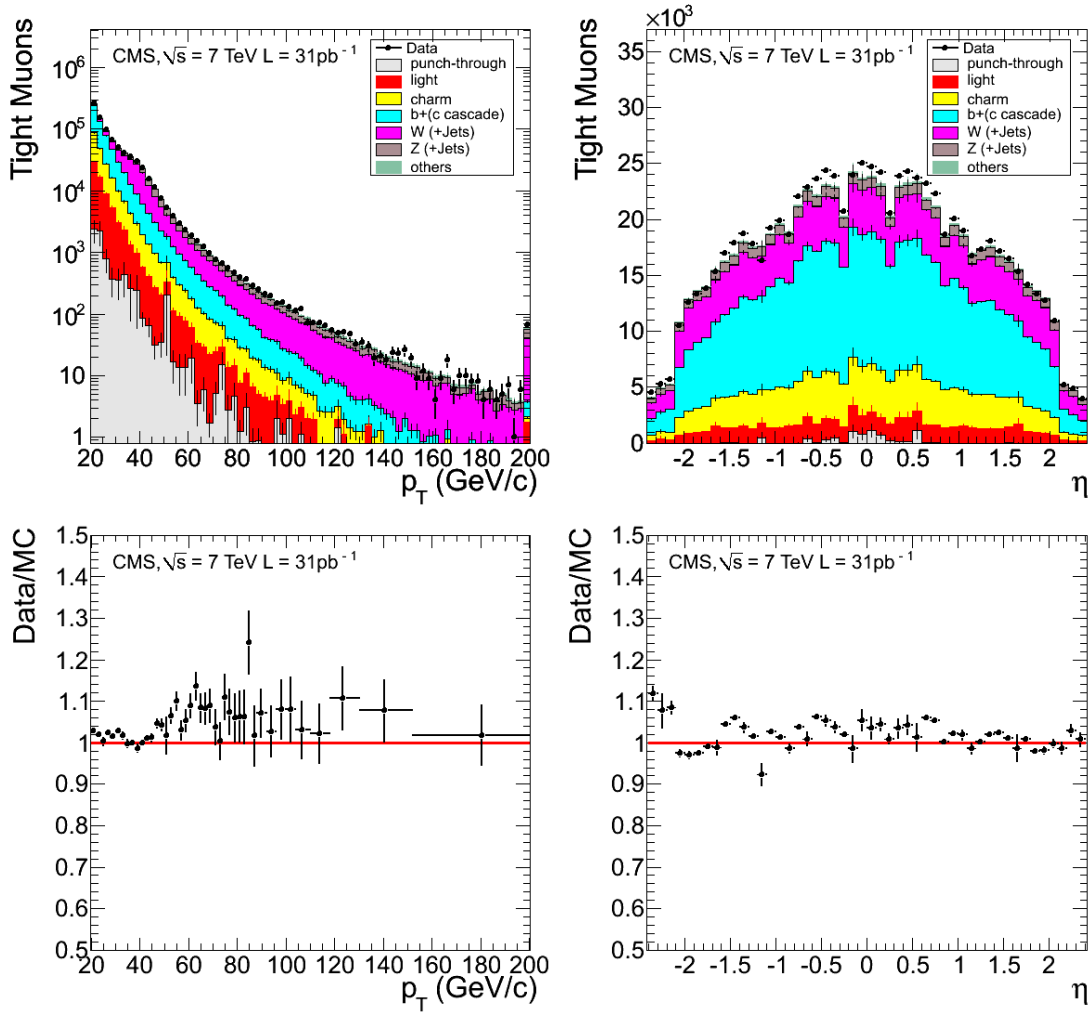

Figure 5. Distributions of transverse momentum (top left) and pseudorapidity (top right) for Tight Muons with $p_{\mathrm{T}} > 20\,\mathrm{GeV}/c$, comparing data (points with error bars) to Monte Carlo simulation broken down into its different components. The last bin in the p_{T} distribution includes the overflow. Dips in the η distribution are due to inefficiencies related to the muon detector geometry. The corresponding ratios of data and MC distributions are shown in the bottom row. The error bars include statistical uncertainties only.

dent on pseudorapidity, as discussed in sections 5 and 9. The overall ratio of the muon yield in data to the Monte Carlo predictions normalized to the same integrated luminosity is found to be 1.02.

The muon transverse momentum and pseudorapidity distributions for $p_{\mathrm{T}} > 20\,\mathrm{GeV}/c$ are compared to the expectations from the Monte Carlo simulation in figure 5. The estimated composition of the sample obtained from the simulation-based studies is shown in table 2. Muons from light-hadron decays are predicted to contribute less than 10%, while the hadron punch-through is suppressed to about 1%. The beauty contribution dominates up to muon transverse momentum of about $30\,\mathrm{GeV}/c$, where the W contribution starts to prevail, leading to a shoulder in the falling p_{T} spectrum. The inclusive muon yield agrees with the expectations within a few percent up to a transverse momentum of $50\,\mathrm{GeV}/c$. At higher momenta the leading processes are W and

2012 JINST 7 P10002

Table 2. Composition by source of Tight Muons with $p_T > 20\,\text{GeV}/c$ according to simulation.

Muon source	Tight Muons with $p_T > 20\,\text{GeV}/c$ [%]
W (+ jets)	20.8
Z/Drell-Yan (+ jets)	4.7
top	0.1
quarkonia	0.7
beauty	47.6
charm	17.4
light flavour	7.8
hadron punch-through	0.9
duplicate	<0.01

Z production, occasionally associated with hard jets. In this p_T region, the data agree with the predictions within 10%. This has been verified to be fully consistent with theoretical uncertainties related to missing higher-order QCD contributions, by comparing the MADGRAPH generator used to simulate W and Z with other Monte Carlo programs for the W(Z)+jets processes. In conclusion, given the known experimental and theoretical uncertainties, the agreement between the data and simulation is satisfactory over the entire momentum range of $p_T \lesssim 200\,\text{GeV}/c$.

4.3 Muon identification variables

The basic selections discussed in section 3 can be further refined for specific purposes using additional information available for each reconstructed muon.

The Tracker Muon segment matching is a powerful tool to reject hadron punch-through. The number of muon stations with matched segments (see section 3) is shown in figure 6(a) for Soft Muons in zero-bias events. The contamination from hadron punch-through is evident in the expectation for one matched station. The probability for a punch-through to be identified as a Soft Muon is drastically reduced by requiring matched segments in at least two stations. The contribution from low-momentum muons from light-quark decays is also suppressed by this requirement. Figure 6(b) shows the distribution of the transverse impact parameter, where the long tail is dominated by pion and kaon decays in flight. Requirements on both variables are used in the Tight Muon selection designed to select prompt muons such as those from W and Z decays (see section 3).

A few other examples of identification variables are shown in figure 7 for Tight Muons with $p_T > 20\,\text{GeV}/c$ collected with the single-muon trigger. The transverse impact parameter and its significance in figures 7(a) and (b) are useful to select either prompt muons or, by inverting the requirement, muons from heavy-flavour decays. The $\chi^2/d.o.f.$ of the tracker-track fit is also a good discriminant to suppress muons from decays in flight, as can be seen from the composition of the tail of the distribution in figure 7(c). The muon isolation is a simple quantity to select prompt muons with high purity. The scalar sum of the transverse momenta of tracks in the inner tracker and

2012 JINST 7 P10002

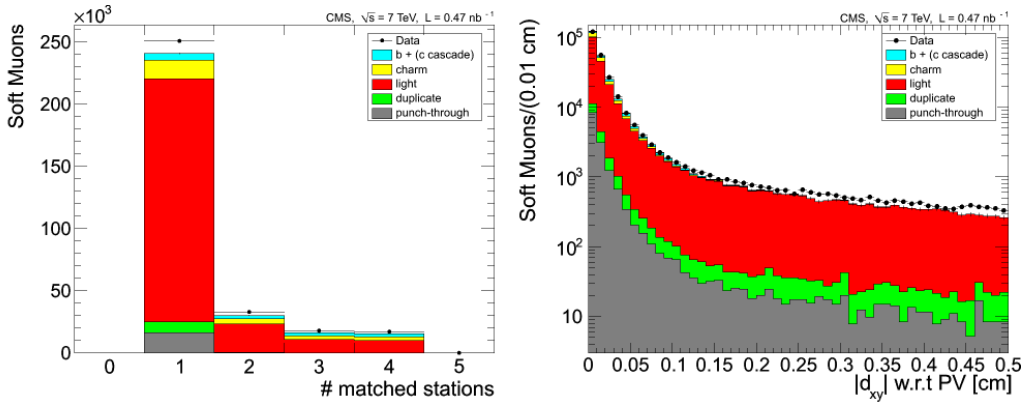

(a) **(b)**

Figure 6. Comparison of data and simulation for distributions of Soft Muons in zero-bias events: (a) number of muon stations with matched segments; (b) transverse impact parameter d_{xy} of the muon with respect to the primary vertex (PV). The MC distributions are normalized to the integrated luminosity of the data sample. The error bars indicate the statistical uncertainty.

the transverse energies in calorimeter cells (both in the ECAL and HCAL) within a cone of radius $\Delta R = \sqrt{(\Delta\varphi)^2 + (\Delta\eta)^2} = 0.3$ centred on the direction vector of the muon candidate is calculated, excluding the contribution from the candidate itself. The relative combined isolation $I^{\mathrm{rel}}_{\mathrm{comb}}$ (further discussed in section 8) is defined as the ratio of this scalar sum to the transverse momentum of the muon candidate. Figure 7(d) shows the distribution of the $I^{\mathrm{rel}}_{\mathrm{comb}}$ variable in events with a single reconstructed primary vertex, compared to the simulation with no pile-up effects. Isolated muons promptly produced in decays of W and Z bosons dominate the region $I^{\mathrm{rel}}_{\mathrm{comb}} < 0.1$. Overall, the agreement between data and Monte Carlo predictions for the muon identification variables is good both for zero-bias events and for events recorded with the single-muon trigger.

The accuracy of the propagation of the tracker tracks to the muon system and the performance of the track-to-segment match have been further studied using Tracker Muons with $p_{\mathrm{T}} > 20\,\mathrm{GeV}/c$, with tight selection requirements on the tracker variables only, to avoid possible biases. To further purify the muon sample, an isolation requirement $I^{\mathrm{rel}}_{\mathrm{comb}} < 0.1$ has been applied.

The distribution of distance in local x between the position of the extrapolated tracker track and the position of the muon segment has been compared between data and simulation, for successful track-to-segment matches (distance less than 3 cm or pull less than 4, see section 3). The RMS width of residuals is shown in figure 8 as a function of the muon-station number, for the DT and CSC systems. As expected, the width of the distributions increases with the amount of material upstream of the muon station and with the distance over which the track is extrapolated, from the innermost to the outermost muon stations (from MB1 to MB4 and from ME1 to ME4 in the DT and the CSC systems, respectively). The general trend is well reproduced by the Monte Carlo simulation, although the increase of the width is a bit larger in the simulation. As the outer ring of ME4 is only partially instrumented with chambers (see figure 1), the residual for ME4 is not directly comparable with the measurements in the other stations because muons traversing the installed ME4 chambers have a higher average momentum.

2012 JINST 7 P10002

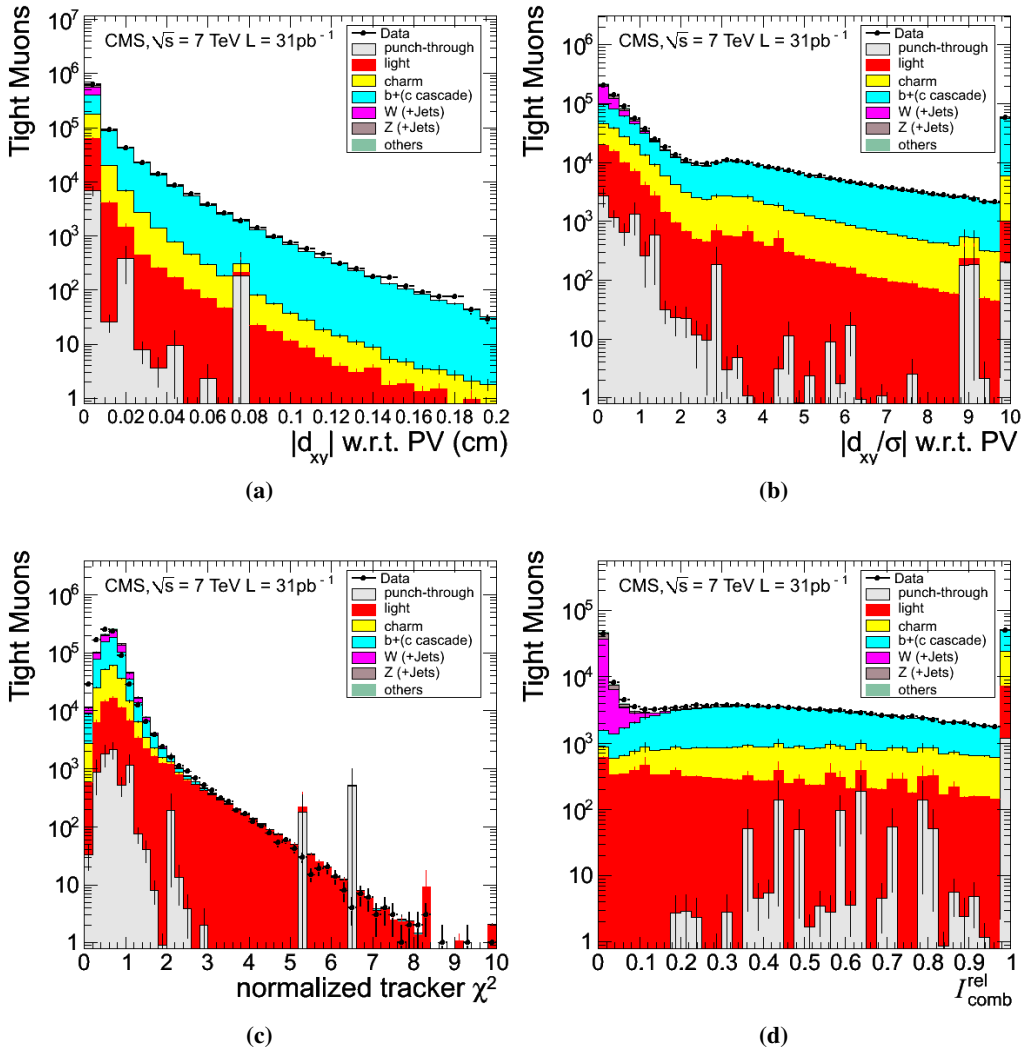

Figure 7. Identification variables for Tight Muons with $p_T > 20\,\mathrm{GeV}/c$: (a) transverse impact parameter d_{xy} with respect to the primary vertex (PV); (b) significance of the transverse impact parameter; (c) $\chi^2/d.o.f.$ of the fit of the track in the inner tracker; (d) relative combined isolation (tracker+calorimeters), with a cone size $\Delta R = 0.3$, for events with a single reconstructed PV. The MC distributions are normalized to the integrated luminosity of the data sample in (a), (b), and (c), and to the number of events in the data sample in (d). The last bin in (b) and in (d) includes the overflow. Error bars indicate statistical uncertainties.

The residuals for track-to-segment matches have also been studied as a function of the muon momentum and pseudorapidity. The first muon station is the most important in the global track reconstruction: it is where the track's sagitta, determined by the magnetic field inside the solenoid, is largest, and its measurements are the least affected by multiple-scattering and showering effects because the material upstream of the first station corresponds only to the inner detectors, the calorimeters, and the magnet cryostat, whereas the stations downstream are also preceded by the steel sections of the magnet return yoke. The average material thickness traversed

2012 JINST 7 P10002

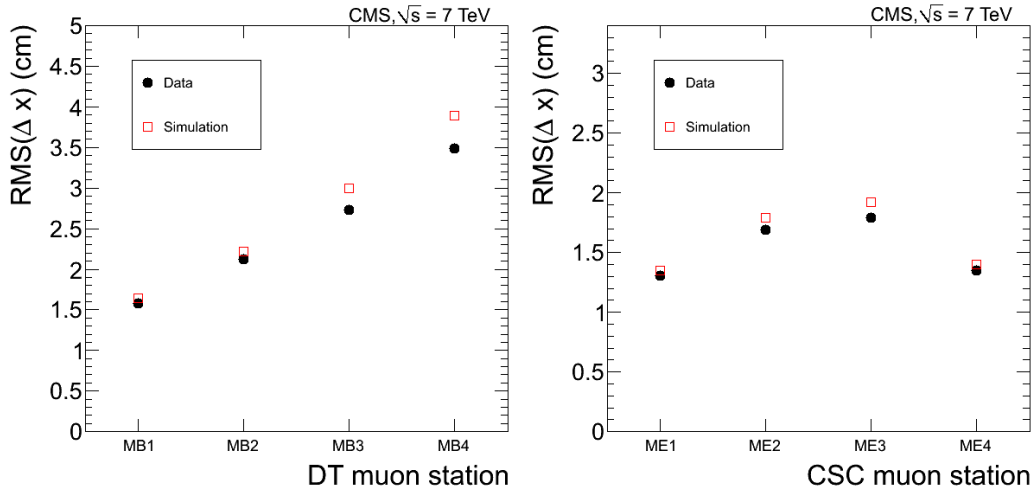

Figure 8. RMS width of residuals of the local x position, given by the position of the muon segment with respect to the extrapolated tracker track, as a function of the muon station, for DT chambers in the barrel region (left) and CSCs in the endcap regions (right). Data are compared with MC expectations.

by a muon reaching the first station is quite different depending on the angular region [15]. In addition, the width of the position residual increases linearly with the propagation distance of the muon trajectory from the interaction region to the first muon chamber. Figure 9(a) shows the RMS width of the residual of the local x position as a function of muon pseudorapidity. A selection on the minimum momentum $p > 90\,\mathrm{GeV}/c$ has been applied to remove the bias induced by the trigger threshold ($p_{\mathrm{T}} > 15\,\mathrm{GeV}/c$) in the endcap regions. As expected from the η dependence of the distance between the inner tracker and the first muon station and of the material thickness, the residual width reaches the maximum values in the overlap region, $0.9 < |\eta| < 1.2$. Figures 9(b), 9(c), and 9(d) show the momentum dependence of the RMS width, separately for the barrel, overlap, and endcap regions. The width decreases with increasing momentum because of smaller multiple-scattering effects. The shapes of the distributions are well reproduced by the Monte Carlo simulation, although the simulation predicts a somewhat larger width. The only exception is the highest momentum bin in the endcap region (figure 9(d)), where the distribution of position resolution in data has larger non-Gaussian tails than predicted by simulation. This also leads to the discrepancy observed at the extreme η bins in figure 9(a).

We have also examined the distributions of pulls of the local positions and directions in both DT and CSC systems. The widths of the pulls were found to be close to unity and no large biases were observed, thus demonstrating that the propagation works as expected and that the uncertainties are well estimated. The widths of the pull distributions in the simulation are about 10% larger than in data. As demonstrated in the next section, such agreement between the expected and the measured residuals and pulls is sufficient to obtain a good description of the muon reconstruction and identification efficiencies by the simulation.

High-momentum muons can give rise to electromagnetic showers in the muon system. These may produce extended clusters of hits in the muon chambers, which can degrade the quality of muon track reconstruction. Hence an accurate simulation and reliable identification of such showers are needed.

2012 JINST 7 P10002

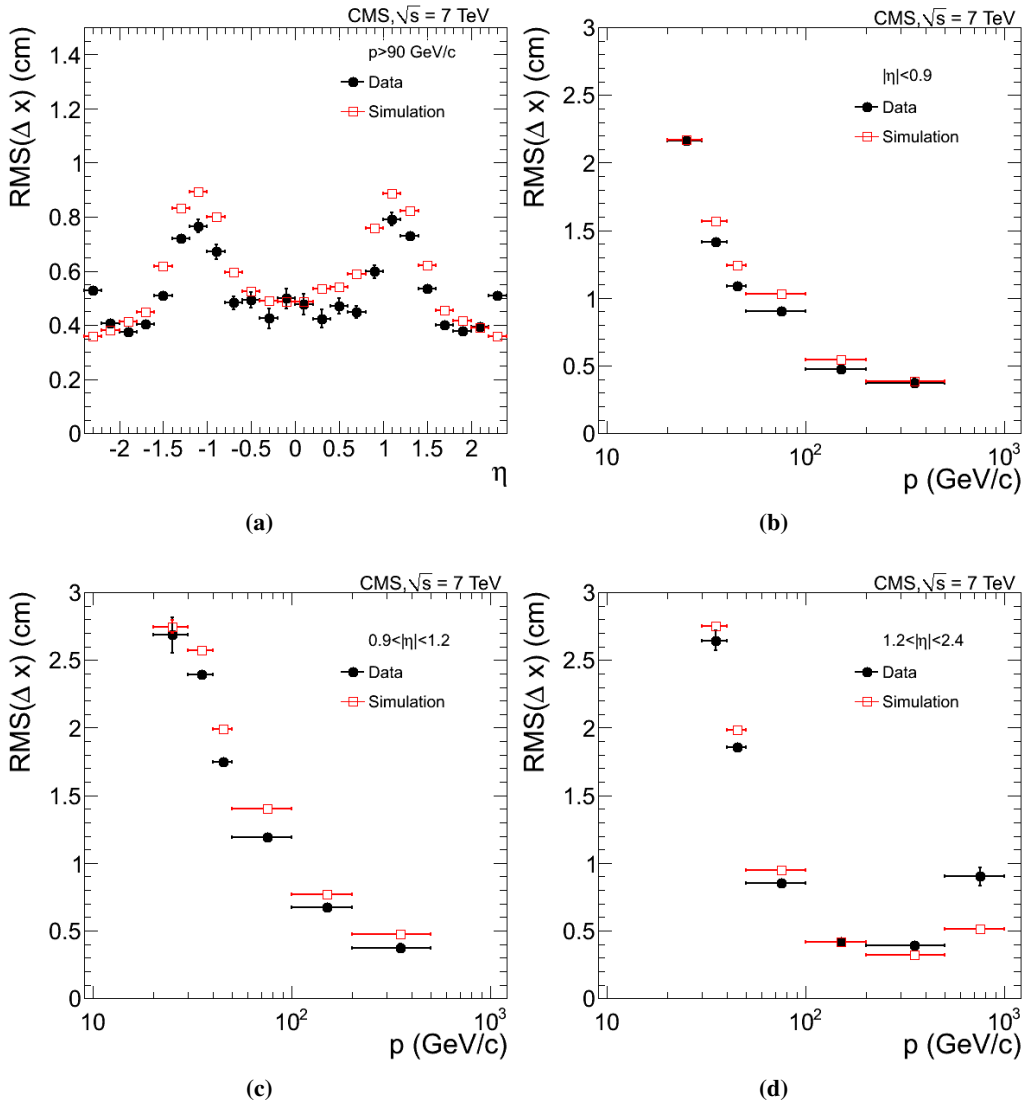

Figure 9. RMS width of residuals of the local x position for the track-to-segment match in the first muon station (a) as a function of the muon pseudorapidity, with a requirement on momentum $p > 90\,\mathrm{GeV}/c$, and (b)–(d) as a function of the muon momentum in different angular regions: (b) $|\eta| < 0.9$; (c) $0.9 < |\eta| < 1.2$; (d) $1.2 < |\eta| < 2.4$. Data are compared with MC expectations.

We have considered several variables that might indicate the presence of electromagnetic showers in the muon system, and examined how well they are reproduced by the simulation. Figure 10 shows the distributions of two of them: the number of hits reconstructed in the DT chamber crossed by a track but not used in the track fit, and the transverse size of the cluster of hits around a track. The cluster of hits is defined iteratively, starting from the impact point of the extrapolated muon track and successively adding any hit if it lies within $\Delta\phi < 0.05$ rad of the hit in the existing cluster with largest radial distance from the impact point. The transverse size of a cluster is defined as the maximum distance in the local x-y plane between the impact point of the track and any hit in the cluster. The plots are made for two samples of high-energy muons (with p recon-

2012 JINST 7 P10002

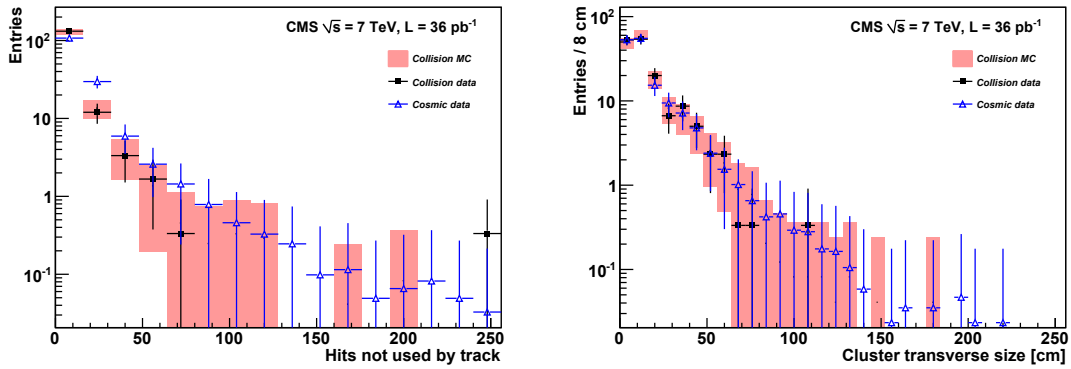

Figure 10. Comparison of data and simulation for variables characterizing electromagnetic showers, for muons with $p > 150\,\mathrm{GeV}/c$ in the barrel region: the number of reconstructed muon hits not used in a track fit (left); the transverse size of the cluster of hits around a track (right). All distributions are normalized to the number of muons per muon station in the collision data sample.

structed by the tracker-only fit above $150\,\mathrm{GeV}/c$): 1) collision muons, and 2) cosmic-ray muons selected from collision data samples, with a topology similar to that of collision muons. Collision muons were selected by requiring that an event has at least one primary vertex reconstructed close to the nominal beam-spot position, and that the muon passes the Tight Muon selection with additional isolation and track-quality selections to reduce contamination from hadron punch-through. Cosmic-ray muons were selected by requiring events with at most two tracks reconstructed in the inner tracker, one of which was also reconstructed as a Global Muon. The momentum spectra of selected collision-muon and cosmic-muon data samples are quite similar, but the cosmic-muon sample provides a larger number of high-energy muons. Monte Carlo samples of Drell-Yan dimuon events passing event selection criteria identical to those applied to the collision muons were used for comparisons with the data. The vast majority of selected cosmic-ray muons are contained in the barrel region, so figure 10 shows distributions for the DT chambers only. We observe good general agreement between the data and MC simulation.

5 Muon reconstruction and identification efficiency

The previous section focused on the comparison between data and simulation for various distributions of inclusive samples of reconstructed muon candidates. In this section we study exclusive samples of prompt muons, pions, kaons, and protons in data to determine the probability that such a particle is reconstructed and identified as a muon.

Throughout this paper, efficiencies are defined in a relative manner, such that the total efficiency for the entire muon triggering, reconstruction, and identification chain can be calculated as the product of the following individual factors:

$$\varepsilon_\mu = \varepsilon_{\mathrm{track}} \cdot \varepsilon_{\mathrm{rec+id}} \cdot \varepsilon_{\mathrm{iso}} \cdot \varepsilon_{\mathrm{trig}} \,. \tag{5.1}$$

The efficiency to reconstruct a muon in the inner tracker $\varepsilon_{\mathrm{track}}$ was measured separately [17, 19] and found to be 99% or higher within the whole tracker acceptance, in good agreement with

2012 JINST 7 P10002

the expectation from simulations. Given the existence of a tracker track, the combined muon reconstruction and identification efficiencies of the different selection algorithms $\varepsilon_{\text{rec+id}}$ can be measured using "tag-and-probe" techniques. In this section the tag-and-probe method is described, and measurements of the $\varepsilon_{\text{rec+id}}$ efficiencies are presented. In section 8, isolation efficiencies ε_{iso} are calculated from a sample of identified muons. In section 9, trigger efficiencies $\varepsilon_{\text{trig}}$ are defined relative to muons identified offline and, unless otherwise mentioned, passing isolation criteria.

5.1 Muon efficiency using the tag-and-probe method on dimuon resonances

5.1.1 Method

We evaluate the efficiencies for prompt muons by applying a tag-and-probe technique to muons from J/ψ and Z decays. Using this technique it is possible to obtain almost unbiased estimates of the efficiencies of the different stages of muon trigger and offline reconstruction. Events are selected with strict selection requirements on one muon (the "tag" muon) and with a more relaxed selection on the other muon (the "probe" muon), such that the selection applied to the probe muon does not bias the efficiency that one wants to measure. The fraction of probe muons that passes the selection under study gives an estimate of its efficiency.

In this section, muon efficiencies $\varepsilon_{\text{rec+id}}$ are measured with this technique. The probes are tracks reconstructed using only the inner tracker, so there is no bias from the muon subdetectors.

In the case of the J/ψ events, combinatorial backgrounds from other tracks in the event are generally high, particularly at low p_{T}. An effective way to suppress this background is to require that the candidate probe muon has the signature of a minimum-ionizing particle (MIP) in the calorimeters. In this way the background can be reduced by about a factor of three without using any information from the muon system. The residual background in both J/ψ and Z events is subtracted by performing a simultaneous fit to the invariant mass spectra for passing and failing probes with identical signal shape and appropriate background shapes; the efficiency is then computed from the normalizations of the signal shapes in the two spectra.

The uncertainty on the fitted efficiency is determined from the likelihood function. As normalizations of signal and background, efficiency of the background, and parameters controlling the shapes of the signal and background are all parameters of the fit, the uncertainty includes the contributions from the background subtraction procedure. When the background is not negligible, as in the case of J/ψ, the uncertainty on the efficiency obtained by the fit is dominated by these contributions.

For the Z resonance, an unbiased sample of dimuon pairs can be collected efficiently using high-p_{T} single-muon triggers. For J/ψ, specialized high-level triggers were implemented, as described in section 2. The muon-plus-track trigger used for the J/ψ case does not bias the efficiencies related to the muon system, but introduces a small positive bias in the efficiency for the Tight Muon selection, which includes quality requirements on the muon tracker track. To measure this bias, the efficiencies for these quality requirements alone are extracted using another special dimuon trigger that uses only the muon system for the reconstruction of one of the two muons. The bias in efficiency, measured to be $(0.7 \pm 0.1)\%$ in the barrel and $(0.3 \pm 0.2)\%$ in the endcaps, is well reproduced by the simulation and cancels out in the ratio of efficiencies from data and from simulation.

2012 JINST 7 P10002

Under certain kinematic configurations muons from J/ψ decays can be close to each other in the muon system. This can result in inefficiencies for some muon identification algorithms. To obtain an unbiased measurement of single-muon efficiencies, a separation criterion is applied to the tag-probe pairs: the extrapolated impact points of the two muon tracks on the surface of the first muon station must have an angular separation $\Delta R = \sqrt{(\Delta\eta)^2 + (\Delta\phi)^2} > 0.5$. The impact of this requirement on $Z \to \mu^+\mu^-$ events is small: as the large opening angle at the production is preserved by the smaller bending in the magnetic field ($\approx$0.1 rad for a p_T of 25 GeV/c), only 0.2% of the $Z \to \mu^+\mu^-$ events fail the separation criterion above. A dedicated measurement of the dimuon efficiencies as a function of the separation between muons is described in section 5.2.

5.1.2 Results

Figure 11 shows the muon efficiency $\varepsilon_{\text{rec+id}}$ given that a tracker track exists, measured using $J/\psi \to \mu^+\mu^-$ and $Z \to \mu^+\mu^-$ events. The results obtained from the data collected in the 2010 LHC data-taking period are compared with those from simulated events.

For comparisons with $Z \to \mu^+\mu^-$ events, an unweighted sample of simulated events corresponding to an integrated luminosity of $\approx$330pb^{-1} is used: the simulated samples are $Z \to \mu^+\mu^-$, W+jets, and muon-enriched QCD (see section 2). For studies at the J/ψ peak, separate samples of prompt $J/\psi \to \mu^+\mu^-$ and $B \to J/\psi + X \to \mu^+\mu^- + X$ are used, simulated as described in section 2. All MC samples used for the results in this section included simulation of pile-up. Simulation of the background processes is not included for the J/ψ case, as it would be impractical to simulate a sufficient number of inclusive muon-plus-track events. For studies of systematic uncertainties described below, samples of background events have been generated according to the background invariant mass spectra determined from fits to the $J/\psi \to \mu^+\mu^-$ events in the data, and added to the simulated signal events.

The tag-and-probe results in data and in simulation agree within the statistical uncertainties of the measurement almost everywhere. The only significant discrepancy is in the barrel around the turn-on of the efficiency curves, where the efficiency in data is systematically higher than in the simulation. This discrepancy arises from a small difference in the widths of the track-to-segment pulls in data and in simulation discussed in section 4.3: the efficiency of the track-to-segment matching is slightly higher in data, and in the region of rapidly rising efficiency the effect is amplified by the large variation of the efficiency in the bin. The 1–2% data-simulation difference in efficiency for Tight Muons in the endcaps is explained by the fact that several CSCs not operational during most of the 2010 data taking were simulated as fully efficient; this has a negligible effect on efficiencies of the other muon selections because they require a match with only a single muon segment. Using a small sample of simulated events, we have verified that when these chambers are properly accounted for in the simulation, the efficiencies for Tight Muons in data and in simulation agree to better than 1%.

The efficiency for the Tight Selection measured on muons from $Z \to \mu^+\mu^-$ is slightly lower than that measured on muons from $J/\psi \to \mu^+\mu^-$. This difference is partly due to the bias introduced by the muon-plus-track trigger on the track quality criteria described previously and partly due to the different kinematics of the probes. The effect is well reproduced by the simulation.

For Soft Muons and Particle-Flow Muons the plateau of the efficiency is reached at p_T $\approx$4 GeV/c in the endcaps and $\approx$6 GeV/c in the barrel, while for Tight Muons it is reached at

2012 JINST 7 P10002

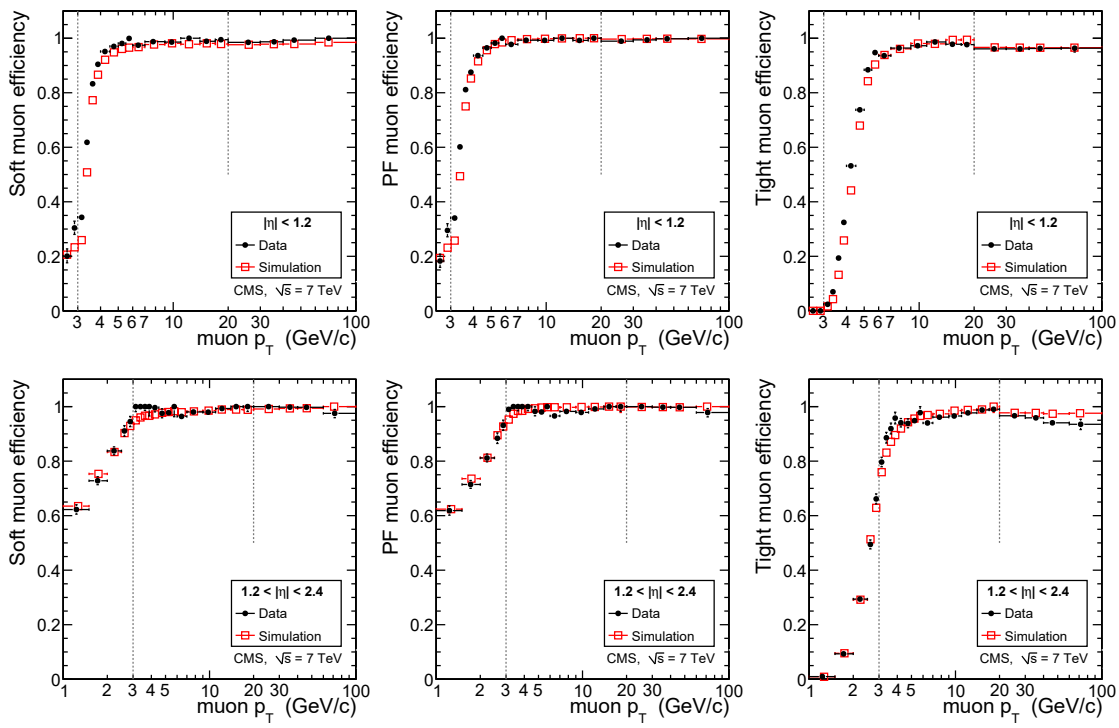

Figure 11. Tag-and-probe results for the muon efficiency $\varepsilon_{\mathrm{rec+id}}$ in data compared to simulation. Given that a tracker track exists, the plots show the efficiency as a function of muon p_{T} for Soft Muons (left), Particle-Flow Muons (middle), and Tight Muons (right) in the barrel and overlap regions (top), and in the endcaps (bottom). The measurement is made using $\mathrm{J}/\psi \to \mu^+\mu^-$ events for $p_{\mathrm{T}} < 20\,\mathrm{GeV}/c$ and $\mathrm{Z} \to \mu^+\mu^-$ events for $p_{\mathrm{T}} > 20\,\mathrm{GeV}/c$. For $p_{\mathrm{T}} < 3\,\mathrm{GeV}/c$, to reduce the background, only tracks with MIP signature are considered.

$\approx$10 GeV/c in both regions. The values of efficiencies at the plateau region obtained using $\mathrm{J}/\psi \to \mu^+\mu^-$ and $\mathrm{Z} \to \mu^+\mu^-$ events in data and simulation are given in table 3. The efficiencies are high, and data and simulation are generally in good agreement. The plateau efficiency for Soft Muons is 1–2% higher in data than in simulation, again due to a difference in the widths of the track-to-segment pulls. The Particle-Flow and Tight Muon selections are much less affected by this difference because they use looser matching criteria between tracks and muon segments. The efficiency at the plateau for the Particle-Flow Muon selection is very close to 100% because the algorithm applies relaxed selection criteria to the high-p_{T} muon candidates if they are isolated.

The dependency of the plateau efficiency on the pseudorapidity is measured using $\mathrm{Z} \to \mu^+\mu^-$ events and is shown in figure 12. The data and simulation agree to better than 2%.

To estimate the effect of pile-up on muon identification performance, the efficiency at the plateau is measured for both $\mathrm{J}/\psi \to \mu^+\mu^-$ and $\mathrm{Z} \to \mu^+\mu^-$ events as a function of the number of reconstructed primary vertices. No loss of efficiency is observed for events containing up to six reconstructed primary vertices, the maximum multiplicity for which a measurement could be made with a statistical uncertainty below 10%.

Trigger efficiencies obtained by a similar tag-and-probe technique are described in section 9.

2012 JINST 7 P10002

Table 3. Muon efficiencies at the efficiency plateau for the different muon selections: efficiency measured from data, and ratio between the measurements in data and simulation. The first uncertainty quoted on the scale factor is the uncertainty on the efficiencies in data and simulation from the fitting procedure, which includes the statistical uncertainty; the second is from the additional systematic uncertainties described later in this section.

Muon selection		$J/\psi \to \mu^+\mu^-$		$Z \to \mu^+\mu^-$	
	Region	Eff. [%]	Data/Sim. ratio	Eff. [%]	Data/Sim. ratio
Soft	$0.0<\|\eta\|<1.2$	$98.4^{+0.3}_{-0.3}$	$1.010\pm0.003\pm0.010$	$99.2^{+0.1}_{-0.1}$	$1.014\pm0.001\pm0.002$
	$1.2<\|\eta\|<2.4$	$98.0^{+0.7}_{-0.7}$	$1.002\pm0.007\pm0.014$	$99.9^{+0.1}_{-0.2}$	$1.005\pm0.002\pm0.004$
Particle-Flow	$0.0<\|\eta\|<1.2$	$98.8^{+0.3}_{-0.3}$	$0.993\pm0.003\pm0.010$	$99.7^{+0.1}_{-0.1}$	$0.999\pm0.001\pm0.002$
	$1.2<\|\eta\|<2.4$	$98.4^{+0.7}_{-0.7}$	$0.988\pm0.007\pm0.014$	$99.8^{+0.1}_{-0.2}$	$0.999\pm0.002\pm0.004$
Tight	$0.0<\|\eta\|<1.2$	$98.4^{+0.3}_{-0.3}$	$0.998\pm0.004\pm0.010$	$96.4^{+0.2}_{-0.2}$	$0.999\pm0.002\pm0.002$
	$1.2<\|\eta\|<2.4$	$96.8^{+0.7}_{-0.7}$	$0.979\pm0.007\pm0.014$	$96.0^{+0.3}_{-0.3}$	$0.983\pm0.003\pm0.004$

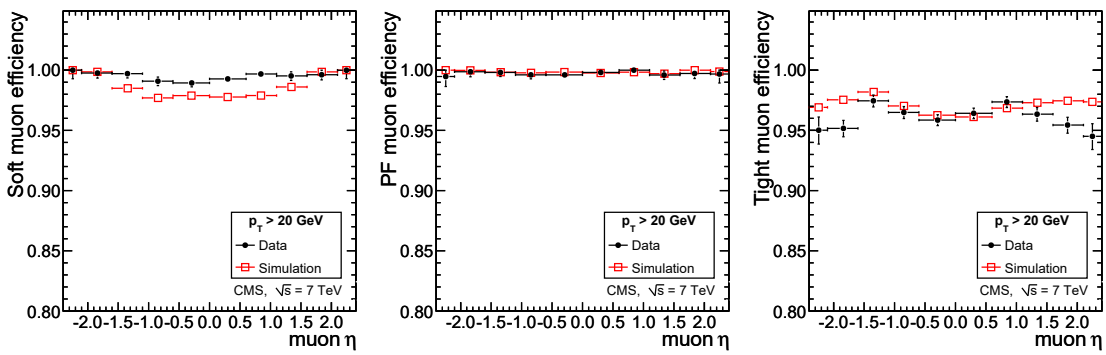

Figure 12. Muon efficiency $\varepsilon_{\mathrm{rec+id}}$ in data and simulation as a function of muon pseudorapidity for Soft Muons (left), Particle-Flow Muons (middle), and Tight Muons (right). The efficiencies were calculated relative to the tracker tracks with $p_{\mathrm{T}} > 20\,\mathrm{GeV}/c$ by applying the tag-and-probe technique to $Z \to \mu^+\mu^-$ events.

5.1.3 Systematic uncertainties

The various contributions to the possible systematic bias in the data-to-simulation ratios of efficiencies calculated using the tag-and-probe method are estimated using simulated and real data.

Bias in the measured efficiencies that could be introduced by the tag-and-probe method and its implementation is studied by comparing the efficiencies obtained by applying the tag-and-probe method to simulated data containing $J/\psi \to \mu^+\mu^-$ ($Z \to \mu^+\mu^-$) decays and various background contributions with the "true" efficiencies computed by simple counting of the passing and failing probes in $J/\psi \to \mu^+\mu^-$ ($Z \to \mu^+\mu^-$) MC events. The difference in the efficiencies is less than 0.5% for muons from $J/\psi \to \mu^+\mu^-$. It is also less than 0.5% for most muons from $Z \to \mu^+\mu^-$

2012 JINST 7 P10002

($20 < p_T < 60\,\text{GeV}/c$), and less than 1.5% for the others. The differences are compatible with zero within the statistical uncertainties; hence, no systematic uncertainty is assigned as a result of this test.

For J/ψ events, the efficiencies are recomputed with the tag-and-probe method using a simple Gaussian instead of a Crystal Ball function [28] to model the resonance and with a quadratic polynomial instead of an exponential to model the background. The differences in the efficiencies resulting from this variation in the assumed signal shape are under 0.1%. The efficiencies obtained with a polynomial background shape are systematically ≈1% higher than those obtained using an exponential background. The difference between the two results is taken as a conservative estimate of systematic uncertainty in the background modelling. The same efficiencies have also been recomputed without the requirement that the probe tracks have a MIP signature in the calorimeters. The results are fully compatible with those obtained with a MIP requirement, but have larger uncertainties. Simulation shows that in this low-p_T range tag-and-probe efficiencies estimated with a MIP requirement are systematically higher, by 1–2%, than without a MIP requirement, due to small correlations between the energy deposition in the calorimeters and the number of hits in the muon chambers. This bias cancels out in the data/simulation ratio, so no corrections accounting for it are made.

For $Z \to \mu^+\mu^-$ events, the efficiencies are recomputed using only isolated probe tracks, which reduces the background by a factor of two. The results agree with those from all probes at the level of 0.1%. As a conservative estimate of systematic uncertainty on the plateau efficiencies resulting from the background estimation, the scale of the largest difference between this estimate and that from simulation is taken; this amounts to 0.2% in the barrel and 0.4% in the endcaps.

For J/ψ events, the kinematic distributions of the signal probes are extracted from the distributions of all probes by using the SPlot technique [29]. The distributions were found to be in good agreement with those predicted by simulation, and therefore no systematic uncertainty is assigned to the procedure of averaging the efficiencies for different probes within each (p_T, η) bin.

Possible bias in the measurements of single-muon efficiencies due to the presence of a second, tag muon in the event is studied by changing the separation criteria from the angular separation $\Delta R > 0.5$ to the tighter requirement that the distance between the coordinates of the two muons in the innermost muon station be larger than 2 m and by using only the pairs of muons that bend away from each other in the magnetic field inside the solenoid. The effect on the efficiencies measured using J/ψ events is 1% in the endcaps and 0.3% in the barrel; this difference is taken as an additional systematic uncertainty on the data-to-simulation ratios of efficiencies. The impact on the efficiencies measured using $Z \to \mu^+\mu^-$ events is negligible, and no additional systematic uncertainty is assigned to them.

In the measurements of efficiencies using $J/\psi \to \mu^+\mu^-$ events, no attempt is made to separate promptly produced J/ψ from those originating from the decay of b quarks. Differences in efficiencies obtained using these two samples of muons are studied in simulation and have been found to be less than 1% and compatible with the statistical uncertainties on each. In the kinematic range over which the measurement is made, the fraction of J/ψ's from the decays of b quarks is always below 50% [18], so the possible effects on the data-to-simulation efficiency ratios are below 0.5%. No additional systematic uncertainty is assigned.

The various contributions to systematic uncertainty were combined in quadrature; the overall uncertainties at the efficiency plateau are shown in table 3.

2012 JINST 7 P10002

5.2 Reconstruction and identification efficiency for nearby muons

If a muon has one or more other muons in its vicinity, their signals in the muon system could overlap, resulting in identification efficiencies lower than for single or well-separated muons. For example, such topologies are common for muon pairs produced in the decays of low-mass resonances such as J/ψ. Another example is hypothetical highly collimated leptons, also referred to as "lepton jets", predicted in different models [30–32] proposed to explain the excess of cosmic-ray leptons in recent astrophysical observations [33–35]. In this section, we report the measurement of reconstruction and identification efficiency for such nearby muons.

The muon identification performance for nearby muons is studied using the data collected during the 2010 LHC data-taking period and compared to the expectations from simulation, in which boosted muon pairs are generated using PYTHIA [8]. Two muon selections are considered: Tracker Muons with at least two tightly matched segments in the muon system, and Tight Muons. Studies on simulated events have shown that the purity of Tracker Muons with two or more well-matched muon segments is similar to that of Tight Muons.

In this study, the efficiency of identifying nearby muons as Tight or Tracker Muons is measured using a sample of dimuons from the decays of low-mass resonances: J/ψ, ϕ, and ρ/ω. These resonances provide muon pairs with kinematic and topological properties similar to those expected for hypothetical collimated muons, notably a small angular separation between the muons.

The sample used for this study consists of pairs of tracker tracks each with p_{T} above 5 GeV/c, associated with the same primary vertex, and for which the invariant mass is in the vicinity of the invariant mass of one of the above resonances. Because the lower mass resonances (ϕ and ρ/ω) have very large combinatorial background, both tracks are also required to have one loosely matched segment in the muon system. To check for any bias introduced by this requirement a measurement was made with tracker tracks from J/ψ decays identified as possible muon candidates by using only the calorimeter information. This gives very similar results hence showing any bias is small. The contribution from the residual background is evaluated from fits to the side bands, by a procedure similar to that used in the tag-and-probe method (section 5.1), and suitably subtracted. The efficiency is defined as the ratio of the number of dimuon candidates passing both the above selection and the muon identification under study to the number of dimuons passing the above selection.

The efficiencies for identifying both muons in the dimuon pair as Tight or Tracker Muons are shown in figure 13. The efficiencies are plotted as a function of the angular separation of the two tracks, $\Delta R = \sqrt{(\Delta\eta)^2 + (\Delta\phi)^2}$, computed at the surface of the first muon station; the collimated muons are expected to populate the range of $\Delta R \lesssim 0.7$. For Tight Muons, a drop in efficiency at small values of ΔR is observed; this inefficiency is introduced by a cleaning procedure used at the seeding stage of the global muon reconstruction to eliminate muon seeds leading to duplicate muons. The efficiency for Tracker Muons, however, remains high at all ΔR values, demonstrating that Tracker Muons are fully adequate for studies involving nearby muons. For both types of selections, the results obtained using different resonances are in good agreement, demonstrating that the dependence of the efficiency on ΔR is not affected by the decay kinematics and combinatorial background. The results of the measurements are also well reproduced by the Monte Carlo simulation.

2012 JINST 7 P10002

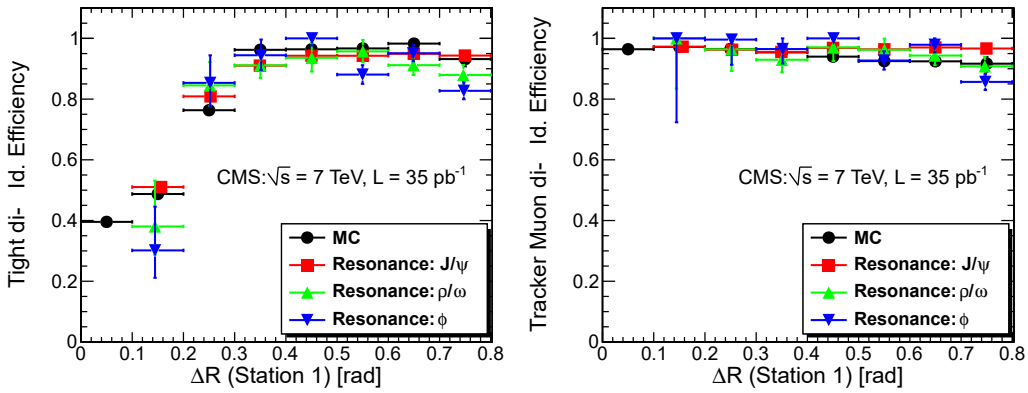

Figure 13. Efficiency for identifying both muons in the dimuon pair as Tight (left) and Tracker (right) Muons as a function of the angular separation of the two tracks computed at the surface of the first muon station. Measurements obtained using J/ψ (squares), ϕ (inverted triangles), and ρ/ω (triangles) are compared with the expectations from the simulation (circles).

5.3 Muon identification probability for particles other than muons

One can obtain pure samples of kaons, pions, and protons from resonances of particle decays such as $K^0_S \to \pi^+\pi^-$, $\Lambda \to p\pi^-$ (and charge conjugate), and $\phi \to K^+K^-$. The resonances are reconstructed using pairs of tracker tracks that are associated with a common decay vertex, with a selection similar to that described in ref. [36]. In Λ decays, the highest momentum track is assumed to be that of the proton. A data sample collected with a jet trigger (minimum p_T of 15 GeV/c) is used, and simulated QCD events, filtered using the same jet trigger, are used for comparison. The simulated events have been reweighted to account for a small difference in the hadron momentum spectrum with respect to the data sample.

We compute the fraction of events in which a hadron track is identified as a Soft Muon, Particle-Flow Muon, or Tight Muon as a function of several relevant track parameters. Background subtraction using resonance sidebands is performed to determine the muon misidentification probability for the particles under study. Invariant mass spectra are fit with a sum of signal and background shapes, using a double Gaussian for the signal and a power law for the background. One fit to the entire mass spectrum is made for each resonance to provide the scale factor between the number of hadrons counted in the sideband region and the background estimation in the signal region. The scaled number of hadrons in the sideband region is then subtracted from the number counted in the signal region, in each bin of the distribution of the hadron track parameter under study. The same background-subtraction procedure is then repeated only for hadrons that share the tracker track with that of a muon. By dividing the sideband-subtracted number of muon-matched hadrons by the sideband-subtracted number of hadrons before any matching to muons, we obtain a misidentification probability for a given hadron type. The same method is applied to events in data and simulation.

In addition to punch-through and decay in flight, there is a third mechanism by which hadrons can be misidentified as prompt muons. This mechanism is random matching between the hadron track in the inner tracker and a track stub in the muon system from one of the other tracks in the jet

2012 JINST 7 P10002

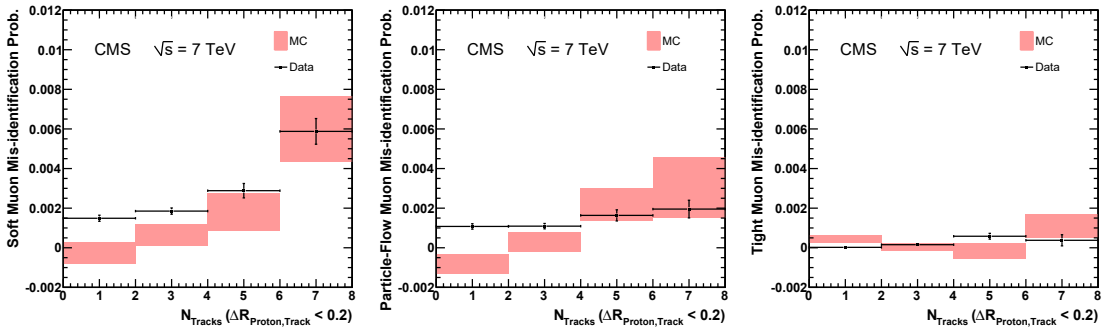

Figure 14. The fraction of protons that are misidentified as a Soft Muon (left), Particle-Flow Muon (centre), or Tight Muon (right) as a function of N_{Tracks}, where N_{Tracks} represents the number of tracks in the vicinity of the proton track (with $\Delta R = \sqrt{(\Delta\eta)^2 + (\Delta\phi)^2} < 0.2$). Only protons with $p > 3\,\text{GeV}/c$ are included. The first bin includes events with $N_{\text{Tracks}} = 0$ and 1, the second bin includes those with $N_{\text{Tracks}} = 2$ and 3, etc. The uncertainties indicated by the error bars (data) and shaded boxes (PYTHIA simulation) are statistical only. Negative values arise from statistical fluctuations in the number of events in the signal and sideband regions.

that may be due to a muon. The frequency of random matching is sensitive to the particular event topology of the sample. For example, in jet-triggered events, the increase in the average number of tracks per event in comparison to minimum-bias-triggered events leads to an increased probability of random matching. To illustrate the effect of random matching, we present the proton-to-muon misidentification probabilities as a function of N_{Tracks} in figure 14, where N_{Tracks} is the number of tracks in the vicinity of the proton track, within a cone of radius $\Delta R < 0.2$. It is clear for both data and simulation that the misidentification probability increases with N_{Tracks} especially in the Soft Muon selection. To remove much of the contribution due to random matching from the probability of misidentifying a hadron as a muon, we impose a requirement of $N_{\text{Tracks}} < 4$ for the rest of the results in this section.

The resulting muon misidentification probabilities are shown in figures 15 and 16 as a function of particle momentum and pseudorapidity, respectively. The shapes of the distributions, well reproduced by simulation, are due to a combination of acceptance (a minimum momentum is required to reach the muon system), the amount of material before the muon system, and the distance available for pions and kaons to decay before reaching the calorimeters. For pions and kaons, the misidentification probabilities are below 1% for all muon selections and decrease at $p \gtrsim 10$–$15\,\text{GeV}/c$ due to fewer of the hadrons decaying to muons within the detector volume. For protons, the probability to be identified as a muon slowly increases with momentum but remains low in the accessible momentum range, which confirms that punch-through is small and that at low momenta the main reason for misidentification of pions and kaons is decays in flight, in agreement with the predictions from simulation discussed in section 4. As expected, the misidentification probabilities are found to be independent of the azimuthal angle and the decay length of the mother particle within the statistical uncertainty.

Overall, the probability to misidentify a hadron as a muon is the largest for Soft Muons, decreases slightly for Particle-Flow Muons, and drops significantly for Tight Muons. As shown in section 5.1, the lower misidentification probability for Tight Muon selection comes at the cost of

2012 JINST 7 P10002

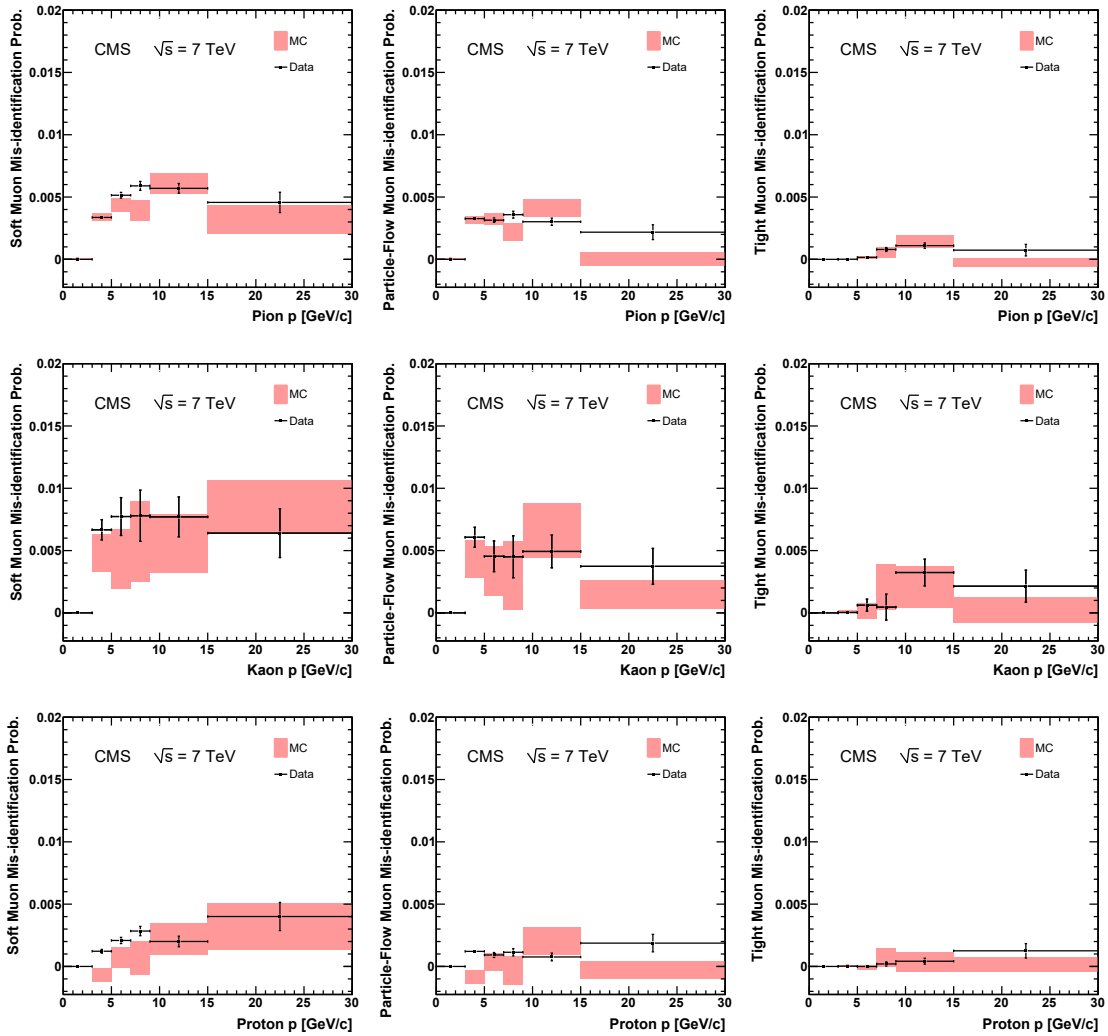

Figure 15. The fractions of pions (top), kaons (centre), and protons (bottom) that are misidentified as Soft Muons (left), Particle-Flow Muons (centre), or Tight Muons (right) as a function of momentum. Only particles with $N_{\text{Tracks}} < 4$ are included. The uncertainties indicated by the error bars (data) and shaded boxes (PYTHIA simulation) are statistical only.

2012 JINST 7 P10002

a few percent lower muon identification efficiency. It is this trade-off between misidentification probability and efficiency that motivates using different muon selections for different analyses.

6 Muon momentum scale and resolution

The measurement of the muon transverse momentum is highly sensitive to the alignment of the tracker and of the muon chambers, to the composition of material and its distribution inside the tracking volume, and to the knowledge of the magnetic field inside and outside the solenoid volume.

The relative bias $\Delta(p_{\text{T}})/p_{\text{T}}$ in reconstructed muon transverse momentum with respect to its true value that could be caused by imperfect knowledge of the magnetic field is generally constant as a function of momentum. Similarly, inaccuracies in the modelling of the energy loss (dependent

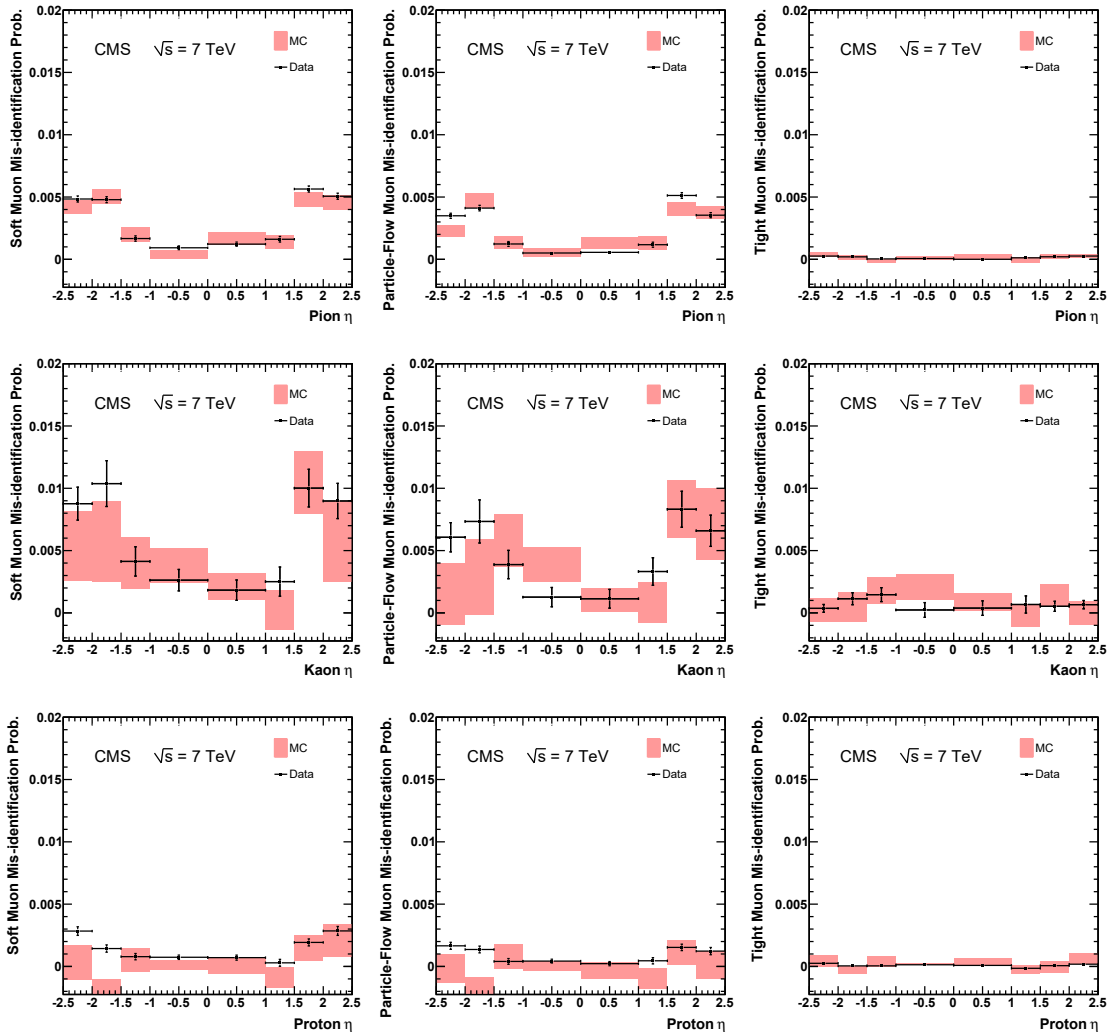

Figure 16. The fractions of pions (top), kaons (centre), and protons (bottom) that are misidentified as Soft Muons (left), Particle-Flow Muons (centre), or Tight Muons (right) as a function of pseudorapidity. Only particles with $p > 3\,\mathrm{GeV}/c$ and $N_{\mathrm{Tracks}} < 4$ are included. The uncertainties indicated by the error bars (data) and shaded boxes (PYTHIA simulation) are statistical only.

on the material distribution) produce relative biases that are essentially independent of the muon momentum. On the other hand, alignment effects produce relative biases that generally increase linearly with momentum.

The momentum scale and resolution of muons are studied using different approaches in different p_{T} ranges. At low and intermediate p_{T} ($\lesssim 100\,\mathrm{GeV}/c$), the mass constraint of dimuon decays from the J/ψ and Z resonances is used to calibrate the momentum scale and measure the momentum resolution. In the high-p_{T} range ($\gtrsim 100\,\mathrm{GeV}/c$), the muon momentum scale and resolution can be measured using cosmic-ray muons (with the exception of the high-$|\eta|$ region).

The lower p_{T} range of the muon spectrum, $p_{\mathrm{T}} \lesssim 10\,\mathrm{GeV}/c$, has been studied in ref. [37]. In this region of p_{T}, alignment effects are less important, and biases in the reconstructed momentum

2012 JINST 7 P10002

mostly arise from uncertainty in the modelling of the detector material and in the description of the magnetic field used when reconstructing the track. Results obtained using J/ψ events show that the overall relative bias in the tracker measurement of the muon p_T in this momentum range is $\approx$0.1%. The muon p_T resolution $\sigma(p_T)/p_T$ was found to be between 0.8% and 3% depending on η and in good agreement with the simulation.

In the intermediate-p_T range, two approaches to study the muon p_T measurement have been developed. The first, referred to as MuScleFit (Muon momentum Scale calibration Fit), produces an absolute measurement of momentum scale and resolution by using a reference model of the generated Z lineshape convoluted with a Gaussian function. The second, called SIDRA (SImulation DRiven Analysis), compares the data with the full simulation of the Z decay to two muons in the CMS detector and provides a way to directly modify the simulation to better match the data. As these two methods have different approaches to the same problem, the difference between the results provides a useful crosscheck and gives an estimate of a systematic uncertainty in the measurement. The results obtained with these methods are reported in section 6.1.

At high p_T (section 6.2), the resolution is determined by comparing cosmic-muon tracks reconstructed independently in the upper and lower halves of the detector, while the scale bias is evaluated by using what is called the "cosmics endpoint method".

6.1 Measurements at intermediate p_T

As previously mentioned, a sample of muons produced in the decays of Z bosons is well suited for measuring the muon momentum scale and resolution in the intermediate range of transverse momentum, $20 < p_T < 100\,\text{GeV}/c$. Muons from Z-boson decays are identified using the Tight Muon selection. They are compared to the simulated sample of $Z \to \mu^+\mu^-$ and Drell-Yan dimuon events reconstructed using the realistic misalignment scenario (see section 2) and passing the same set of muon selection criteria. Tight Muon selection is chosen since it is used in all electro-weak precision measurements in CMS. However using a different selection has no significant impact on the results presented in this section.

Measurements of the muon momentum scale and resolution, reported in sections 6.1.1 and 6.1.2, refer to the p_T of the tracker-only fit as it is the default muon momentum assignment in the range of $p_T < 200\,\text{GeV}/c$ (see section 3). Studies of the resolution of the p_T measured by the muon system only, provided by the standalone-muon track fit, are described in section 6.1.3.

6.1.1 Muon momentum scale

In the MuScleFit approach, the biases in the reconstructed muon p_T are determined from the position of the Z mass peak as a function of muon kinematic variables. Figure 17 shows the position of the peak determined from a fit to a Voigtian (the convolution of a Lorentzian and a Gaussian) in bins of muon ϕ, shown separately for positively and negatively charged muons, and muon η, for both data and simulation.[2] We observe a sinusoidal bias as a function of ϕ,

[2]Note that the peak position returned by the fit is not expected to perfectly match the PDG value of the Z mass. The generator-level Z lineshape is not symmetric around the peak and has a higher tail at lower mass values. When it is convoluted with the detector resolution effects (which can be approximated with a Gaussian), the peak shifts towards lower values. A simplified test performed by convolving the reference lineshape with a Gaussian with $\sigma = 1.5\,\text{GeV}/c^2$ gives a peak position of $90.8\,\text{GeV}/c^2$.

2012 JINST 7 P10002

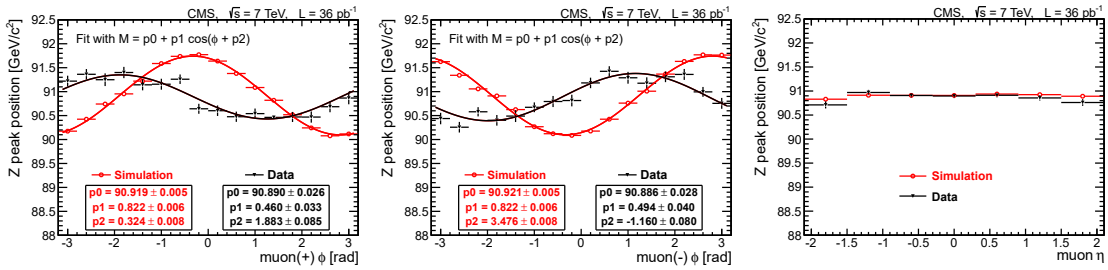

Figure 17. The position of the Z peak reconstructed by the MuScleFit method as a function of muon ϕ for positively charged muons (left), ϕ for negatively charged muons (middle), and η for muons of both charges (right). Results obtained from data (black triangles) are compared with those from simulation (red circles). The ϕ plots also show the results of sinusoidal fits; the values of the fit parameters are given in the text boxes below the labels.

antisymmetric for muons of opposite charges. The maximum shift of the position of the mass peak is about 0.5%. This is significantly larger than the relative bias observed at low p_{T} using the J/ψ events, indicating that the relative bias is p_{T} dependent and that its main source at intermediate p_{T} is the residual tracker misalignment. As explained in section 2, the misalignment scenario used in the simulation was obtained by the alignment procedure similar to that used in the data but was based only on the sample of cosmic-ray muons available at the time of the MC production. This results in a different phase and slightly larger amplitude of the bias in MC simulation. In addition, a small η-dependent bias is also present. This bias exhibits no dependence on muon charge, has a parabolic shape, and is reasonably well reproduced by the Monte Carlo simulation.

MuScleFit uses an unbinned likelihood fit with a reference model to correct the momentum scale. Given the shape of the Z-peak position biases, the following ansatz function is used for the calibration of the momentum scale:

$$p'_{\mathrm{T}} = p_{\mathrm{T}}(1 + b \cdot p_{\mathrm{T}} + c \cdot \eta^2 + q \cdot d \cdot p_{\mathrm{T}} \cdot \sin(\phi + e)), \tag{6.1}$$

where q is $+1$ for μ^+ and -1 for μ^-, and b, c, d, and e are the fit parameters. The model taken as calibration reference is a lineshape of the Z decaying to dimuon pairs as described in ref. [38] and generated with a high granularity in 1001 bins between 71.2 and 111.2 GeV/c^2. Figure 18 shows the results of this calibration procedure on data. The calibrated position of the mass peak is consistent with being flat within the statistical uncertainties, demonstrating that the biases are successfully removed. When averaged over ϕ, the correction is small, and the position of the dimuon invariant-mass peak remains practically unchanged. The same calibration procedure also successfully eliminates momentum scale biases present in the simulation.

The strategy implemented in the SIDRA method consists of modifying the reconstructed invariant-mass spectrum of simulated $\mathrm{Z} \to \mu^+\mu^-$ events by additional shifts and resolution distortions to make it agree with the invariant-mass distribution observed in data. This means that unlike the MuScleFit method, the SIDRA method calibrates only relative biases between data and simulation. This approach assumes that the resolution in data is slightly worse than in simulation and is well suited for the present study. The $\mathrm{Z} \to \mu^+\mu^-$ candidates in data and in simulation are binned according to their reconstructed parameters, and the difference between the two

2012 JINST 7 P10002

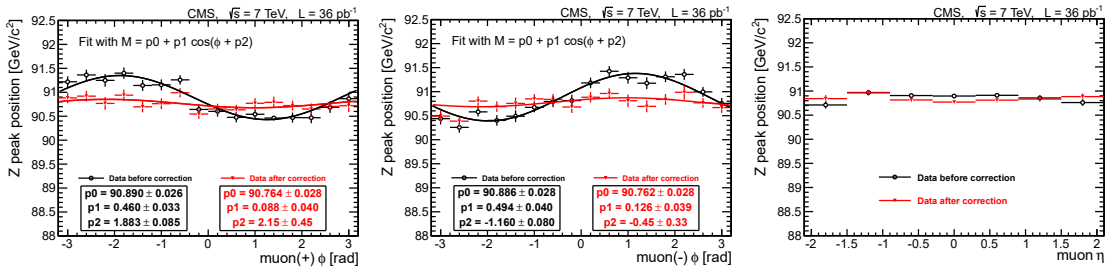

Figure 18. The position of the Z peak in data as a function of muon ϕ for positively charged muons (left), ϕ for negatively charged muons (middle), and η for muons of both charges (right) before (black circles) and after (red triangles) the MuScleFit calibration. The ϕ plots also show the results of sinusoidal fits; the values of the fit parameters are given in the text boxes below the labels.

distributions is minimized by using a binned maximum likelihood fit. At each minimization step, the reconstructed transverse momentum p_{T} of the simulated muons, $p_{\mathrm{T,sim}}$, is modified as follows:

$$\frac{1}{p'_{\mathrm{T,sim}}} = \frac{1}{p_{\mathrm{T,sim}}} + \delta_{\kappa_{\mathrm{T}}}(q,\phi,\eta) + \sigma_{\kappa_{\mathrm{T}}}(q,\phi,\eta)\ \mathrm{Gauss}(0,1)\,, \tag{6.2}$$

where $\delta_{\kappa_{\mathrm{T}}}$ and $\sigma_{\kappa_{\mathrm{T}}}$ are parameters controlling the scale shifts and resolution distortions, respectively, and $\mathrm{Gauss}(0,1)$ denotes a sampling according to a Gaussian of zero mean and unit variance. The fit parameters depend in general on the muon charge q, its azimuthal angle ϕ, and its pseudorapidity η. This ansatz assumes that the differences between the data and the simulation are due to misalignment, with relative effects increasing with p_{T}. This assumption is justified by the excellent agreement between data and simulation for low-mass dimuon resonances [37]. Similarly to the MuScleFit case, several exploratory studies suggest dependencies of the type

$$\delta_{\kappa_{\mathrm{T}}}(q,\phi,\eta) = A + B\eta^2 + qC\sin(\phi-\phi_0)\,; \tag{6.3}$$

$$\sigma_{\kappa_{\mathrm{T}}}(q,\phi,\eta) = A' + B'\eta^2\,, \tag{6.4}$$

where A, B, C, ϕ_0, A', and B' are the parameters to be determined in the fit. The dependence on charge influences the choice of the binning for the fit: since the proposed ansatz function has a charge-dependent term as a function of ϕ, we employ a two-dimensional grid, binning events according to the reconstructed dimuon invariant mass and the azimuthal angle of one of the two muons.

The results of the application of the SIDRA method to the dimuon invariant-mass spectrum in 2010 data are shown in figure 19. Applying SIDRA corrections to the simulation improves agreement with the data. The scale shifts $\delta_{\kappa_{\mathrm{T}}}$ as a function of ϕ and η are shown in figure 20, superimposed with the corresponding shifts obtained with the MuScleFit method. As also shown in figure 17, the phases and amplitudes of the ϕ-dependent biases present in data and in simulation are different: for $p_{\mathrm{T}} \approx M_{\mathrm{Z}}/2$, characteristic of this study, the amplitude of the sinusoidal correction to be applied to the simulation in order to obtain the best match with the data is $\approx$1.5%; differences between the corrections from the two methods do not exceed 0.3%. When examined as a function of η, the scale shifts between data and simulation are consistent with zero in the barrel region and increase with $|\eta|$. For $p_{\mathrm{T}} = M_{\mathrm{Z}}/2$ and $|\eta| > 2$, they are $\approx$0.5% with a difference between the two

2012 JINST 7 P10002

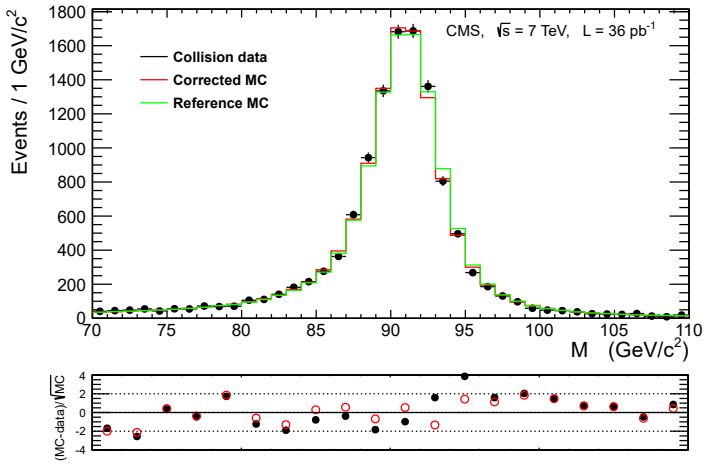

Figure 19. Top: distributions of the dimuon invariant mass for the selected $Z \to \mu^+\mu^-$ candidates in data (points with error bars) and in simulation without ("reference MC") and with ("corrected MC") corrections from SIDRA applied. Bottom: bin-by-bin difference (rebinned for clarity) between the simulation and the data, divided by the expected statistical uncertainty, for MC samples without (filled black circles) and with (open red circles) the SIDRA corrections. The uncertainties are statistical only.

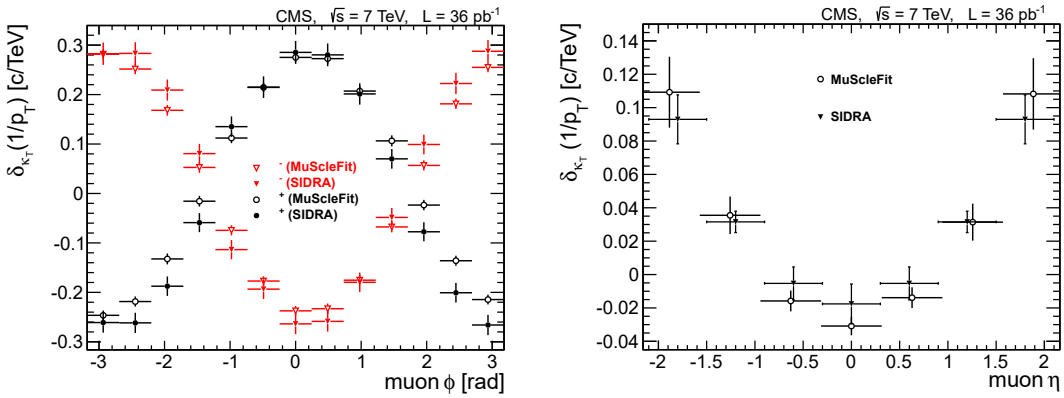

Figure 20. Comparison of the differences between muon momentum scale in data and that in the simulation obtained with the SIDRA and MuScleFit methods as a function of the azimuthal angle for positive and negative muons (left) and pseudorapidity (right). Only statistical uncertainties are shown.

methods of ≈0.1%. When integrated over ϕ and η, the overall difference in muon momentum scale δ_{κ_T} between data and simulation is found to be 0.016 ± 0.012 (stat.) c/TeV for SIDRA and 0.020 ± 0.006 (stat.) c/TeV for MuScleFit.

We use the difference between the MuScleFit and SIDRA relative simulation-to-data corrections as the systematic uncertainty in the measurements of the absolute momentum scale bias obtained with MuScleFit. Another source of systematic uncertainties are the theoretical uncertainties in the reference models used by both SIDRA and MuScleFit, such as uncertainties in parton distribution functions, initial state radiation and higher-order QCD effects, and weak and QED in-

2012 JINST 7 P10002

terference effects. Dedicated simulation studies show that these uncertainties can produce shifts in the Z mass peak position of at most 0.1%, which corresponds to an uncertainty in p_T scale of order $0.1\% \cdot p_T/[91\,\text{GeV}/c]$ if positive and negative muons are equally affected. Summing both types of systematic uncertainties in quadrature, the amplitude of the ϕ-dependent scale correction at $p_T = M_Z/2$ is found to be 0.266 ± 0.010 (stat.) $\pm$ 0.046 (syst.) GeV/c. When integrating over ϕ, the scale correction for the same p_T varies from $\Delta(p_T) = -0.130 \pm 0.022$ (stat.) $\pm$ 0.046 (syst.) GeV/c for $\eta = 0$ to $\Delta(p_T) = 0.234 \pm 0.048$ (stat.) $\pm$ 0.046 (syst.) GeV/c for $|\eta| = 2.1$. The future versions of the alignment workflow will include a Z-mass constraint as an integral part of the alignment procedure, which will strongly reduce the ϕ and η dependence of the momentum bias. Averaged over the whole acceptance, the relative bias in the muon momentum scale is measured with a precision of better than 0.2% and is found to be consistent with zero up to p_T values of 100 GeV/c.

6.1.2 Muon momentum resolution

The techniques used to calibrate the muon momentum scale can also be used to measure the muon transverse momentum resolution. In SIDRA, an extra smearing in data with respect to the resolution predicted by the simulation is obtained from the σ_{κ_T} parameter, as explained in section 6.1.1. The full resolution in data can then be evaluated by applying the scale shifts and extra smearing to the reconstructed p_T of muons in simulation and comparing the obtained p_T values with the "true" p_T. The MuScleFit procedure takes into account the correlations between the two muons, but neglects contributions to the mass resolution from the ϕ and η resolutions, as well as covariance terms. These contributions were found to be small with respect to other terms at the typical p_T range of muons from Z; nevertheless, the systematic uncertainty due to these approximations is estimated from the simulation and accounted for in the final uncertainty of the result. Resolution and scale biases are fit in successive iterations to minimize correlation effects. The assumed functional form to fit the momentum resolution in data contains a term linear in p_T, and separate terms for positive and negative η, each parabolic in η with a common minimum at $\eta = 0$. In the simulation many more events are available, and the η component contains a third term, symmetric about $\eta = 0$.

The calibration of the momentum scale described in section 6.1.1 improves the muon momentum resolution by ≈2%. Figure 21 shows the MuScleFit and SIDRA measurements of muon transverse momentum resolution versus η after correcting for biases in the momentum scale, for both data and simulation. The grey band enveloping MuScleFit results in data shows statistical and systematic uncertainties summed in quadrature. The uncertainties from the choice of a particular function for the resolution shape and the approximations in the method are estimated by comparing the result of the fit using the same function in simulation with the true MC resolution. The bin-by-bin difference between the two results is taken as the systematic uncertainty. The relative difference is on average 6% with an RMS of 4%. Another source of systematic uncertainty included in the band is theoretical uncertainties in the reference models discussed in section 6.1.1. They can produce an extra smearing of the Z mass distribution of at most 0.5%, which can be interpreted as an uncertainty of $0.5\%/\sqrt{2}$ for muons with $p_T \approx M_Z/2$. The statistical and systematic uncertainties are of similar magnitude; the overall (statistical and systematic combined in quadrature) 1σ uncertainty of the measurement varies from 20% to 40% of the resolution in the studied acceptance range.

As can be seen in figure 21, the results obtained with the two methods agree within the uncertainties: the largest difference in the barrel is $(\sigma(p_T)/p_T)_{\text{MuScleFit}} - (\sigma(p_T)/p_T)_{\text{SIDRA}} =$

2012 JINST 7 P10002

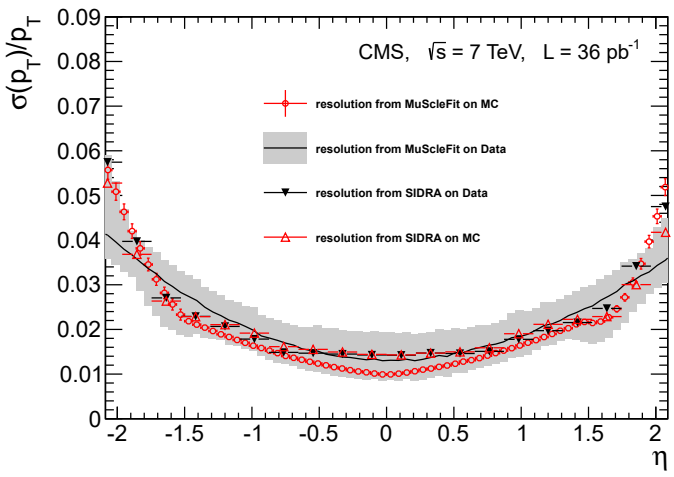

Figure 21. Relative transverse momentum resolution $\sigma(p_{\mathrm{T}})/p_{\mathrm{T}}$ in data and simulation measured by applying the MuScleFit and SIDRA methods to muons produced in the decays of Z bosons and passing the Tight Muon selection. The thin line shows the result of MuScleFit on data, with the grey band representing the overall (statistical and systematic) 1σ uncertainty of the measurement. The circles are the result of MuScleFit on simulation. The downward-pointing and upward-pointing triangles are the results from SIDRA obtained on data and simulation, respectively; the resolution in simulation was evaluated by comparing the reconstructed and "true" p_{T} once the reconstructed p_{T} was corrected for ϕ-dependent biases. The uncertainties for SIDRA are statistical only and are smaller than the marker size.

$0.003 \pm 0.003(\mathrm{stat.} \oplus \mathrm{syst.})$, while in the endcaps it is $-0.018 \pm 0.013(\mathrm{stat.} \oplus \mathrm{syst.})$. The relative p_{T} resolution in the intermediate p_{T} range obtained using MuScleFit is found to be in the range from 1.3% to 2.0% for muons in the barrel and up to ≈6% for muons in the endcaps, in good agreement with the results obtained from simulation. The $\sigma(p_{\mathrm{T}})/p_{\mathrm{T}}$ averaged over ϕ and η varies in p_{T} from $(1.8 \pm 0.3(\mathrm{stat.}))\%$ at $p_{\mathrm{T}} = 30\,\mathrm{GeV}/c$ to $(2.3 \pm 0.3(\mathrm{stat.}))\%$ at $p_{\mathrm{T}} = 50\,\mathrm{GeV}/c$, again in good agreement with the expectations from simulation.

6.1.3 Momentum resolution of standalone muons

The momentum resolution for standalone muons is estimated using the p_{T} of the tracker track as reference:

$$R_{\mathrm{sta}}(1/p_{\mathrm{T}}) = \left((1/p_{\mathrm{T}})^{\mathrm{sta}} - (1/p_{\mathrm{T}})^{\mathrm{trk}}\right) \Big/ (1/p_{\mathrm{T}})^{\mathrm{trk}} \ . \tag{6.5}$$

As the resolution of the tracker tracks at low and intermediate p_{T} is expected to be about an order of magnitude better than the resolution of the standalone-muon tracks, eq. (6.5) provides a good estimate of the resolution for standalone muons. The relative difference between the resolutions measured with respect to the tracker-track p_{T} and the true p_{T} was evaluated from simulation and found to be smaller than 1% in the barrel and smaller than 5% in the endcaps.

The sample of muons used for this study is selected from events passing the single-muon trigger with a minimum p_{T} threshold of $5\,\mathrm{GeV}/c$ by applying the standard requirements for Tight Muons (see section 3). Selected muons were subdivided into subsamples according to the p_{T} and η of the tracker track, and a Gaussian fit to the distribution of R_{sta} (eq. (6.5)) is performed for each

2012 JINST 7 P10002

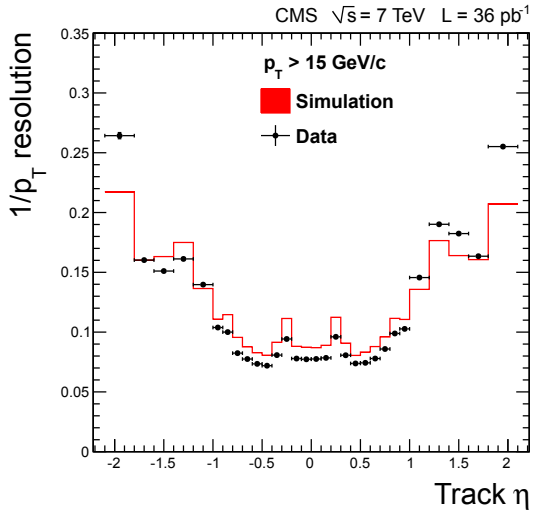

Figure 22. The $1/p_{\mathrm{T}}$ resolution of standalone-muon tracks with respect to tracker tracks, as a function of η of the tracker track for muons with $p_{\mathrm{T}} > 15\,\mathrm{GeV}/c$. Resolution is estimated as the σ of a Gaussian fit to $R_{\mathrm{sta}}(1/p_{\mathrm{T}})$ defined in eq. (6.5).

subsample, with the fit restricted to a range ± 1 RMS about the sample mean. The resolution thus measured using data is compared with results obtained from simulation. Simulated muons are selected from MC samples of QCD, $\mathrm{W} \to \mu\nu$, and $\mathrm{Z} \to \mu^+\mu^-$ events using the same trigger and selection criteria as applied to data.

We report results for standalone muons with a beam-spot constraint applied in the track fit. Figure 22 shows the widths of the Gaussian fits to the distributions of R_{sta} as a function of η for muons with $p_{\mathrm{T}} > 15\,\mathrm{GeV}/c$. The resolution in the barrel remains better than 10% up to $p_{\mathrm{T}} = 100\,\mathrm{GeV}/c$. The overall shape of the η dependence is reproduced by the MC simulation to within 10–15%. Considering that standalone muons are usually not used in physics analyses on their own and mainly serve as a component of the global-muon reconstruction, the performance of which is well described by the simulation, this difference between resolutions for standalone muons in data and simulation is acceptable. A slight asymmetry between resolutions in the negative and positive endcaps is due to small differences in the precision of the alignment of the muon chambers. The bias in the momentum scale of standalone muons, given by the mean values of the fits to the R_{sta} distributions, does not exceed 1% in the barrel region and 5% in the region of $0.9 < |\eta| < 2.1$.

6.2 Measurements at high p_{T}

High-p_{T} muons are an important signature in many searches for new physics, so it is crucial that the performance of their reconstruction, which has some significant differences to that of lower-p_{T} muons (such as an increased role of the muon system in momentum measurement and larger impact of showering) is well understood. While there are few high-p_{T} muons from LHC collisions in the 2010 dataset, cosmic-ray events provide a source of muons with a momentum spectrum extending to quite high p_{T}; cosmic-ray muons having momentum up to a few TeV/c have been

2012 JINST 7 P10002

observed in CMS. Here we present results using cosmic-ray events collected during periods in 2010 when the LHC was not delivering collisions.

6.2.1 Muon momentum resolution from cosmic-ray muon data

Cosmic-ray muons that traverse the entire CMS detector can be used to evaluate the momentum resolution by comparing the momenta reconstructed independently in the upper and lower halves of the muon system, a procedure that was first applied to cosmic-ray muons collected in 2008 [2]. The angular distribution of cosmic-ray muons that traverse the detector is strongly peaked in the vertical direction. To select events in which the muons are most similar to those produced in collision events and used in physics analyses, we only use pairs of tracks that pass close to the interaction point, enforced in practice by requiring each track of the pair to contain hits from at least eight different layers of the silicon strip tracker and at least one hit from the pixel detector. The results presented in this section are for the barrel region only, because few cosmic muons cross both endcaps and pass near the centre of CMS.

To estimate the muon q/p_{T} resolution, we define the relative residual,

$$R(q/p_{\mathrm{T}}) = \frac{(q/p_{\mathrm{T}})^{\mathrm{upper}} - (q/p_{\mathrm{T}})^{\mathrm{lower}}}{\sqrt{2}(q/p_{\mathrm{T}})^{\mathrm{lower}}}, \tag{6.6}$$

where "upper" and "lower" refer to the results of the fits in the two halves of CMS, and the factor of $\sqrt{2}$ accounts for the fact that the two fits are independent. We also define the normalized residual (pull) as

$$P(q/p_{\mathrm{T}}) = \frac{(q/p_{\mathrm{T}})^{\mathrm{upper}} - (q/p_{\mathrm{T}})^{\mathrm{lower}}}{\sqrt{\sigma^2_{(q/p_{\mathrm{T}})^{\mathrm{upper}}} + \sigma^2_{(q/p_{\mathrm{T}})^{\mathrm{lower}}}}}, \tag{6.7}$$

to examine the behavior of the uncertainties from the track fit. To study the various effects as a function of p_{T}, we examine both the truncated sample RMS and a Gaussian fit to the distributions of $R(q/p_{\mathrm{T}})$ and $P(q/p_{\mathrm{T}})$, with the fit range in each p_{T} bin under consideration restricted to the region of ± 1.5 RMS centred on the sample mean. The p_{T} used in the binning is that of the lower tracker-only track.

Figure 23(a) shows the Gaussian widths of the pulls as a function of p_{T} for the tracker-only and global fits, and for the sigma-switch and Tune P algorithms (see section 3). While the cores of the pull distributions are well described by Gaussians, the tails are non-Gaussian, so these widths are slightly smaller than the sample RMS values, which are not shown here. The widths of the pulls for the tracker-only fit are within $\pm 10\%$ of unity over the entire p_{T} range studied, indicating that the track uncertainties are well estimated. The widths of the pulls for the global fit are close to unity in the range of $p_{\mathrm{T}} \lesssim 200\,\mathrm{GeV}/c$, where the tracker information dominates in the fit, and start to become larger at $p_{\mathrm{T}} \approx 200\,\mathrm{GeV}/c$. One important factor contributing to this is that the muon alignment position uncertainties, which account for the precision with which the positions of different detector components are known, are set to zero in the track fits. As a consequence, the total uncertainties are underestimated at high p_{T}. As Tune P uses less information from the muon system than the global fit, the pulls are in between those of tracker-only and global fits.

Figure 23(b) shows the sample means for the distributions of $P(q/p_{\mathrm{T}})$ for the same four muon reconstruction algorithms. The means are consistent with zero up to p_{T} values of $100\,\mathrm{GeV}/c$, above

2012 JINST 7 P10002

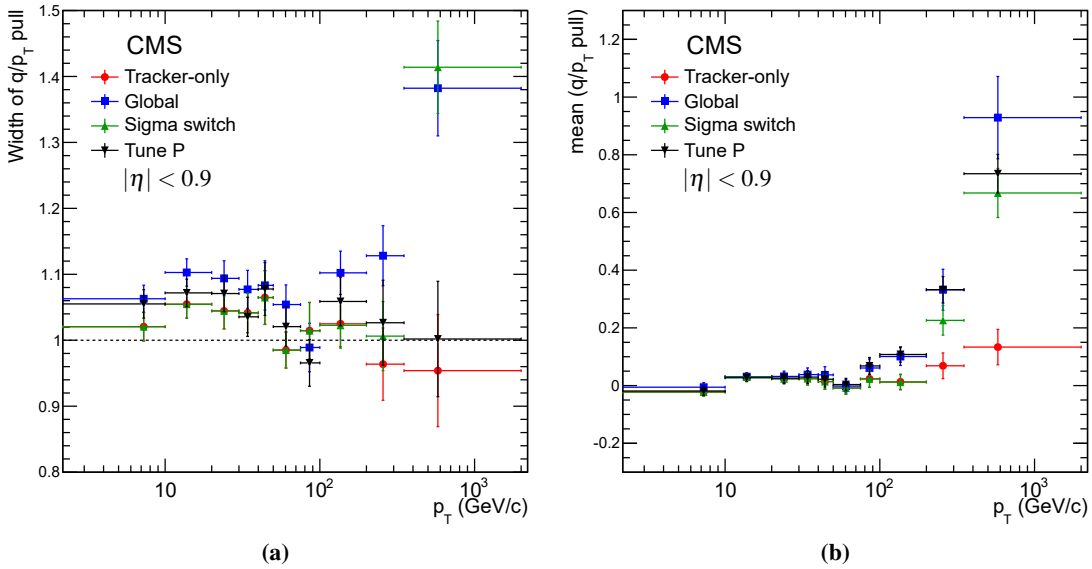

Figure 23. (a) Widths of Gaussian fits to the distributions of the muon q/p_T pulls (as defined by eq. (6.7)) for the tracker-only and global fits, and for the output of the sigma-switch and Tune P algorithms, as a function of the p_T of the muon; (b) the means of the same distributions.

Table 4. Comparison of the fitted Gaussian width σ, sample RMS (truncated at ± 1), and counts in the tails of the $R(q/p_T)$ distribution for 294 muons with measured transverse momentum in the range $350 < p_T < 2000\,\text{GeV}/c$.

Fit/selector	Fitted σ, %	RMS, %	$R(q/p_T) < -1$	$R(q/p_T) > 1$
Tracker-only	7.3 ± 0.3	9.7 ± 0.4	0	0
Global	7.8 ± 0.3	15.6 ± 0.7	4	9
Sigma switch	7.1 ± 0.3	9.8 ± 0.4	0	0
Tune P	6.2 ± 0.3	8.2 ± 0.3	0	0

which fits with muon information begin to show a sizeable bias. The biases seen in the means of the residual distributions $R(q/p_T)$, which are not shown here, are small, indicating that the source of the bias in the means of $P(q/p_T)$ is most likely to be the underestimated uncertainties in the fit. This bias should become smaller as the muon system alignment and its uncertainties are further refined.

Figures 24(a) and (b) show the relative resolution as measured by the Gaussian width and the truncated sample RMS, respectively, for the tracker-only and global fits, and for the sigma-switch and Tune P algorithms as a function of the p_T of the muon. Table 4 summarizes the performance of these algorithms for muons with transverse momentum in the range $350 < p_T < 2000\,\text{GeV}/c$. The Gaussian width gives a measure of the core resolution, while the truncated sample RMS includes the effects of the tails of the distribution; both can be separately important for considerations of momentum resolution, possibly depending on the details of the physics analysis being considered.

2012 JINST 7 P10002

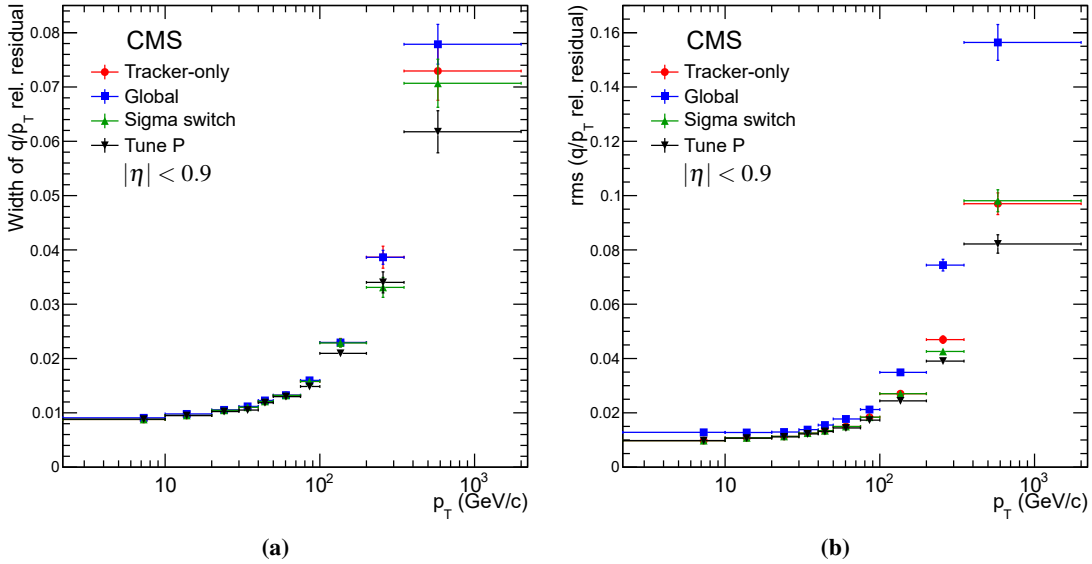

Figure 24. (a) Widths of Gaussian fits of the distributions of the muon q/p_T relative residuals (as defined by eq. (6.6)) for the tracker-only and global fits, and for the output of the sigma-switch and Tune P algorithms, as a function of the p_T of the muon; (b) sample RMS values (truncated at ± 1) of the same distributions.

Muon momentum resolution in the p_T region below approximately 200 GeV/c is dominated by the track measurement in the inner tracker, so one already has the best performance by using the tracker-only fit for low-to-intermediate-p_T muons. At high p_T, the extended path length through the magnetic field between the tracker and the muon system leads to improved resolution, provided that the pattern recognition carefully selects hits in the muon system, avoiding hits due to showers and hits in any muon chamber whose position is poorly known. In figure 24 these two effects are visible: at high p_T, the global fit has larger resolution tails and worse core resolution than the tracker-only fit, while the more selective Tune P performs better than tracker-only and sigma switch in both respects. These results are in agreement with previous studies and expectations [2].

6.2.2 Momentum scale from the cosmics endpoint method

The flux of cosmic-ray muons falls steeply as momentum increases. If there is a q/p_T bias present in the reconstruction at high momentum, the shape of the q/p_T spectrum for cosmic-ray muons will be distorted, with the location of the minimum shifted from zero; the q/p_T bias of high-momentum tracks can be extracted from the location of the minimum. The "cosmic endpoint" method used to estimate the bias is described in ref. [39] and briefly summarized below.

We perform a binned comparison between the q/p_T distributions of the data and of simulated events, introducing various artificial biases into the spectrum of simulated events and calculating the χ^2 as the sum of the squared differences between each bin of the data histogram and the corresponding bin of the new simulated histogram, divided by the value in the simulated bin. To ensure that the extraction of the bias is not affected by possible data-simulation differences in the flux ratio of positive to negative cosmic-ray muons, the q/p_T distribution in the simulation is

2012 JINST 7 P10002

normalized to that in the data separately in the $q/p_{\mathrm{T}} < 0$ and $q/p_{\mathrm{T}} > 0$ regions. We then fit the distribution of the χ^2 values as a function of the introduced bias with a polynomial and take the location of its minimum as the estimate of the bias in data. The one standard deviation statistical uncertainty is computed as the $\Delta(q/p_{\mathrm{T}})$ corresponding to an increase in the function value by $\Delta\chi^2 = 1$ from its minimum.

We report results for the tracker-only reconstruction to compare directly with the measurements performed at intermediate p_{T} (section 6.1). Using cosmic-ray muons reconstructed with $p_{\mathrm{T}} > 200\,\mathrm{GeV}/c$ and passing the selection criteria as described in the previous section, and introducing in the simulation a bias κ of the form

$$q/p_{\mathrm{T}} \rightarrow q/p_{\mathrm{T}} + \kappa \tag{6.8}$$

motivated by the arguments used for the choice of the functional forms presented in eqs. (6.1) and (6.2), the bias in data is found to be -0.20 ± 0.12 (stat.) c/TeV.

To test the robustness of this procedure we generate ensembles of pseudo-experiments using simulated cosmic-ray muons for five equally spaced values of κ from -0.2 to $0.2\ c/\mathrm{TeV}$. For each pseudo-experiment, we repeat the procedure outlined above and calculate a pull as the difference between the estimated bias and the input bias divided by the uncertainty. The distributions of these pulls are consistent with a Gaussian of zero mean and unit width. Considering all the pull distributions tested, we assign the largest deviation from zero mean, 0.02 c/TeV, as a systematic uncertainty on the estimate of the bias. We also consider the following sources of systematic uncertainty and find their impact to be negligible: the resolution model in the simulation, the functional form and the fit range used in finding the χ^2 minimum, and uncertainty in the charge ratio of cosmic-ray muons.

To compare this measurement to that obtained using muons from Z decays (section 6.1), we divide the cosmic-ray muon sample into three bins in ϕ and repeat the above procedure. The results using these ϕ bins and for the whole studied ϕ range are shown in table 5. The results for the momentum bias at high p_{T} obtained with the endpoint method are compatible with those observed at intermediate p_{T}. The accuracy of the measurement is currently statistically limited by the available sample of high-p_{T} cosmic-ray muons and will improve as more cosmic muons are collected.

7 Background from cosmic-ray and beam-halo muons

7.1 Cosmic-ray muons

As shown in the previous section and in ref. [2], cosmic-ray muons are very valuable for studying the performance of the muon system and muon reconstruction tools. At the same time, they are a source of several types of background in physics analyses:

- A cosmic-ray muon passing close to the interaction point can be reconstructed as a collision muon, or as a pair of oppositely charged muons in the upper and lower halves of CMS.

- A muon that is not reconstructed in the tracker (either because it is out-of-time or passes too far from the interaction point) can still be reconstructed as a standalone muon in the muon system and accidentally matched to a tracker track, forming a mismeasured global muon.

2012 JINST 7 P10002

Table 5. The average q/p_T bias obtained with the cosmic endpoint method in three bins of the azimuthal angle ϕ and for the whole studied ϕ range. The first uncertainty quoted is statistical; the second is systematic. Also shown are results obtained with the MuScleFit method (section 6.1) by rescaling p_T of each of the muons from Z decays according to eq. (6.1) and computing the average difference between the rescaled and the original q/p_T values in bins of ϕ. The distribution of muons from Z decays was reweighted to have the same ϕ distribution as that of cosmic-ray muons. The uncertainty quoted is statistical only.

ϕ range, rad	Endpoint method, c/TeV	MuScleFit method, c/TeV
$-\pi < \phi < -2.1$	$-0.14 \pm 0.09 \pm 0.02$	-0.10 ± 0.01
$-2.1 < \phi < -1.05$	$-0.31 \pm 0.09 \pm 0.03$	-0.11 ± 0.01
$-1.05 < \phi < 0$	$-0.09 \pm 0.07 \pm 0.01$	-0.06 ± 0.01
$-\pi < \phi < 0$	$-0.20 \pm 0.12 \pm 0.02$	-0.10 ± 0.01

- A cosmic-ray muon can deposit energy in the calorimeters but avoid detection in the tracking detectors, which would result in, e.g., mismeasured missing transverse energy.

To discriminate between cosmic-ray and collision muons, several quantities can be used, related to either properties of the whole event (vertex quality and track multiplicity) or properties of a muon candidate (transverse impact parameter $|d_{xy}|$, timing information, and collinearity of two tracks reconstructed in the upper and lower halves of the detector and associated with the same muon). Their performance was studied using two different data samples: a sample of muons from collisions with a small (of the order of 1%) contamination from cosmic-ray muons, selected by requiring events with a high-quality reconstructed primary vertex, and a sample of cosmic-ray muons with a contamination from collision events smaller than 0.1%, selected by requiring events without a well-reconstructed primary vertex and with at most two tracks reconstructed in the inner tracker. For comparisons with the data, Monte Carlo samples of $Z \to \mu^+\mu^-$ and Drell-Yan dimuon events were used as representative of muons from collisions for the variables under study. Only events with at least one Global Muon reconstructed with $p_T > 10\,\text{GeV}/c$ and passing loose quality criteria were selected. All distributions were normalized to the number of collision muons in data.

A few examples of variables that can be used to distinguish cosmic muons from collision muons are shown in figure 25 for cosmic-ray muons, muons from collision data, and muons in simulated Z and Drell-Yan events. Figure 25(a) shows the distributions of the transverse impact parameter calculated relative to the beam-spot position d_{xy}. The d_{xy} distribution for cosmic-ray muons is flat, while for collision muons it is strongly peaked at zero. The typical requirement used in muon analyses to suppress the cosmic-muon background is $|d_{xy}| < 0.2$ cm. For illustration, the Z+Drell-Yan MC prediction is shown as well, exhibiting an even narrower transverse impact parameter peak than the inclusive collision muon sample (cf. figure 7) and demonstrating that a tighter and more effective d_{xy} requirement can be applied in specific cases.

If a cosmic muon passes close enough to the centre of the tracker, it is expected to be reconstructed as two tracks ("legs") in the upper and lower halves of CMS with almost equal p_T and opposite directions. The distinct topology of cosmic muons is well represented by the opening angle α, defined as the largest angle between the inner-tracker track of a muon and any other track

2012 JINST 7 P10002

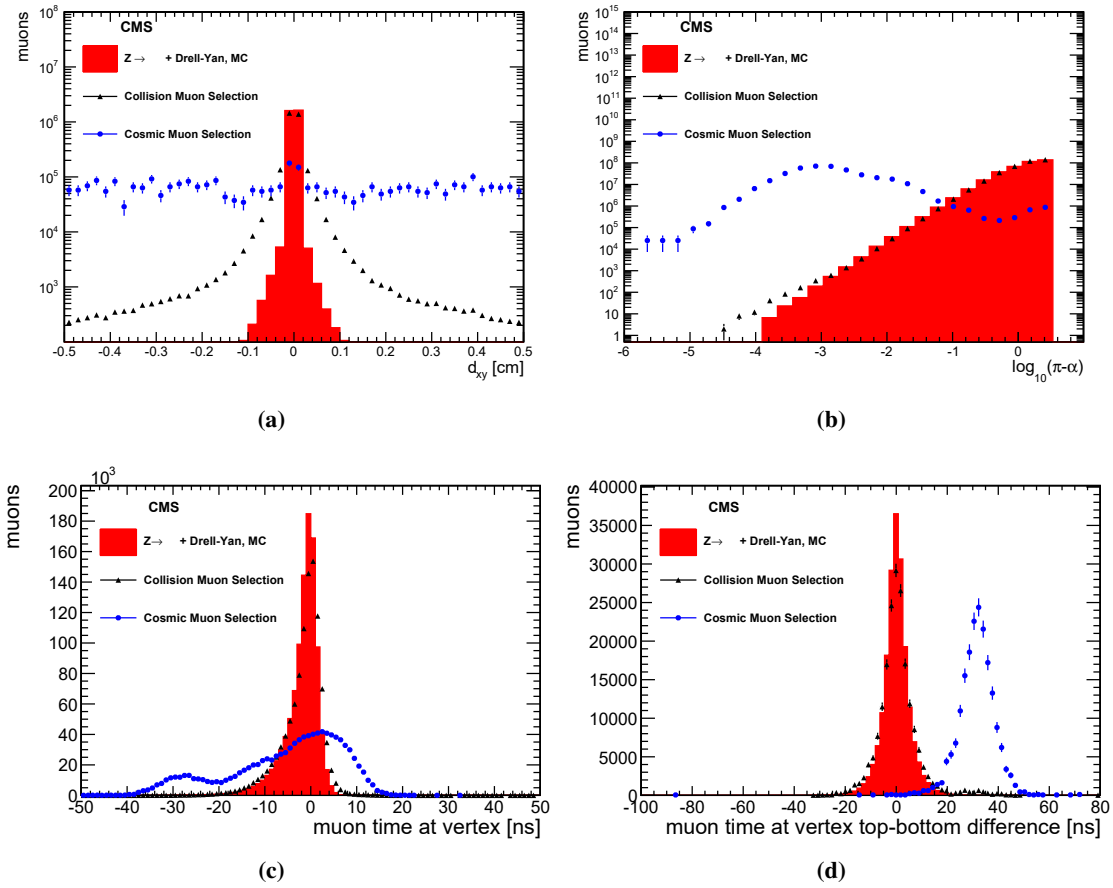

Figure 25. Distributions of variables used for identification of cosmic-ray muons, shown for collision and cosmic-ray muon data samples described in the text, and for Z+Drell-Yan MC samples: (a) muon transverse impact parameter with respect to the nominal beam-spot position; (b) $\log_{10}(\pi - \alpha)$ (see text); (c) muon timing; (d) timing difference between upper and lower muon legs.

in the event. The distributions of $\log_{10}(\pi - \alpha)$ for cosmic-ray and collision muons are shown in figure 25(b). As expected, for most cosmic muons a track opposite in direction could be found, which is not the case for collision muons or muons from simulated Z+Drell-Yan samples. The excess in the number of collision muons observed at the negative tail of the distribution over that predicted is due to a small admixture of cosmic-ray muons present in the data.

Muon timing information can also be used to discriminate between cosmic-ray muons and muons from collisions. The timing distributions observed in data and MC samples are shown in figure 25(c). The muon timing is defined as the time at which a muon would pass the interaction point relative to the time of the bunch crossing. It is calculated from timing information available in the muon system under the assumption that a particle is moving at the speed of light from the centre of the CMS detector outward. Therefore, for collision muons one should expect a distribution peaked around zero with a width determined by the resolution of the time measurement. For cosmic-ray muons the actual arrival time distribution is flat but the reconstructed distribution is also centred around zero. This is due to the trigger and inner-tracker reconstruction being most efficient

2012 JINST 7 P10002

for in-time particles. The additional peak visible at negative time is due to the upper reconstructed legs in events where the lower leg is the source of the trigger. In events where both legs are reconstructed, the timing difference between the upper and lower legs is a good discriminator between dimuons from collisions and cosmic-ray muons, as can be seen in figure 25(d).

Cosmic-ray muon backgrounds must be removed from all physics analyses using muons. For the vast majority of analyses, a simple impact-parameter requirement $|d_{xy}| < 0.2$ cm, which suppresses the contamination from cosmic muons in a sample of Tight Muons with $p_T > 10\,\mathrm{GeV}/c$ to below 10^{-4}, is sufficient. Some analyses, in particular searches for new phenomena involving very energetic muons, need to employ additional cosmic-ray background rejection criteria because the proportion of cosmic muons to collision muons increases as the muon momentum increases. For example, in the search for extra charged gauge bosons (W') decaying to a muon and a neutrino [40], the standard impact-parameter cutoff at 0.2 cm was replaced with a tight cutoff of 0.02 cm. In the search for extra neutral gauge bosons (Z') decaying to muon pairs [41], the impact-parameter requirement was complemented with a selection on the opening angle, $(\pi - \alpha) > 0.02$ rad. As the amount of accumulated data increases, the reach of physics analyses is extending to higher values of dimuon mass and muon momentum; since the spectrum of muons predicted by the Standard Model falls more rapidly with increasing p_T than the cosmic-muon spectrum, more sophisticated methods may become necessary to suppress cosmic-ray muon background to the required level in those kinematic regions. A cosmic-muon identification algorithm has been developed that combines several quantities sensitive to cosmic muons in order to maximize the cosmic-ray muon selection efficiency and minimize misidentification of muons from pp collisions as cosmic-ray muons. This algorithm quantifies the compatibility of any given muon with the hypothesis that it is a cosmic-ray muon; the quantities used are the ones described earlier in this section plus a few others characterizing the event activity and whether there are hits in the opposite (upper or lower) half of CMS which could be associated to a muon track by the dedicated cosmic-muon reconstruction algorithm.

Table 6 shows the performance of cosmic-ray muon identification with some typical individual selections and that of the cosmic-muon identification algorithm. The efficiency is defined as the fraction of events identified as cosmic-ray muons by each algorithm in the sample of cosmic-ray muons selected from collision data, as discussed above. The misidentification fraction is the fraction of simulated Z+Drell-Yan events identified as cosmic-ray muons. The first row shows the performance of the back-to-back identification, which requires that the opening angle $\alpha > (\pi - 0.1)$ rad and that $|p_{T1} - p_{T2}|/\sqrt{p_{T1} \cdot p_{T2}} < 0.1$. The second row shows the effect of applying an impact-parameter requirement: muons with $|d_{xy}| > 0.2$ cm are flagged as cosmic-ray muons. This requirement is quite efficient in identifying cosmic-ray muons, while maintaining a low misidentification probability for collision muons. In the third and fourth rows, we show the performance of the cosmic-muon identification algorithm. This algorithm allows the analyzer to tune the identification efficiency and misidentification fraction according to the needs of the analysis. The tight selection minimizes the misidentification at the cost of some loss of efficiency in cosmic-ray muon rejection. The loose selection maximizes cosmic-ray muon rejection efficiency at the cost of some higher misidentification.

2012 JINST 7 P10002

Table 6. The efficiency of cosmic-ray muon identification and misidentification fractions for some relevant individual quantities and the loose and tight versions of the cosmic-muon identification algorithm. Uncertainties are statistical only.

	Efficiency (%)	Misidentification (%)
Back-to-back	89.97 ± 0.13	0.153 ± 0.002
$\lvert d_{\mathrm{xy}} \rvert > 0.2$ cm	99.05 ± 0.04	0.0045 ± 0.0003
Cosmic ID tight	97.58 ± 0.07	0.0001 ± 0.0001
Cosmic ID loose	99.52 ± 0.03	0.153 ± 0.002

7.2 Beam-halo muons

Accelerator-induced backgrounds ("beam halo") contribute to a variety of physics analyses. The CMS detector can identify beam-halo muons that overlap with collision events and might otherwise be considered as part of the collision itself. The CSC system has extensive geometrical coverage in the plane transverse to the beamline and hence can detect halo muons traveling parallel to the beamline as well as muons originating from collisions. An algorithm has been developed to identify beam-halo muons using information from the CSCs available at both the trigger and the reconstruction level. The following three categories of information have proved effective: 1) a dedicated Level-1 beam-halo trigger (based on patterns of hits in the CSC system consistent with a charged particle traveling parallel to the beamline); 2) CSC trigger primitives (patterns of hits within an individual CSC consistent with a traversing charged particle) that are early in time relative to the actual pp collision; and 3) a reconstructed standalone-muon track with a trajectory parallel to the beamline. Requiring any one of these conditions leads to excellent beam-halo muon identification efficiency. We refer to this as *Loose Halo ID*. Requiring any two of these conditions ensures fewer collision muons are spuriously accepted as halo, but at the expense of slightly lower efficiency for true halo muons. This is referred to as *Tight Halo ID*.

The performance of the beam-halo identification algorithms was studied with 2010 collision data and Monte Carlo samples. Simulated beam-halo muons that passed through the barrel or endcap calorimeters were found to satisfy the requirements of the Loose Halo ID 96% of the time, while satisfying the requirements of the Tight Halo ID 65% of the time. To measure these efficiencies in collision data we used $\not{E}_T$-triggered events. Beam-halo muons can induce a large missing energy signal by traversing the barrel or endcap calorimeters at constant ϕ, and thus $\not{E}_T$-triggered data provide an enriched sample of beam-halo muons. A pure sample of beam-halo muons was selected by requiring no reconstructed collision muon in an event and $\not{E}_T > 50\,\mathrm{GeV}$ opposite in ϕ to at least one reconstructed hit in the CSCs. The fraction of muons in the selected sample identified as beam halo was found to be 89% for the Loose and 73% for the Tight Halo ID. Given the number of simplifying assumptions involved in the simulation of beam-halo events, the agreement between the data and the simulation is considered to be satisfactory.

The fraction of simulated minimum-bias events in which a particle produced in a proton-proton collision was misidentified as a beam-halo muon was $\approx 5 \times 10^{-5}$ and $\approx 10^{-7}$ for the Loose

2012 JINST 7 P10002

and Tight Halo ID algorithms, respectively. When evaluated from minimum-bias collision data, these misidentification probabilities were found to be somewhat larger but still small, with values of $\approx 2 \times 10^{-4}$ and $\approx 8 \times 10^{-7}$, respectively.

The probability for a beam-halo muon crossing the CSCs to be misidentified as a collision muon was also evaluated in data and found to be $\approx 10^{-4}$ for Soft Muons with $p_{\mathrm{T}} < 5\,\mathrm{GeV}/c$ and $\lesssim 5 \times 10^{-5}$ for Soft Muons with higher p_{T} and for Tight Muons. Another important number is the fraction of collision events contaminated by beam-halo muons. In 2010, it ranged from $\approx 10^{-5}$ to $\approx 10^{-3}$, depending on the LHC fill, for muon-triggered events [42]; the fraction could be higher by an order of magnitude for hadronic-triggered events, due to the beam-halo muons' role in triggering the event via energy deposited in the calorimeters. Several searches for new physics in CMS [43, 44] employed the beam-halo identification algorithms described above to veto events with beam-halo contamination.

8 Isolation

The requirement that a muon is an isolated particle in the event, meaning that the energy flow in its vicinity is below a certain threshold, can effectively discriminate muons from the decays of W and Z bosons from those produced in heavy-flavor decays and hadron decays in flight. Three different isolation algorithms have been studied:

- *Tracker relative isolation (I^{rel}_{trk}).* This algorithm calculates the scalar sum of the p_{T} of all tracker tracks reconstructed in a cone of radius $\Delta R \equiv \sqrt{(\Delta\varphi)^2 + (\Delta\eta)^2} < 0.3$ centred on the muon track direction. The p_{T} of the muon track itself is not included in the sum. For the muon to be considered isolated, the ratio of the p_{T} sum to the muon track p_{T} is required to be below a certain threshold. Track directions and values of p_{T} are computed at the point of closest approach to the nominal centre of the detector.

- *Tracker-plus-calorimeters (combined) relative isolation (I^{rel}_{comb}).* The discriminating variable is similar to $I^{\mathrm{rel}}_{\mathrm{trk}}$, but the numerator of the ratio also includes the sum of energies measured in ECAL and HCAL towers found within a cone of radius $\Delta R < 0.3$ centred on the muon track direction. The energy deposits associated with the muon track itself are not included in the sum.

- *Particle-flow relative isolation (I^{rel}_{PF}).* The discriminating variable is the sum of the p_{T} of all charged hadrons, the transverse energies E_{T} of all photons, and E_{T} of all neutral hadrons reconstructed by the particle-flow algorithm [21] within a cone of radius $\Delta R < 0.4$ centred on the muon track direction, divided by the muon track p_{T}.

The optimization of the cone sizes was performed independently for the different algorithms, resulting in the different ΔR values mentioned above. Each of these algorithms has features that suit the requirements of different analyses. For example, the tracker-plus-calorimeters relative isolation with a threshold of 0.15 is the algorithm chosen for the measurement of the W and Z cross sections [19]. The search for heavy resonances decaying into muon pairs [41] instead used the tracker relative isolation given that high-energy muons are expected to deposit a significant amount of energy in the calorimeters. Photons emitted in final-state radiation can lead to energy deposited in the ECAL only. An isolation algorithm that uses energy deposits in the inner tracker

2012 JINST 7 P10002

and the HCAL only is not considered in this paper. Analyses involving τ leptons [45, 46] use particle-flow isolation for the muons from the τ decays, since particle flow is used for the global event reconstruction in these analyses.

The efficiency of the various isolation algorithms was measured in data, using a sample of muons from Z decays. Two methods were used: tag-and-probe and the Lepton Kinematic Template (LKT) method. The tag-and-probe method is described in section 5.1. The LKT method [3] is an extension of the random-cone [47] method. It relies on the assumption that the kinematics of muons from decays of W or Z bosons produced in the hard parton scattering is unrelated to accompanying interactions of the other partons in the colliding protons (the underlying event), which are responsible for the energy flow around the muons. An isolation variable can then be computed relative to any specific direction in an event with underlying event activity similar to that of a signal event. Events containing a Z decaying into a pair of muons, with the reconstructed muon tracks and activity associated with them discarded, were used as approximations to underlying events. Directions were drawn from template kinematic distributions of muons obtained from simulation. As every event can be re-used multiple times, the LKT method provides an important cross-check for the results obtained with the tag-and-probe technique, which are statistically limited in some kinematic regions.

An almost pure sample of $Z \to \mu^+\mu^-$ events was obtained by selecting events with a pair of oppositely charged muons that form an invariant mass in a mass region around the nominal Z mass (between 70 and 110 GeV/c^2 for the tag-and-probe method and within 10 GeV/c^2 of the nominal Z mass for the LKT method) and with each muon satisfying the Tight Muon identification criteria. For the tag-and-probe method, the tag muon was also required to be isolated with $I^{\rm rel}_{\rm comb} < 0.15$. A sample of simulated $Z \to \mu^+\mu^-$ and Drell-Yan dimuon events passing the same selection criteria was used for comparisons with the data, with simulated minimum-bias collision events overlaid to reproduce the observed pile-up (PU) distribution.

Figure 26 shows the efficiency of the various isolation algorithms evaluated on muons with $20 < p_{\rm T} < 50$ GeV/c from Z decays as a function of the threshold on the corresponding isolation variable. Results obtained with the tag-and-probe (for all three isolation algorithms) and the LKT (for $I^{\rm rel}_{\rm trk}$ and $I^{\rm rel}_{\rm comb}$) methods are shown for both data and simulation. Efficiencies in data and MC simulation are generally in good agreement, with the difference between the two not exceeding 1.5%. A single exception is the results from the LKT method for low values of the $I^{\rm rel}_{\rm comb}$ threshold, where efficiencies from MC simulation are lower than those from data by up to 4%. The origin of this discrepancy is under study. The ratios of efficiencies obtained on data and on simulation are also reported in figure 26 and can be considered as scale factors to correct MC results. The agreement between the tag-and-probe and LKT results on data is within 1%.

The efficiency of the various isolation algorithms for muons from Z decays is shown as a function of the muon $p_{\rm T}$ and for two threshold values in figure 27 for $I^{\rm rel}_{\rm trk}$, figure 28 for $I^{\rm rel}_{\rm comb}$, and in figure 29 for $I^{\rm rel}_{\rm PF}$. In each of the three figures the ratio between data and MC results is also reported. The two threshold values studied for each isolation algorithm are those most commonly used in physics analyses and correspond approximately to the end of the rapid rise of the efficiency curve and to the beginning of the efficiency plateau shown in figure 26. The results obtained with the tag-and-probe and LKT methods agree within the statistical uncertainties down to the lowest tested muon $p_{\rm T}$ (5 GeV/c). The LKT results, which have very small statistical uncertainties, indicate that

2012 JINST 7 P10002

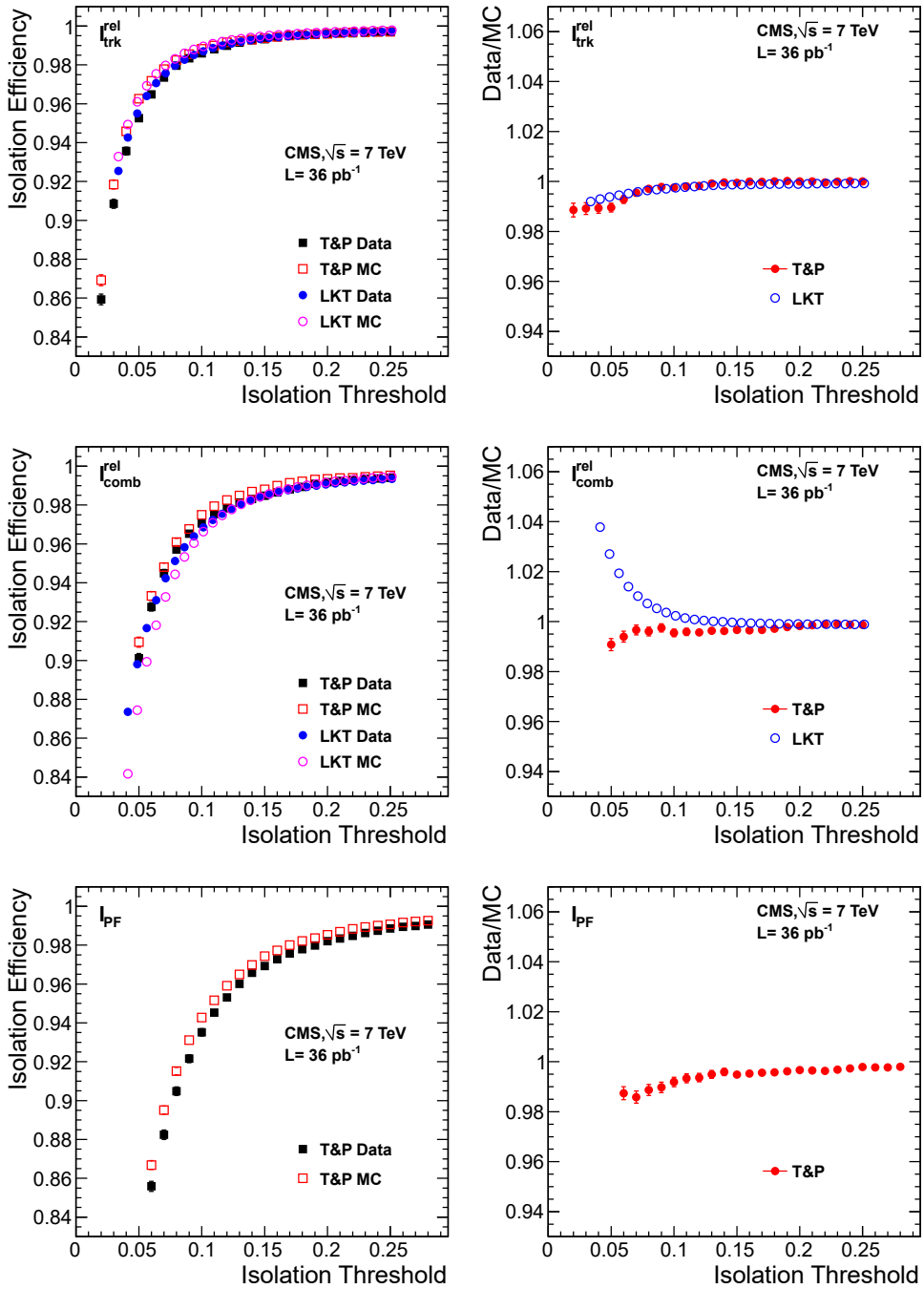

Figure 26. Left: efficiencies of various isolation algorithms for muons with $20 < p_T < 50\,\text{GeV}/c$ from Z decays as a function of the isolation threshold. Results are shown for both data and simulation using the tag-and-probe ("T&P") and Lepton Kinematic Template ("LKT") methods; the LKT method is not used for the particle-flow algorithm. Right: data to simulation ratios. Plots are shown for tracker relative (I^{rel}_{trk}, top), tracker-plus-calorimeters relative (I^{rel}_{comb}, middle), and particle-flow relative (I^{rel}_{PF}, bottom) isolation algorithms. The MC samples include simulation of pile-up events.

2012 JINST 7 P10002

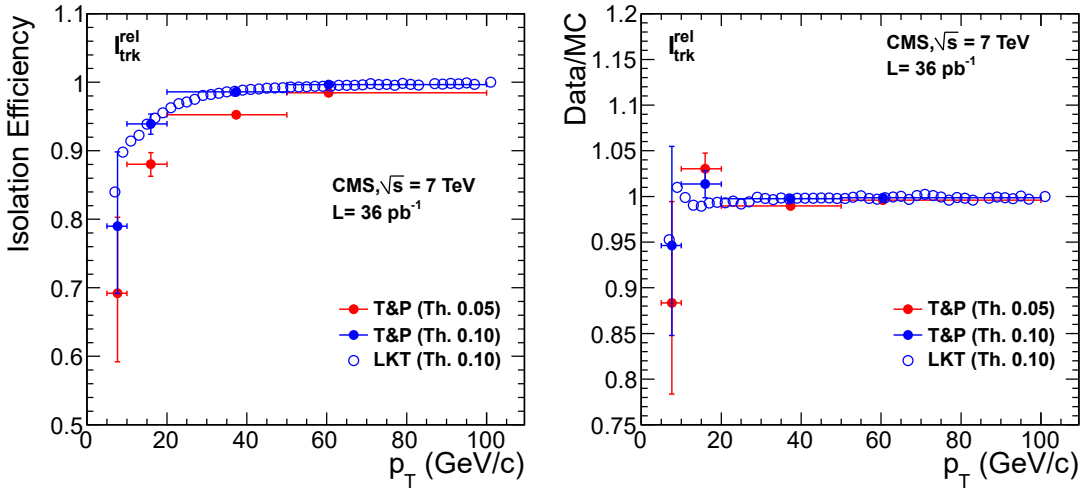

Figure 27. Left: efficiency of tracker relative isolation $I^{\mathrm{rel}}_{\mathrm{trk}}$ for muons from Z decays as a function of muon p_{T}, measured with data using the tag-and-probe ("T&P") method (in bins of [5, 10], [10, 20], [20, 50], and [50, 100] GeV/c) and the LKT method (finer binning). Results corresponding to the threshold values of 0.05 and 0.1 are shown. Right: ratio between data and MC efficiencies. The MC samples include simulation of pile-up events.

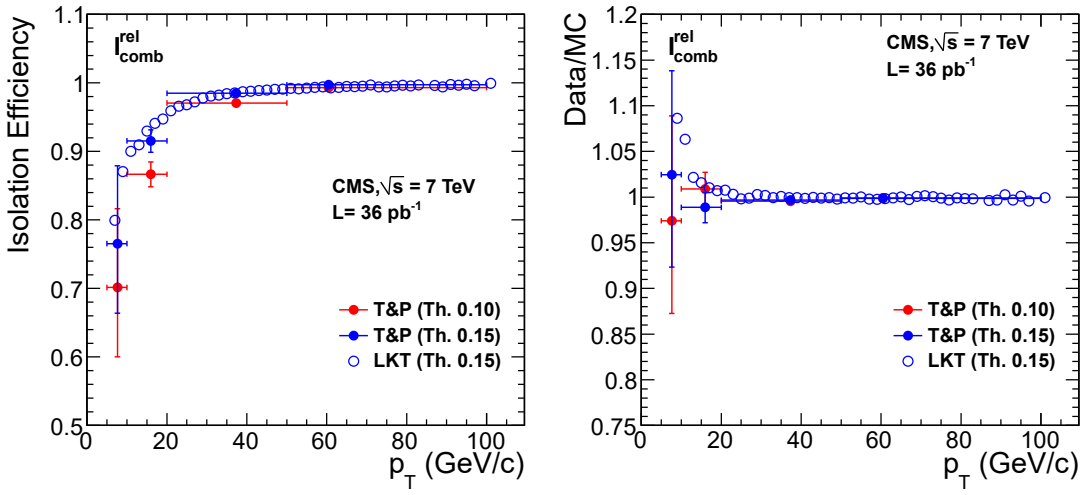

Figure 28. Left: efficiency of tracker-plus-calorimeters relative isolation $I^{\mathrm{rel}}_{\mathrm{comb}}$ for muons from Z decays as a function of muon p_{T}, measured with data using the tag-and-probe ("T&P") method (in bins of [5, 10], [10, 20], [20, 50], and [50, 100] GeV/c) and the LKT method (finer binning). Results corresponding to the threshold values of 0.10 and 0.15 are shown. Right: ratio between data and MC efficiencies. The MC samples include simulation of pile-up events.

for muon p_{T} as low as 5 GeV/c, the agreement between data and MC efficiencies for $I^{\mathrm{rel}}_{\mathrm{trk}}$ ($I^{\mathrm{rel}}_{\mathrm{comb}}$) is within 5% (10%), while for p_{T} greater than 15 GeV/c the agreement is within 1%.

Another important characteristic of the performance of an isolation algorithm is its power to reject muons from typical background events. To estimate the rejection power, a sample

2012 JINST 7 P10002

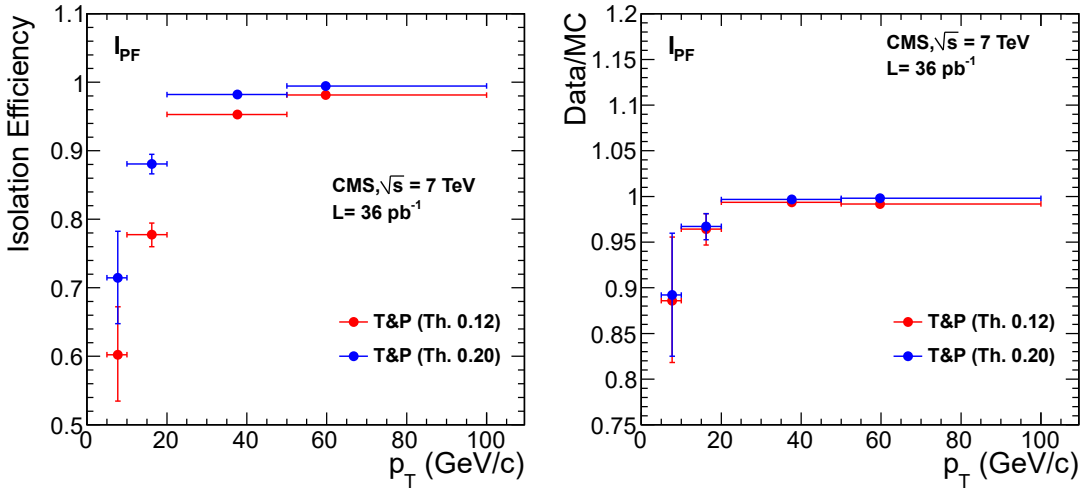

Figure 29. Left: efficiency of particle-flow relative isolation $I_{\mathrm{PF}}^{\mathrm{rel}}$ for muons from Z decays as a function of muon p_{T}, measured with data using the tag-and-probe ("T&P") method. Results corresponding to the threshold values of 0.12 and 0.20 are shown. Right: ratio between data and MC efficiencies. The MC samples include simulation of pile-up events.

enhanced with events from QCD processes is used. These events are selected by requiring the following: one offline reconstructed muon with $20 < p_{\mathrm{T}} < 50\,\mathrm{GeV}/c$ satisfying the Tight Muon requirements; no other Tight Muon reconstructed in the event; at least one particle-flow jet reconstructed with E_{T} greater than 30 GeV; the azimuthal angle $\Delta\phi_{\mu,\not{E}_T}$ between the muon and the missing transverse energy directions smaller than 1.5 rad; and the transverse mass, defined as $M_{\mathrm{T}} = \sqrt{2p_{\mathrm{T}}\not{E}_T(1-\cos(\Delta\phi_{\mu,\not{E}_T}))}$, smaller than $20\,\mathrm{GeV}/c^2$. The last two requirements reduce the contamination from W events significantly. A sample of simulated events from QCD processes, W decays, $\mathrm{Z} \to \mu^+\mu^-$, Drell-Yan, and $t\bar{t}$ production, mixed according to the corresponding cross sections, is used to study the expected composition of the data sample resulting from the above selection and for comparing results obtained from data and MC simulations that include pile-up observed in data. Before isolation requirements are applied, events from QCD processes represent 99.6% of the MC sample. The next most important contributions come from W (0.3%) and Z+Drell-Yan events (0.1%).

Figure 30 shows the efficiency of the various isolation algorithms for muons from Z decays versus the efficiency of the same algorithm for muons from the QCD-enhanced dataset. In both cases muons are required to have $20 < p_{\mathrm{T}} < 50\,\mathrm{GeV}/c$. Results obtained with the tag-and-probe method are reported; the LKT results agree with the tag-and-probe results within 1% for both data and simulation, and are shown only for the $I_{\mathrm{comb}}^{\mathrm{rel}}$ algorithm for comparison. As can be seen in the figure, the best performance for the considered datasets and p_{T} range is given by $I_{\mathrm{PF}}^{\mathrm{rel}}$, followed closely by $I_{\mathrm{comb}}^{\mathrm{rel}}$. For a given signal efficiency, the background rejection evaluated using the MC sample (not shown) is slightly better than that in the data, by up to 0.5% for $I_{\mathrm{trk}}^{\mathrm{rel}}$ and up to 1% for $I_{\mathrm{comb}}^{\mathrm{rel}}$ and $I_{\mathrm{PF}}^{\mathrm{rel}}$. It should be noted that the reported background efficiency includes the absolute 0.4% contamination from truly isolated muons from W/Z decays in the background sample, as described above.

2012 JINST 7 P10002

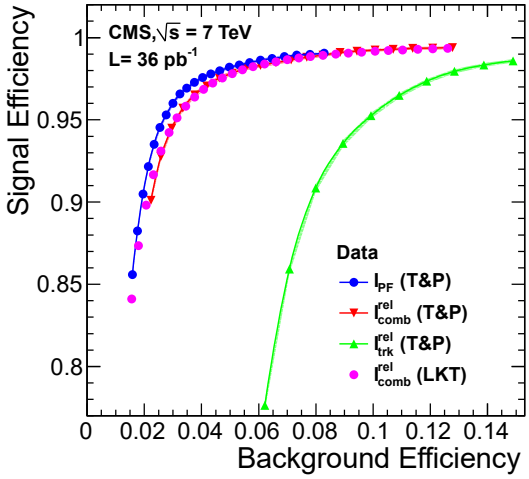

Figure 30. Isolation efficiency for muons from Z decays versus isolation efficiency for muons in the QCD-enhanced dataset described in the text, for tracker relative, tracker-plus-calorimeters relative, and particle-flow relative isolation algorithms. Muons are required to have p_{T} in the range between 20 and 50 GeV/c. The background rejection is limited by the 0.4% contamination from truly isolated muons.

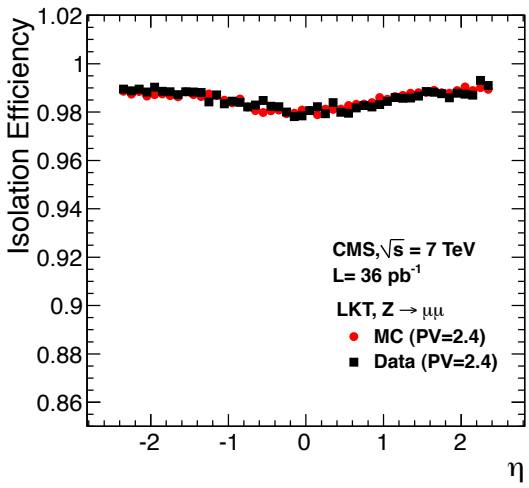

Figure 31. Muon isolation efficiency versus η. Efficiency for muons with p_{T} between 20 and 50 GeV/c from Z decays observed in 2010 data, in which the average number of reconstructed primary vertices (PV) is 2.4, is compared with the results obtained using MC samples with the same average number of primary vertices. The results were obtained with the LKT method using the $I^{\mathrm{rel}}_{\mathrm{comb}}$ algorithm with a threshold of 0.15.

The efficiency of any isolation algorithm features a dependence on the muon pseudorapidity, and this dependence is expected to become more pronounced as the number of pile-up collisions increases. Figure 31 shows the efficiency for muons with $20 < p_{\mathrm{T}} < 50$ GeV/c from Z decays observed in data compared with the results obtained using MC samples having the same distribution of the number of primary vertices as in data, with an average of 2.4. The results are obtained with the LKT method using the $I^{\mathrm{rel}}_{\mathrm{comb}}$ algorithm with a threshold of 0.15. The particular η dependence

2012 JINST 7 P10002

reflects the distribution of transverse energy flow expected for minimum-bias events. Methods to mitigate the impact of pile-up on the performance of isolation algorithms have been developed for higher luminosity running. One such technique is based on the measurement, event-by-event, of the average transverse momentum per unit area ρ added to the event by minimum-bias pile-up collisions [48]. Another technique uses reconstructed tracks and primary vertices to compute a correction factor β to be applied to all or part of the numerator of the isolation variables described above. In both cases, the ρ and β variables allow the energy in the isolation cone due to particles produced in pile-up collisions to be estimated.

An additional advantage of the LKT method is that it can be used to estimate the isolation efficiency for muons produced in any signal process. The basic assumption is made that the kinematics of a muon produced in the leptonic decay of a W, Z, or a heavier new particle is unrelated to the activity of the rest of the event. Under this assumption, the isolation efficiency for muons from such a signal can be inferred from the corresponding efficiency measured using muons from Z, by extrapolating from underlying event activity of Z events to that of the signal. The number of ECAL and HCAL calorimeter towers with transverse energy above threshold can be used as a measure of the event activity. The power of this technique can be appreciated in figure 32, where the isolation efficiency for prompt muons from simulated $t\bar{t}$ events forced to decay leptonically is plotted versus the number of calorimeter towers with $|\eta| < 2.7$ and $E_T > 1\,\text{GeV}$. The isolation efficiency for muons from Z decays (data and MC simulation) is shown superimposed. The efficiencies shown are those of the $I^{\text{rel}}_{\text{comb}}$ algorithm computed by the LKT method. Compared to $t\bar{t}$, Z events are characterized by relatively low occupancies. In the region where the Z and $t\bar{t}$ efficiencies overlap, however, the differences between them do not exceed 2%, and both sets of points tend to align along an approximately straight line. The parameters of this line can be obtained by fitting the points from the Z dataset; the parameters are then used to predict, with an accuracy of a few percent, the isolation efficiency for muons in events with large underlying activity, which cannot be directly measured with the tag-and-probe technique. The pile-up contribution can then be accounted for and corrected by means of the techniques using the ρ and β variables described above.

9 Muon trigger

The CMS trigger system consists of two basic stages: the hardware-based Level-1 trigger [5] and the software-based high-level trigger (HLT) [6].

The Level-1 muon trigger uses signals from all three CMS muon detector systems: DT, CSC, and RPC. It has a latency of 3.2 μs and reduces the rate of inclusive muon candidate events read-out from detector front-end electronics to a few kHz by applying selections on the estimated muon p_T and quality.

In the muon HLT, first a Level-1 trigger object is used as a seed to reconstruct a standalone-muon track in the muon system, leading to an improved p_T estimate. At this point, p_T threshold filters are applied to the standalone (also called Level-2) muon. Then seeds in the inner tracker are generated in the region around the extrapolated Level-2 muon, and tracker tracks are reconstructed. If a successful match is made between a tracker track and the Level-2 muon, a global fit combining tracker and muon hits is performed, yielding a Level-3 muon track on which the final p_T require-

2012 JINST 7 P10002

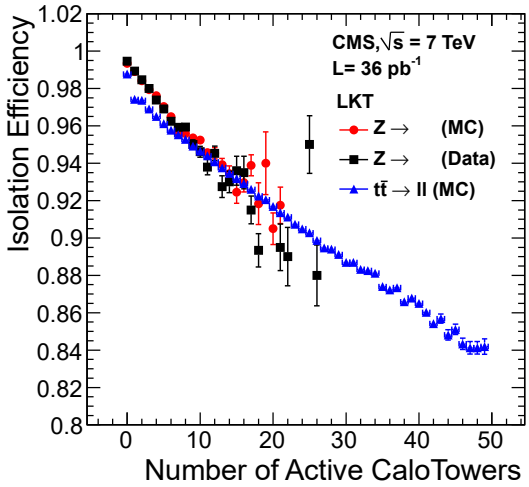

Figure 32. Muon isolation efficiency versus number of calorimeter towers in the region of $|\eta| < 2.7$ having transverse energy larger than 1 GeV. Results for muons with $20 < p_{\mathrm{T}} < 50\,\mathrm{GeV}/c$ from Z decays obtained in data and in simulation are compared with the efficiency for prompt muons in a simulated sample of top pairs decaying leptonically. All results were obtained with the LKT method using the $I^{\mathrm{rel}}_{\mathrm{comb}}$ algorithm with a threshold of 0.15. The MC samples include simulation of pile-up events.

ments are applied. In this way, the rate of recorded inclusive muon events is reduced to a few tens of Hz. The average processing time of the HLT reconstruction is about 50 ms.

In this section we report on trigger efficiency measurements and rejection rates, and compare them to predictions from the simulation. We study the trigger efficiency using two complementary methods: one using tag-and-probe and one using single muons reconstructed offline. The efficiencies are shown separately for the barrel and for the overlap-endcap regions since differences in the trigger response have been observed between them.

9.1 Trigger efficiency using the tag-and-probe method on dimuon resonances

In this subsection, we report the measurements of the trigger efficiency for prompt muons performed by applying the tag-and-probe method described in section 5.1 to muons from the decays of J/ψ and Z resonances. With this method, the trigger efficiency can be measured with respect to any offline muon selection. In the following, we use Soft Muons and Tight Muons as probes to check how efficient the trigger is in selecting muons that can be reconstructed offline. In the case of the Z, the probe muons are also required to be isolated by requiring $I^{\mathrm{rel}}_{\mathrm{comb}}$ to be smaller than 0.15. Measured efficiencies are compared to those evaluated using the MC samples described in section 5.1.

The muon trigger efficiency was studied separately in two regions of muon transverse momentum: below and above $20\,\mathrm{GeV}/c$. In the region of $p_{\mathrm{T}} > 20\,\mathrm{GeV}/c$, the efficiency was measured using a sample of $\mathrm{Z} \to \mu^+\mu^-$ events collected with single-muon triggers. In the region of $p_{\mathrm{T}} < 20\,\mathrm{GeV}/c$, the $\mathrm{J}/\psi \to \mu^+\mu^-$ events collected by the specialized muon-plus-track triggers described in section 2 were used. Several instances of the muon-plus-track trigger have been deployed, with different thresholds on the p_{T} of the tracker track; those with the lower thresholds became prescaled as the instantaneous luminosity increased during 2010. As a result, the amount of data used for the

2012 JINST 7 P10002

Table 7. Level-1, HLT, and overall single-muon trigger efficiencies for Soft Muons in the efficiency plateau ($9 < p_T < 20\,\text{GeV}/c$) for different pseudorapidity regions. The first column shows efficiencies measured from data; the second column shows the ratio between the measurements in data and simulation. The uncertainties are statistical only.

Trigger Level		Tag-and-Probe $J/\psi \to \mu^+\mu^-$	
	Region	Eff. [%]	Data/MC
Level-1	$\lvert\eta\rvert < 2.1$	97.1 ± 0.2	0.990 ± 0.002
	$\lvert\eta\rvert < 0.9$	99.2 ± 0.1	0.995 ± 0.001
	$0.9 < \lvert\eta\rvert < 2.1$	94.5 ± 0.3	0.978 ± 0.004
HLT	$\lvert\eta\rvert < 2.1$	99.1 ± 0.2	0.995 ± 0.002
	$\lvert\eta\rvert < 0.9$	99.2 ± 0.2	0.993 ± 0.002
	$0.9 < \lvert\eta\rvert < 2.1$	99.0 ± 0.3	0.997 ± 0.004
Level-1+HLT	$\lvert\eta\rvert < 2.1$	96.2 ± 0.2	0.985 ± 0.003
	$\lvert\eta\rvert < 0.9$	98.5 ± 0.2	0.989 ± 0.002
	$0.9 < \lvert\eta\rvert < 2.1$	93.6 ± 0.5	0.975 ± 0.005

measurements presented here varies with the p_T region: it corresponds to an integrated luminosity of 0.9 pb^{-1} for $p_T < 3\,\text{GeV}/c$, 0.6 pb^{-1} for $3 < p_T < 5\,\text{GeV}/c$, and 5.3 pb^{-1} for $5 < p_T < 20\,\text{GeV}/c$. The sample of $Z \to \mu^+\mu^-$ events used for the measurements in the range of p_T above $20\,\text{GeV}/c$ corresponds to an integrated luminosity of 31 pb^{-1}.

To evaluate the trigger efficiency, trigger objects must be matched to the muons reconstructed offline. Level-1 muon-trigger candidates are matched to offline muons by position, extrapolating a muon tracker track to the muon system. The HLT muons are matched to the muons reconstructed offline by direction at the vertex. The HLT-only efficiencies are computed matching the probe with the Level-1 candidate and requiring it to be also matched with the HLT candidate. The combined efficiencies of Level-1 and HLT are obtained simply requiring the probe to be matched with the HLT candidate.

9.1.1 Trigger efficiency for Soft Muons

Trigger efficiencies for Soft Muons in the range of $p_T < 20\,\text{GeV}/c$ were measured using muons from the decays of J/ψ particles.

The single-muon trigger efficiencies for Soft Muons are shown in figure 33 as a function of muon p_T, separately for the Level-1 trigger with p_T threshold at $3\,\text{GeV}/c$, the HLT with p_T threshold at $5\,\text{GeV}/c$, and for the full Level-1-HLT online selection. The efficiencies at the plateau, for muons with p_T in the range of $9 < p_T < 20\,\text{GeV}/c$, are reported as a function of muon η in figure 34 and summarized in table 7.

All efficiency curves show a sharp "turn-on" at the trigger p_T threshold, well described by the simulation. As expected, the turn-on is sharper for the HLT, due to an improved p_T resolution. The plateau efficiencies are about 99% for the Level-1 trigger in the barrel region and for the HLT

2012 JINST 7 P10002

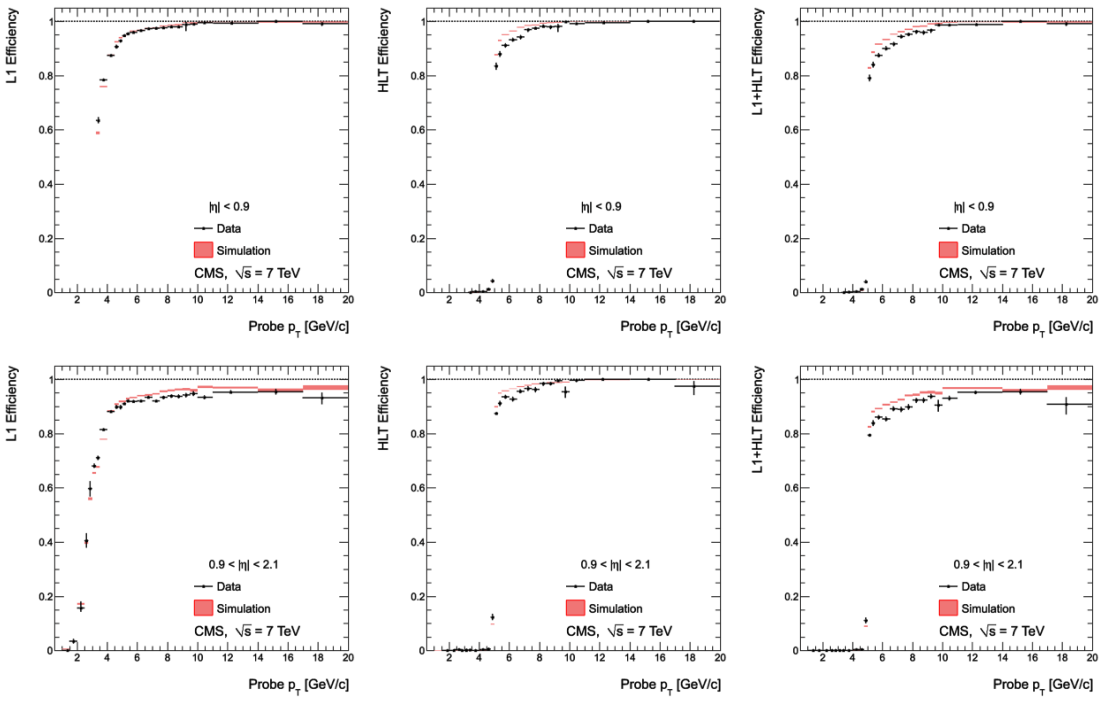

Figure 33. Single-muon trigger efficiencies for Soft Muons as a function of the Soft Muon p_{T} in the barrel (top) and the overlap-endcap (bottom) regions: the efficiency of the Level-1 trigger with p_{T} threshold at 3 GeV/c (left), the efficiency of the HLT with p_{T} threshold of 5 GeV/c with respect to Level-1 (middle), and the combined efficiency of Level-1 and HLT (right). The efficiencies obtained using $\mathrm{J}/\psi \to \mu^+\mu^-$ events (points with error bars) are compared with predictions from the MC simulation ($\pm 1\sigma$ bands); the uncertainties are statistical only.

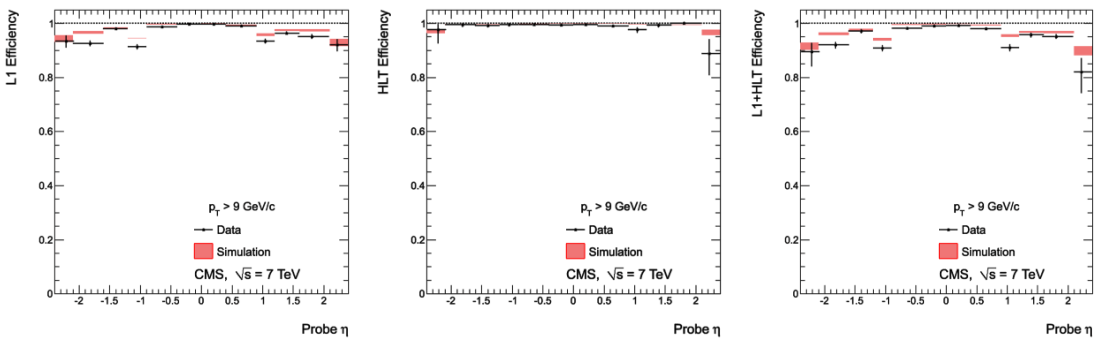

Figure 34. Single-muon trigger efficiencies for Soft Muons as a function of the Soft Muon η, for muons with p_{T} in the range of $9 < p_{\mathrm{T}} < 20$ GeV/c: the efficiency of the Level-1 trigger with p_{T} threshold at 3 GeV/c (left), the efficiency of the HLT with p_{T} threshold of 5 GeV/c with respect to Level-1 (middle), and the combined efficiency of Level-1 and HLT (right). The efficiencies obtained using $\mathrm{J}/\psi \to \mu^+\mu^-$ events (points with error bars) are compared with predictions from the MC simulation ($\pm 1\sigma$ bands); the uncertainties are statistical only.

2012 JINST 7 P10002

in the whole studied pseudorapidity range. The Level-1 efficiency in the overlap-endcap region is slightly lower, at about 95%. Most of the 5% efficiency loss is due to stringent quality criteria used in the selection logic of Level-1 muon triggers during 2010 data taking; these criteria were further optimized during the 2010–11 winter technical stop of the LHC. Measured efficiencies are generally in good agreement with those expected, with the ratios between the two (see table 7) being within 1% of unity. The only exception is a slightly larger, about 2%, difference between data and simulation in the overlap-endcap region due to a few non-operational CSCs not accounted for in the simulation (see section 5.1).

The very forward region, $2.1 < |\eta| < 2.4$, is characterized by higher rates of low-p_{T} muons and poorer momentum resolution. At the nominal LHC luminosity, this region is intended to be used to improve trigger efficiency for events with multiple muons but not to be included in triggering on single muons. In 2010, however, the luminosity and hence the rates of low-p_{T} muons were sufficiently low to allow the single-muon trigger to be extended to include the entire acceptance of muon detectors, up to $|\eta| = 2.4$. In this region of $|\eta| = 2.1$–2.4, the 3:1 ganging of 48 CSC cathode strips into 16 readout channels in the first muon station [49] leads to an ambiguity in p_{T} assignment at Level-1 trigger. The algorithm to resolve this ambiguity was configured with the goal to reduce the rate of muons with overestimated p_{T} to a minimum. As a consequence, the efficiency of the Level-1 triggers in the very forward region was high for triggers with low p_{T} thresholds (about 95% for the Level-1 trigger with p_{T} threshold at 3 GeV/c, see figure 34), but substantially lower for triggers with thresholds above 3 GeV/c (see next section).

9.1.2 Trigger efficiency for Tight Muons

Trigger efficiencies for Tight Muons were measured by applying the tag-and-probe method to $\mathrm{J}/\psi \to \mu^+\mu^-$ events in the region of p_{T} below 20 GeV/c and $\mathrm{Z} \to \mu^+\mu^-$ events in the region of p_{T} above 20 GeV/c.

Using this combination of these two resonances, we can study efficiencies of the Level-1 trigger with p_{T} threshold at 7 GeV/c and of two high-level triggers, with thresholds at 9 and 15 GeV/c. These efficiencies, together with the combined efficiency of the Level-1 and HLT, are shown in figure 35 as a function of muon p_{T}. The efficiencies for muons with $p_{\mathrm{T}} > 20$ GeV/c evaluated using $\mathrm{Z} \to \mu^+\mu^-$ events are shown as a function of muon η in figure 36 and are summarized in the first two columns of table 8.

Like the trigger efficiencies for Soft Muons, the efficiency curves for Tight Muons show a rapid turn-on of efficiencies near the applied threshold: for Level-1 threshold at $p_{\mathrm{T}} = 7$ GeV/c and HLT threshold at $p_{\mathrm{T}} = 9$ GeV/c, the plateau is reached at $p_{\mathrm{T}} \approx 10$ GeV/c. The turn-on region is well reproduced by the simulation. The combined Level-1 and HLT efficiency at the plateau is about 95% in the region of $|\eta| < 0.9$ and about 90% in $0.9 < |\eta| < 2.1$. Most of the efficiency loss occurs at Level-1 and, in particular, in the overlap-endcap region for the reasons described in section 9.1.1. In the very forward region, $2.1 < |\eta| < 2.4$, the single-muon trigger efficiency is about 45%. Most of the losses are due to the underestimation of p_{T} by the Level-1 p_{T}-assignment algorithm described in section 9.1.1; this algorithm has been modified during the 2010–11 winter technical stop of the LHC to yield higher efficiency for muons with p_{T} larger than 20 GeV/c. The difference between the measured and predicted average plateau efficiencies (see table 8) is within 0.5% for the HLT and of the order of 2–3% for the Level-1.

2012 JINST 7 P10002

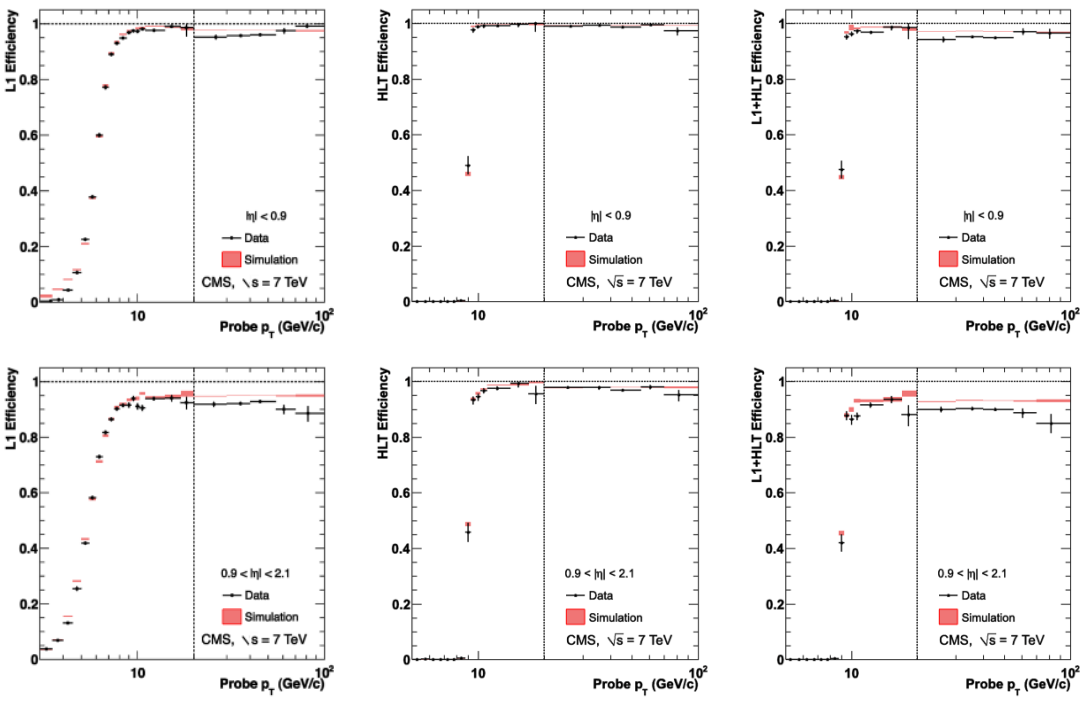

Figure 35. Single-muon trigger efficiencies for Tight Muons as a function of the Tight Muon p_{T} in the barrel (top) and the overlap-endcap (bottom) regions. The measurements are done with the tag-and-probe method, using $\mathrm{J}/\psi \to \mu^+\mu^-$ events for p_{T} below 20 GeV/c and $\mathrm{Z} \to \mu^+\mu^-$ events above. The efficiencies are shown for the following triggers: Level-1 with $p_{\mathrm{T}} > 7$ GeV/c threshold (left), HLT with p_{T} threshold at 9 GeV/c for p_{T} below 20 GeV/c and at 15 GeV/c above (centre), and the combination of the above Level-1 and HLT triggers (right). The efficiencies in data (points with error bars) are compared with predictions from the simulation ($\pm 1\sigma$ bands); the uncertainties are statistical only.

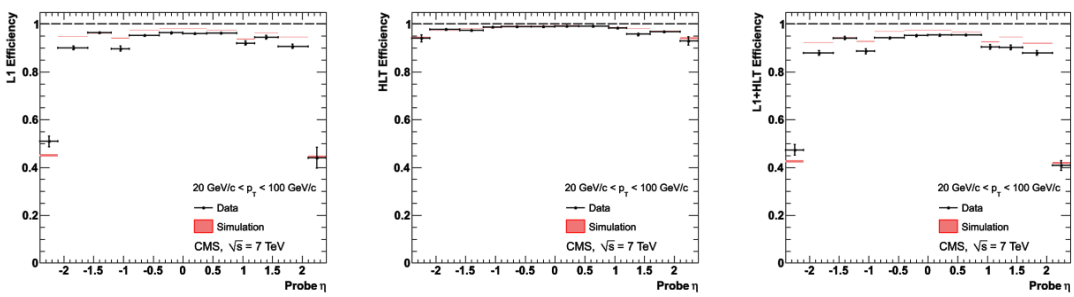

Figure 36. Single-muon trigger efficiencies for Tight Muons with $p_{\mathrm{T}} > 20$ GeV/c as a function of the Tight Muon η: the efficiency of the Level-1 trigger with p_{T} threshold at 7 GeV/c (left), the efficiency of the HLT with p_{T} threshold of 15 GeV/c with respect to Level-1 (middle), and the combined efficiency of Level-1 and HLT (right). The efficiencies obtained using $\mathrm{Z} \to \mu^+\mu^-$ events (points with error bars) are compared with predictions from the MC simulation ($\pm 1\sigma$ bands); the uncertainties are statistical only.

2012 JINST 7 P10002

Table 8. Summary of Level-1, HLT, and overall trigger efficiencies for Tight Muons at the efficiency plateau in different pseudorapidity regions. The results obtained using muons from Z decays and single isolated muons collected with jet triggers are averaged over the p_T range of 20–100 GeV/c; the results from single muons contained in b-tagged jets are reported without an upper p_T limit. For each method, the first column shows efficiencies measured from data; the second column shows the ratios between the estimates in data and in simulation. The quoted uncertainties are purely statistical.

Trigger Level	$Z \to \mu^+\mu^-$		Single isolated μ		Single μ in b jets	
Region	Eff. [%]	Data/MC	Eff. [%]	Data/MC	Eff. [%]	Data/MC
Level-1						
$\lvert\eta\rvert<2.1$	94.1±0.2	0.976±0.002	92.9±0.8	0.966±0.011	94.1±0.3	0.975±0.003
$\lvert\eta\rvert<0.9$	95.9±0.2	0.981±0.002	94.7±1.0	0.971±0.013	95.4±0.3	0.978±0.004
$0.9<\lvert\eta\rvert<2.1$	92.3±0.3	0.971±0.004	91.1±1.2	0.961±0.017	92.2±0.5	0.971±0.006
HLT						
$\lvert\eta\rvert<2.1$	98.2±0.1	0.996±0.001	97.8±0.5	0.993±0.007	94.4±0.3	0.977±0.003
$\lvert\eta\rvert<0.9$	99.0±0.1	0.996±0.001	98.6±0.5	0.996±0.008	96.9±0.3	0.988±0.003
$0.9<\lvert\eta\rvert<2.1$	97.4±0.2	0.995±0.002	97.1±0.8	0.991±0.011	90.5±0.6	0.959±0.007
Level-1+HLT						
$\lvert\eta\rvert<2.1$	92.5±0.3	0.972±0.003	90.8±0.9	0.959±0.013	88.9±0.4	0.953±0.004
$\lvert\eta\rvert<0.9$	95.0±0.3	0.978±0.003	93.3±1.1	0.967±0.015	92.5±0.4	0.967±0.005
$0.9<\lvert\eta\rvert<2.1$	89.9±0.4	0.966±0.004	88.5±1.4	0.952±0.020	83.5±0.8	0.931±0.008

To estimate the effect of multiple interactions on the muon trigger performance, the measurement of the efficiency at the plateau is performed as a function of the number of reconstructed primary vertices in the event. Just as for muon identification, no loss in efficiency has been observed for events containing up to six reconstructed primary vertices.

9.1.3 Systematic uncertainties

The studies of systematic uncertainties in the data-to-simulation ratios of trigger efficiencies closely followed those performed for the muon reconstruction and identification efficiencies (section 5.1.3) and focused on lineshape modelling and background subtraction.

The efficiencies obtained by applying the tag-and-probe method to the simulated samples of muons are compared with the "true" efficiencies computed by simple counting of the passing and failing probes in simulated $J/\psi \to \mu^+\mu^-$ and $Z \to \mu^+\mu^-$ events. The results are in good agreement: the difference in the efficiencies is smaller than 0.1% for muons in both samples, well within the statistical uncertainties of the measurements.

For $J/\psi \to \mu^+\mu^-$ events in data, the efficiencies are recomputed using a simple Gaussian instead of a Crystal Ball function [28] to model the resonance and with a quadratic polynomial instead of an exponential to model the background. Like the results reported in section 5, the

2012 JINST 7 P10002

differences in the efficiencies resulting from this variation in assumed signal shape are smaller than 0.1%; the changes in efficiencies due to a different background parametrization are less than 0.2%. The same test has been made for $Z \to \mu^+\mu^-$ events: using a quadratic polynomial instead of an exponential to model the background results in the efficiency changes of 0.05%. In all cases, the difference between the two results gives an estimate of possible systematic uncertainty due to the modelling of signal and backgrounds.

Finally, for the efficiencies calculated using J/ψ events, the uncertainty due to residual correlation effects between the two muons has been studied by changing the separation criteria as described in section 5.1.3. The effect on the measured ratio of efficiencies in data and in simulation is about 0.3% in the barrel and less than 0.1% in the endcaps.

9.1.4 Efficiency of online muon isolation requirements

To further reduce the trigger rate, isolation criteria can be applied at the HLT. The isolation requirements are based on the calorimeter information for the Level-2 muons and on the pixel tracks for the Level-3 muons [6].

The efficiency of online isolation requirements was evaluated by applying the tag-and-probe technique to muons from Z decays. To obtain the trigger efficiency for muons that are commonly used in physics analyses, the probe is required to pass the Tight Muon selection. Furthermore, to determine the additional effect of online isolation criteria, we require that the probe muon match the trigger object that passed a non-isolated muon trigger of the same threshold.

Figure 37 shows the efficiency of the online isolation selection as a function of the threshold applied to each of the three offline isolation variables described in section 8: the tracker absolute isolation (the numerator of $I^{\mathrm{rel}}_{\mathrm{trk}}$), the tracker-plus-calorimeters relative isolation ($I^{\mathrm{rel}}_{\mathrm{comb}}$), and the particle-flow relative isolation ($I^{\mathrm{rel}}_{\mathrm{PF}}$). The probes are Tight Muons with $|\eta| < 2.1$ and $p_{\mathrm{T}} > 20\,\mathrm{GeV}/c$, matched with the muon trigger candidates that passed the Level-1 trigger with a p_{T} threshold of $7\,\mathrm{GeV}/c$ and HLT with a p_{T} threshold of $9\,\mathrm{GeV}/c$. We then ask whether the matched trigger object passes the combination of the Level-1 and HLT triggers with the same p_{T} thresholds, but also including the isolation criteria.

The efficiency as a function of the threshold on the tracker-based isolation shows a drop around $1\,\mathrm{GeV}/c$. This is a direct consequence of the thresholds implemented in the pixel-track-based isolation at Level-3. For the typical values of the thresholds applied offline (see section 8), an additional efficiency loss due to online isolation requirements is of the order of 4–5%. The measured efficiency distributions are well described by the simulation, with differences of the order of 1% or less over the wide range of threshold values.

9.2 Muon trigger efficiencies from jet-triggered samples

While the tag-and-probe technique using muons from J/ψ or Z allows one to determine trigger efficiencies for prompt signal muons with sufficiently small bias, the momentum range over which the efficiency can be probed is restricted to the momentum range covered by muons from the decays of these resonances.

As an alternative to the tag-and-probe method, it is useful to study the inclusive trigger efficiency for single muons reconstructed offline, in a sample collected using a trigger not involving the muon and tracker systems. In this section, we report trigger efficiencies obtained

2012 JINST 7 P10002

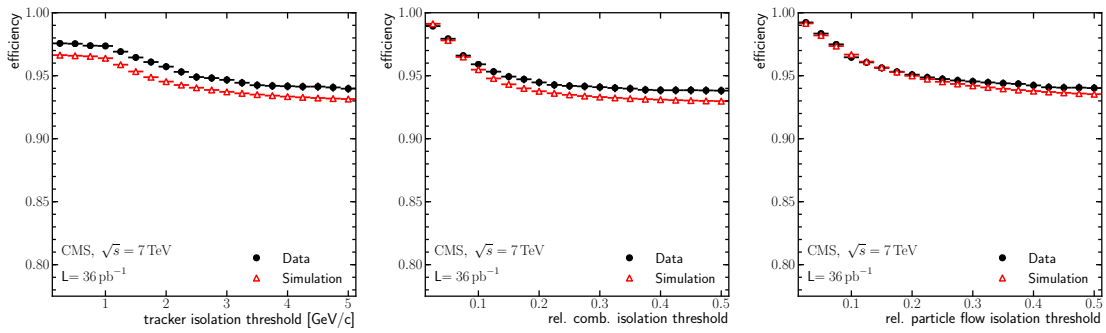

Figure 37. Efficiency of single-muon trigger including isolation requirements for Tight Muons matched with the trigger objects passing trigger without isolation. Efficiencies measured in data (circles) are compared with the predictions of the MC simulation (triangles) as a function of the thresholds applied to the offline isolation variables: tracker absolute isolation (left), tracker-plus-calorimeters relative isolation (middle), and the particle-flow relative isolation (right).

from 2010 data samples recorded with jet triggers, which use only energy measurements in the calorimeters. We use data collected using two single-jet triggers, with thresholds on uncorrected jet p_T of 70 and 100 GeV/c, as well as events in which the sum of all uncorrected transverse energy H_T from jets is larger than 100 GeV. To reduce background, the probes are required to be Tight Muons. They are matched to the HLT muon using the track direction at the vertex. Mismatches are reduced by requiring that only one reconstructed muon be present in the event.

Backgrounds from pion and kaon decays, as well as remaining hadron punch-through, lower the estimated efficiency. From table 2 we expect these backgrounds to be at the level of about 10% for Tight Muons with $p_T > 20$ GeV/c. A higher rejection of these backgrounds can be achieved by applying two alternative and independent additional selections:

- Isolation, which selects mainly muons from W decays and suppresses the heavy-flavour contributions that are typically non-isolated.
- B tagging, which selects muons from semileptonic heavy-flavour decays. Jets are reconstructed by the particle-flow algorithm [21], and a b-tagging criterion [50] is imposed on the jet associated with the muon by requiring a secondary vertex formed from at least two high-quality tracks.

Trigger efficiencies obtained using isolated muons are shown in figure 38 as a function of the reconstructed muon p_T, both for data and for simulated $W \to \mu\nu$ decays. To select isolated muons, the tracker-plus-calorimeters relative isolation is required to be $I^{rel}_{comb} < 0.15$. The p_T spectrum of muons in the sample thus obtained extends beyond 300 GeV/c, thus probing a significantly wider momentum range than the tag-and-probe method. The efficiency beyond $p_T > 20$ GeV/c is consistent with being flat. The average plateau efficiencies are reported in the third and fourth columns of table 8. They can be directly compared to the results from the tag-and-probe method at the $Z \to \mu^+\mu^-$ resonance, which effectively uses isolated muons as well. The results from the two methods are in good agreement.

2012 JINST 7 P10002

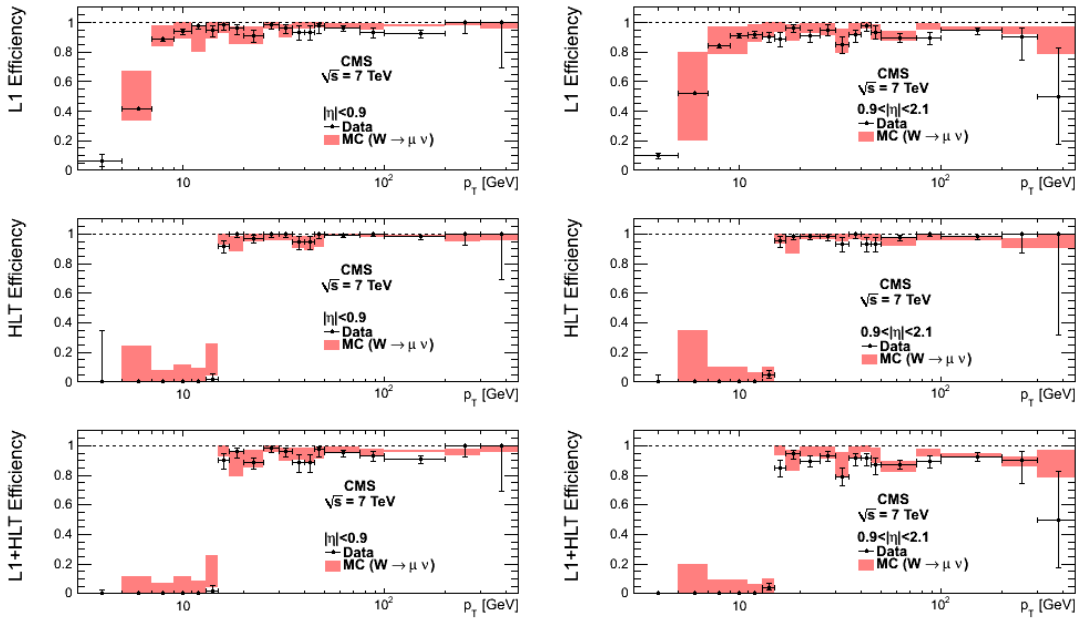

Figure 38. Single-muon trigger efficiencies for Tight Muons passing the offline isolation selection as a function of the muon p_{T}, in the barrel ($|\eta| < 0.9$, left) and the overlap-endcap ($0.9 < |\eta| < 2.1$, right) regions. In both regions the efficiencies for the following triggers are shown: the Level-1 trigger with p_{T} threshold at 7 GeV/c (top), the HLT with p_{T} threshold at 15 GeV/c with respect to the Level-1 (middle), and the combination of above Level-1 and HLT triggers (bottom). The efficiencies in data (points with error bars) are compared with predictions from the simulation ($\pm 1\sigma$ bands); the uncertainties are statistical only.

The trigger efficiencies for Tight Muons in jets, obtained from the b-tagging approach, are shown in figure 39 for data and for a muon-enriched sample of minimum-bias events generated using PYTHIA. The simulation includes the same jet-trigger requirements as used in the data. The shape of the efficiency curves is well reproduced by the simulation. In the plateau above 20 GeV/c the data and simulation agree to about the 5% level. The plateau trigger efficiency as a function of the muon pseudorapidity is shown in figure 40 and summarized in the last two columns of table 8.

The systematic uncertainty due to possible residual background from hadron punch-through and muons from light flavours surviving the b-tagging selection was studied by varying the selection criteria. The results do not change significantly if

- before applying the b-tagging condition, the offline muon requirements are further tightened by imposing more stringent selection criteria on the χ^2 of the tracker-only and the global track fits, and by increasing the minimum required number of pixel and strip tracker hits;

- the b-tagging condition is tightened, by requiring at least three instead of the default two high-quality tracks associated with the secondary vertex;

- only those events are used in which the muon track is matched to the secondary vertex by the b-tagging algorithm.

2012 JINST 7 P10002

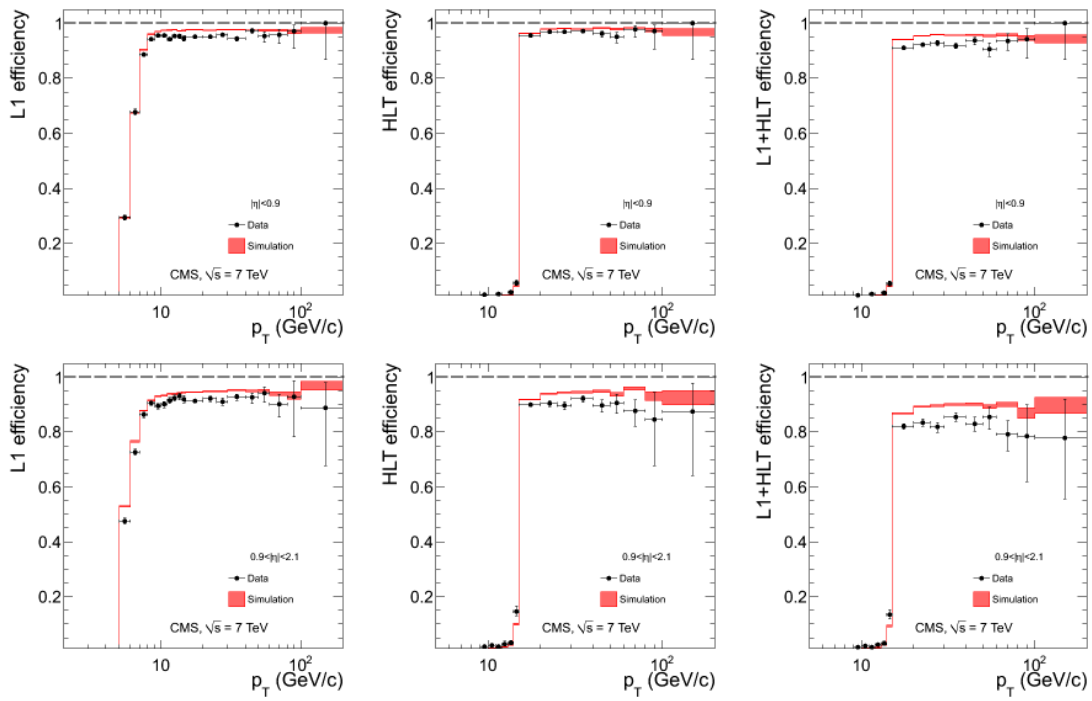

Figure 39. Single-muon trigger efficiencies for Tight Muons contained in b-tagged jets as a function of the muon p_{T}, in the barrel (top) and the overlap-endcap (bottom) regions. The efficiencies are shown for the following triggers: the Level-1 trigger with p_{T} threshold at 7 GeV/c (left), the HLT with p_{T} threshold at 15 GeV/c with respect to the Level-1 (middle), and the combination of above Level-1 and HLT triggers (right). The efficiencies in data (points with error bars) are compared with predictions from the simulation ($\pm 1\sigma$ bands); the uncertainties are statistical only.

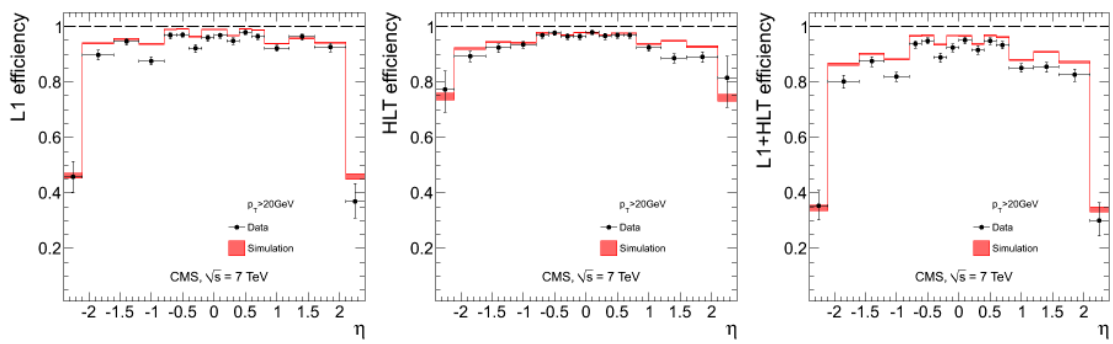

Figure 40. Single-muon trigger efficiencies for Tight Muons contained in b-tagged jets as a function of the muon pseudorapidity, for muons with $p_{\mathrm{T}} > 20$ GeV/c: the efficiency of the Level-1 trigger with p_{T} threshold at 7 GeV/c (left), the efficiency of HLT with p_{T} threshold at 15 GeV/c with respect to the Level-1 (middle), and the combined efficiency of Level-1 and HLT (right). The efficiencies in data (points with error bars) are compared with predictions from the simulation ($\pm 1\sigma$ bands); the uncertainties are statistical only.

2012 JINST 7 P10002

Performing the same checks on the sample of simulated events leads to similar results. In addition, we verified in simulation that the efficiency determined for muons from heavy-flavour decays agrees with that determined by applying the b tagging to the full Monte Carlo sample including backgrounds. This demonstrates that b tagging is very effective in suppressing the background. However, due to pre-selection requirements applied at the generator level, the simulated sample of muon-enriched minimum-bias events used in this study lacks punch-through and light-hadron decays occurring downstream of the ECAL, which results in a smaller impact of the b tagging on the muon selection in simulation than in data. Therefore we consider the difference between the results obtained with and without the b tagging, which is smaller than 1% both in the barrel and endcap, to be a conservative estimate of the systematic uncertainty due to background.

The trigger efficiencies determined for muons in b jets are lower than those obtained for isolated muons in similar ranges of muon transverse momentum. The dependence of trigger efficiency on isolation is demonstrated in figure 41, which shows Level-1 and HLT efficiencies for muons in a jet-triggered sample versus the tracker-plus-calorimeter relative isolation $I^{\mathrm{rel}}_{\mathrm{comb}}$. The thin vertical lines at 0.15 show the typical value defining the isolated muon selection. Without the b tagging, a slight dependence of the Level-1 efficiency on isolation can be seen, due to the residual background contamination; the efficiency becomes flat once the b tagging is applied. The HLT efficiency, on the other hand, has a clear dependence on the muon isolation, even after b tagging. The downward trend has a steeper slope without the b-tagging condition due to the larger background. Similar conclusions are obtained by studying other isolation variables, e.g., the track multiplicity within an angular cone around the muon direction. A worse performance of the single-muon trigger at HLT for muons within high-multiplicity jets is not unexpected. The precision in the matching of the Level-2 muon candidate from the muon chambers with the tracker track from the inner tracker is limited by time constraints dictated by the online operation. Hence, with higher track multiplicity in the tracker matching region the probability of wrong association increases. Nevertheless, the HLT efficiency remains greater than 90% even in the most unfavourable environment of high multiplicities, corresponding to the highest values of $I^{\mathrm{rel}}_{\mathrm{comb}}$ in figure 41.

The ratios of muon trigger efficiencies derived from jet-triggered events in data and in simulation are shown in the last column of table 8. Since muons in jet-triggered events tend to be less isolated than those in muon-triggered events, these corrections are not directly applicable to the muon-triggered events and must themselves be corrected for the difference in isolation in the two samples. This is done by reweighting the jet-triggered events to match the distribution of a given isolation quantity in the muon-triggered events, and then recalculating the corrections. After the reweighting is done, the data-to-simulation efficiency ratios are closer to unity than those before reweighting by 0.01 in the region of $|\eta| < 0.9$ and by 0.03 in the region of $0.9 < |\eta| < 2.1$. These final ratios are in agreement with those obtained with the other two methods, which are shown in table 8. Reweighting the events using either the $I^{\mathrm{rel}}_{\mathrm{comb}}$ distribution or the distribution of the number of tracks in the vicinity of the muon gives statistically compatible results.

The possible effect of event pile-up on the trigger efficiencies was examined by performing the efficiency measurements as a function of the number of good reconstructed primary vertices in the event. No significant dependence, within the statistical uncertainty of about 2%, was found in the available range of one to seven reconstructed primary vertices.

2012 JINST 7 P10002

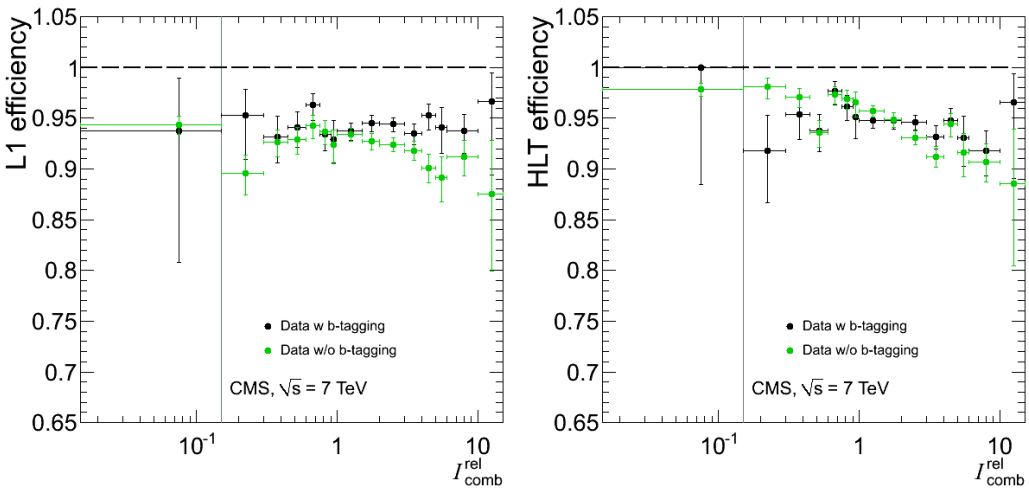

Figure 41. Single-muon trigger efficiencies for Tight Muons with $p_T > 20\,\text{GeV}/c$ and $|\eta| < 2.1$, with and without the further b-tagging selection, as a function of the muon isolation variable I^{rel}_{comb}: the Level-1 trigger (left), and the HLT with respect to the Level-1 (right).

9.3 Trigger rejection rates

The main task of the trigger is to reduce the rate of events to be recorded, while keeping high efficiency for the physics-signal events. The two previous sections focused on the trigger efficiency; in this section we show what fraction of minimum-bias events is rejected as a function of muon trigger p_T threshold at Level-1, Level-2, and Level-3, and compare to the prediction from simulation of minimum-bias events.

The rates of accepted muon triggers were evaluated on a data sample collected using the Level-1 muon trigger with a p_T threshold of $7\,\text{GeV}/c$ and corresponding to an integrated luminosity of 26.5 nb^{-1}. The resulting cross sections are shown in figure 42. At the peak instantaneous luminosity of about 2×10^{32} cm^{-2} Hz, achieved at the end of the LHC operation in 2010, the rate of Level-1 muon trigger with the p_T threshold of $7\,\text{GeV}/c$ was about 2 kHz and the rate of the HLT trigger with the p_T threshold of $15\,\text{GeV}/c$ was slightly below 20 Hz.

To reproduce the trigger rate, the simulation must reproduce the correct sample composition and the correct trigger efficiency, and also must correctly describe the resolution for muons from different sources including the resolution tails. The level of agreement between the Level-1 and HLT trigger performance in data and the Monte Carlo simulation is generally fairly good, with the simulation slightly underestimating the rates at higher thresholds. These results demonstrate that the trigger simulation is a useful tool to predict muon trigger rates and confirm that the performance of the CMS muon trigger system is close to the design expectation.

10 Conclusions

The performance of muon reconstruction, identification, and triggering in CMS has been studied extensively using 40 pb^{-1} of data collected in pp collisions at $\sqrt{s} = 7\,\text{TeV}$ at the LHC in 2010.

2012 JINST 7 P10002

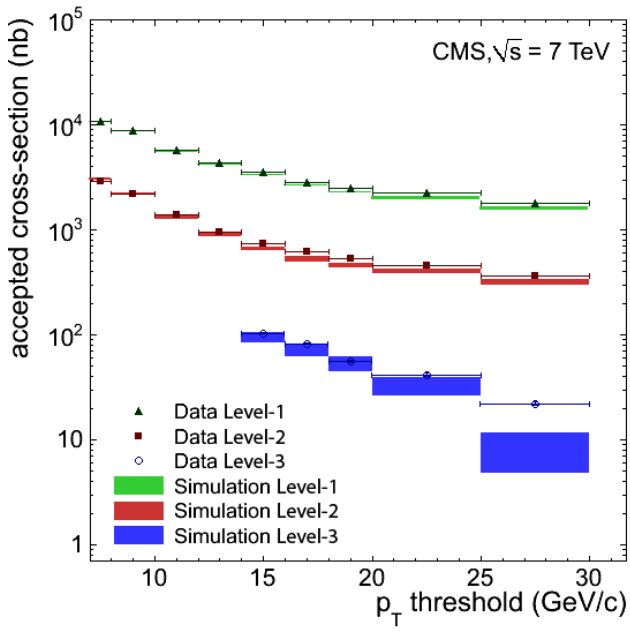

Figure 42. The accepted cross section of events as a function of muon trigger p_T threshold for the actual Level-1, Level-2, and Level-3 muon trigger objects processed online in data, compared to the emulated Level-1 and HLT trigger in simulation. Points corresponding to thresholds of prescaled Level-3 triggers are not plotted.

These data were used to study several representative muon selections, which were chosen as benchmarks covering a wide range of physics analysis needs.

The distributions of kinematic and identification variables for muons reconstructed from inclusive data samples are generally in good agreement with predictions from simulation over the momentum range of $p_T \lesssim 200\,\text{GeV}/c$, including variables sensitive to large hit occupancies in the muon detectors. Identification efficiencies, for muons with p_T larger than a few GeV/c, are above 95% for all selections studied. They are correctly reproduced by the Monte Carlo simulations. Misidentification is lower than 1% for the loosest selection and below 0.1% for the tightest. In the specific case of several nearby muons, where the tightest selection becomes less efficient, an optimized selection was developed to preserve high efficiency with only a minimal increase of misidentification.

Two complementary methods have been developed to evaluate muon momentum scale biases and resolution in the range $20 < p_T < 100\,\text{GeV}/c$, where the momentum measurement is provided by the tracker. The average bias $\Delta(p_T)/p_T$ in the muon momentum scale was measured with a precision of better than 0.2% and was found to be consistent with zero. The relative p_T resolution is between 1.3% to 2.0% for muons in the barrel and better than 6% in the endcaps, in good agreement with simulation. The transverse momentum resolution of tracks reconstructed using information from only muon detectors is better than 10% in the barrel region. At high momenta, the best measurement of muon p_T is obtained by selective use of information from the muon system in addition to that from the inner tracker. The p_T resolution, evaluated in the barrel region using muons from cosmic rays, is better than 10% up to 1 TeV/c.

2012 JINST 7 P10002

Algorithms to identify cosmic and beam-halo backgrounds among collision events were developed and successfully used in physics analyses of 2010 data. The performance of various muon isolation algorithms was shown to be reasonably well modelled by the simulation.

The muon trigger efficiency for isolated muons is better than 90% over the full η range, and is typically substantially better.

In this document we have shown that the performance specifications set out for the measurement of muons in CMS have largely been met. The good performance and detailed understanding of the muon reconstruction, identification, and triggering provides the necessary confidence in all elements of the chain from muon detection to muon analysis, which is essential for searches for physics beyond the Standard Model as well as accurate Standard Model measurements.

Acknowledgments

We wish to congratulate our colleagues in the CERN accelerator departments for the excellent performance of the LHC machine. We thank the technical and administrative staff at CERN and other CMS institutes. This work was supported by the Austrian Federal Ministry of Science and Research; the Belgium Fonds de la Recherche Scientifique, and Fonds voor Wetenschappelijk Onderzoek; the Brazilian Funding Agencies (CNPq, CAPES, FAPERJ, and FAPESP); the Bulgarian Ministry of Education and Science; CERN; the Chinese Academy of Sciences, Ministry of Science and Technology, and National Natural Science Foundation of China; the Colombian Funding Agency (COLCIENCIAS); the Croatian Ministry of Science, Education and Sport; the Research Promotion Foundation, Cyprus; the Estonian Academy of Sciences and NICPB; the Academy of Finland, Finnish Ministry of Education and Culture, and Helsinki Institute of Physics; the Institut National de Physique Nucléaire et de Physique des Particules / CNRS, and Commissariat à l'Énergie Atomique et aux Énergies Alternatives / CEA, France; the Bundesministerium für Bildung und Forschung, Deutsche Forschungsgemeinschaft, and Helmholtz-Gemeinschaft Deutscher Forschungszentren, Germany; the General Secretariat for Research and Technology, Greece; the National Scientific Research Foundation, and National Office for Research and Technology, Hungary; the Department of Atomic Energy and the Department of Science and Technology, India; the Institute for Studies in Theoretical Physics and Mathematics, Iran; the Science Foundation, Ireland; the Istituto Nazionale di Fisica Nucleare, Italy; the Korean Ministry of Education, Science and Technology and the World Class University program of NRF, Korea; the Lithuanian Academy of Sciences; the Mexican Funding Agencies (CINVESTAV, CONACYT, SEP, and UASLP-FAI); the Ministry of Science and Innovation, New Zealand; the Pakistan Atomic Energy Commission; the State Commission for Scientific Research, Poland; the Fundação para a Ciência e a Tecnologia, Portugal; JINR (Armenia, Belarus, Georgia, Ukraine, Uzbekistan); the Ministry of Science and Technologies of the Russian Federation, and Russian Ministry of Atomic Energy; the Ministry of Science and Technological Development of Serbia; the Ministerio de Ciencia e Innovación, and Programa Consolider-Ingenio 2010, Spain; the Swiss Funding Agencies (ETH Board, ETH Zurich, PSI, SNF, UniZH, Canton Zurich, and SER); the National Science Council, Taipei; the Scientific and Technical Research Council of Turkey, and Turkish Atomic Energy Authority; the Science and Technology Facilities Council, U.K.; the U.S. Department of Energy, and the U.S. National Science Foundation.

2012 JINST 7 P10002

Individuals have received support from the Marie-Curie programme and the European Research Council (European Union); the Leventis Foundation; the A. P. Sloan Foundation; the Alexander von Humboldt Foundation; the Associazione per lo Sviluppo Scientifico e Tecnologico del Piemonte (Italy); the Belgian Federal Science Policy Office; the Fonds pour la Formation à la Recherche dans l'Industrie et dans l'Agriculture (FRIA-Belgium); the Agentschap voor Innovatie door Wetenschap en Technologie (IWT-Belgium); and the Council of Science and Industrial Research, India.

References

[1] CMS collaboration, S. Chatrchyan et al., *Commissioning of the CMS experiment and the cosmic run at four Tesla*, 2010 *JINST* **5** T03001 [arXiv:0911.4845].

[2] CMS collaboration, S. Chatrchyan et al., *Performance of CMS muon reconstruction in cosmic-ray events*, 2010 *JINST* **5** T03022 [arXiv:0911.4994].

[3] CMS collaboration, *Performance of muon identification in pp collisions at* $\sqrt{s} = 7$ *TeV*, CMS-PAS-MUO-10-002, CERN, Geneva Switzerland (2010).

[4] CMS collaboration, S. Chatrchyan et al., *The CMS experiment at the CERN LHC*, 2008 *JINST* **3** S08004.

[5] CMS collaboration, *CMS TriDAS project: technical design report; 1, the trigger systems*, CERN-LHCC-2000-038, CERN, Geneva Switzerland [CMS-TDR-006-1].

[6] CMS collaboration, *CMS trigger and data-acquisition project: technical design report*, CERN-LHCC-2002-026, CERN, Geneva Switzerland (2002) [CMS-TDR-006-ADD-2].

[7] J. Pumplin et al., *New generation of parton distributions with uncertainties from global QCD analysis*, *JHEP* **07** (2002) 012.

[8] T. Sjöstrand, S. Mrenna and P. Skands, *PYTHIA* 6.4 *physics and manual*, *JHEP* **05** (2006) 026.

[9] CMS collaboration, S. Chatrchyan et al., *Measurement of the underlying event activity at the LHC with* $\sqrt{s} = 7$ *TeV and comparison with* $\sqrt{s} = 0.9$ *TeV*, *JHEP* **09** (2011) 109 [arXiv:1107.0330].

[10] D. Lange, *The EvtGen particle decay simulation package*, *Nucl. Instrum. Meth.* **A 462** (2001) 152.

[11] S. Frixione, P. Nason and C. Oleari, *Matching NLO QCD computations with parton shower simulations: the POWHEG method*, *JHEP* **11** (2007) 070 [arXiv:0709.2092].

[12] J. Alwall et al., *MadGraph/MadEvent v4: the new web generation*, *JHEP* **09** (2007) 028.

[13] GEANT4 collaboration, S. Agostinelli et al., *GEANT4: a simulation toolkit*, *Nucl. Instrum. Meth.* **A 506** (2003) 250.

[14] J. Allison et al., *GEANT4 developments and applications*, *IEEE Trans. Nucl. Sci.* **53** (2006) 270.

[15] CMS collaboration, *CMS physics technical design report volume I: detector performance and software*, CERN-LHCC-2006-001, CERN, Geneva Switzerland (2006) [CMS-TDR-008-1].

[16] R. Fruhwirth, *Application of Kalman filtering to track and vertex fitting*, *Nucl. Instrum. Meth.* **A 262** (1987) 444.

[17] CMS collaboration, *Measurement of tracking efficiency*, CMS-PAS-TRK-10-002, CERN, Geneva Switzerland (2010).

2012 JINST 7 P10002

[18] CMS collaboration, V. Khachatryan et al., *Prompt and non-prompt J/ψ production in pp collisions at* $\sqrt{s} = 7$ *TeV*, *Eur. Phys. J.* **C 71** (2011) 1575 [arXiv:1011.4193].

[19] CMS collaboration, V. Khachatryan et al., *Measurements of inclusive W and Z cross sections in pp collisions at* $\sqrt{s} = 7$ *TeV*, *JHEP* **01** (2011) 080 [arXiv:1012.2466].

[20] CMS collaboration, S. Chatrchyan et al., *Measurement of the inclusive W and Z production cross sections in pp collisions at* $\sqrt{s} = 7$ *TeV*, *JHEP* **10** (2011) 132 [arXiv:1107.4789].

[21] CMS collaboration, *Particle-flow event reconstruction in CMS and performance for jets, taus and* $\not{E}_T$, CMS-PAS-PFT-09-001, CERN, Geneva Switzerland (2009).

[22] CMS collaboration, *Commissioning of the particle-flow event reconstruction with leptons from J/ψ and W decays at* 7 *TeV*, CMS-PAS-PFT-10-003, CERN, Geneva Switzerland (2010).

[23] H. Burkhardt et al. eds., *LHC lumi days: LHC workshop on LHC luminosity calibration*, CERN-PROCEEDINGS-2011-001, CERN, Geneva Switzerland (2011).

[24] S. Frixione and B.R. Webber, *Matching NLO QCD computations and parton shower simulations*, *JHEP* **06** (2002) 029 [hep-ph/0204244].

[25] S. Frixione, P. Nason and B.R. Webber, *Matching NLO QCD and parton showers in heavy flavor production*, *JHEP* **08** (2003) 007 [hep-ph/0305252].

[26] CMS collaboration, V. Khachatryan et al., *Measurement of the* B^+ *production cross section in pp collisions at* $\sqrt{s} = 7$ *TeV*, *Phys. Rev. Lett.* **106** (2011) 112001 [arXiv:1101.0131].

[27] CMS collaboration, S. Chatrchyan et al., *Measurement of the* B^0 *production cross section in pp collisions at* $\sqrt{s} = 7$ *TeV*, *Phys. Rev. Lett.* **106** (2011) 252001 [arXiv:1104.2892].

[28] M.J. Oreglia, *A study of the reactions* $\psi' \to \gamma\gamma\psi$, Ph.D. thesis, appendix D, SLAC-R-236, Stanford University, Stanford U.S.A. (1980).

[29] M. Pivk and F.R. Le Diberder, *SPlot: a statistical tool to unfold data distributions*, *Nucl. Instrum. Meth.* **A 555** (2005) 356 [physics/0402083].

[30] N. Arkani-Hamed, D.P. Finkbeiner, T.R. Slatyer and N. Weiner, *A theory of dark matter*, *Phys. Rev.* **D 79** (2009) 015014 [arXiv:0810.0713].

[31] D.P. Finkbeiner and N. Weiner, *Exciting dark matter and the INTEGRAL/SPI* 511 *keV signal*, *Phys. Rev.* **D 76** (2007) 083519 [astro-ph/0702587].

[32] D. Tucker-Smith and N. Weiner, *Inelastic dark matter*, *Phys. Rev.* **D 64** (2001) 043502 [hep-ph/0101138].

[33] PAMELA collaboration, O. Adriani et al., *An anomalous positron abundance in cosmic rays with energies* 1.5–100 *GeV*, *Nature* **458** (2009) 607 [arXiv:0810.4995].

[34] FERMI-LAT collaboration, A.A. Abdo et al., *Measurement of the cosmic ray* $e^+ + e^-$ *spectrum from* 20 *GeV to* 1 *TeV with the Fermi Large Area Telescope*, *Phys. Rev. Lett.* **102** (2009) 181101 [arXiv:0905.0025].

[35] J. Chang et al., *An excess of cosmic ray electrons at energies of* 300–800 *GeV*, *Nature* **456** (2008) 362.

[36] CMS collaboration, *Tracking and vertexing results from first collisions*, *Eur. Phys. J.* **C 70** (2010) 165.

[37] CMS collaboration, *Measurement of momentum scale and resolution of the CMS detector using low-mass resonances and cosmic ray muons*, CMS-PAS-TRK-10-004, CERN, Geneva Switzerland (2010).

2012 JINST 7 P10002

[38] S. Dittmaier and M. Huber, *Radiative corrections to the neutral-current Drell-Yan process in the Standard Model and its minimal supersymmetric extension*, *JHEP* **01** (2010) 060 [arXiv:0911.2329].

[39] CMS collaboration, *Measurement of the charge asymmetry of atmospheric muons with the CMS detector*, CMS-PAS-MUO-10-001, CERN, Geneva Switzerland (2010).

[40] CMS collaboration, S. Chatrchyan et al., *Search for a W' boson decaying to a muon and a neutrino in pp collisions at $\sqrt{s} = 7$ TeV*, *Phys. Lett.* **B 701** (2011) 160 [arXiv:1103.0030].

[41] CMS collaboration, S. Chatrchyan et al., *Search for resonances in the dilepton mass distribution in pp collisions at $\sqrt{s} = 7$ TeV*, *JHEP* **05** (2011) 093 [arXiv:1103.0981].

[42] CMS collaboration, S. Chatrchyan et al., *Missing transverse energy performance of the CMS detector*, 2011 *JINST* **6** P09001 [arXiv:1106.5048].

[43] CMS collaboration, V. Khachatryan et al., *Search for stopped gluinos in pp collisions at $\sqrt{s} = 7$ TeV*, *Phys. Rev. Lett.* **106** (2011) 011801 [arXiv:1011.5861].

[44] CMS collaboration, S. Chatrchyan et al., *Search for new physics with jets and missing transverse momentum in pp collisions at $\sqrt{s} = 7$ TeV*, *JHEP* **08** (2011) 155 [arXiv:1106.4503].

[45] CMS collaboration, S. Chatrchyan et al., *Measurement of the inclusive Z cross section via decays to tau pairs in pp collisions at $\sqrt{s} = 7$ TeV*, *JHEP* **08** (2011) 117 [arXiv:1104.1617].

[46] CMS collaboration, V. Khachatryan et al., *CMS tracking performance results from early LHC operation*, *Eur. Phys. J.* **C 70** (2010) 1165 [arXiv:1007.1988].

[47] S. Abdullin et al., *Sensitivity of the muon isolation cut efficiency to the underlying event uncertainties*, CMS-NOTE-2006-033, CERN, Geneva Switzerland (2006).

[48] M. Cacciari and G.P. Salam, *Pileup subtraction using jet areas*, *Phys. Lett.* **B 659** (2008) 119 [arXiv:0707.1378].

[49] CMS collaboration, *The performance of the CMS muon detector using pp collisions at $\sqrt{s} = 7$ TeV at the LHC*, CMS-PAS-MUO-11-001, to be published, CERN, Geneva Switzerland (2012).

[50] CMS collaboration, *Performance of the b-jet identification in CMS*, CMS-PAS-BTV-11-001, CERN, Geneva Switzerland (2011).

2012 JINST 7 P10002

The CMS collaboration

Yerevan Physics Institute, Yerevan, Armenia

S. Chatrchyan, V. Khachatryan, A.M. Sirunyan, A. Tumasyan

Institut für Hochenergiephysik der OeAW, Wien, Austria

W. Adam, T. Bergauer, M. Dragicevic, J. Erö, C. Fabjan, M. Friedl, R. Frühwirth, V.M. Ghete, J. Hammer[1], M. Hoch, N. Hörmann, J. Hrubec, M. Jeitler, W. Kiesenhofer, M. Krammer, D. Liko, I. Mikulec, M. Pernicka[†], B. Rahbaran, C. Rohringer, H. Rohringer, R. Schöfbeck, J. Strauss, A. Taurok, F. Teischinger, P. Wagner, W. Waltenberger, G. Walzel, E. Widl, C.-E. Wulz

National Centre for Particle and High Energy Physics, Minsk, Belarus

V. Mossolov, N. Shumeiko, J. Suarez Gonzalez

Universiteit Antwerpen, Antwerpen, Belgium

S. Bansal, L. Benucci, T. Cornelis, E.A. De Wolf, X. Janssen, S. Luyckx, T. Maes, L. Mucibello, S. Ochesanu, B. Roland, R. Rougny, M. Selvaggi, H. Van Haevermaet, P. Van Mechelen, N. Van Remortel, A. Van Spilbeeck

Vrije Universiteit Brussel, Brussel, Belgium

F. Blekman, S. Blyweert, J. D'Hondt, R. Gonzalez Suarez, A. Kalogeropoulos, M. Maes, A. Olbrechts, W. Van Doninck, P. Van Mulders, G.P. Van Onsem, I. Villella

Université Libre de Bruxelles, Bruxelles, Belgium

O. Charaf, B. Clerbaux, G. De Lentdecker, V. Dero, A.P.R. Gay, G.H. Hammad, T. Hreus, A. Léonard, P.E. Marage, L. Thomas, C. Vander Velde, P. Vanlaer, J. Wickens

Ghent University, Ghent, Belgium

V. Adler, K. Beernaert, A. Cimmino, S. Costantini, G. Garcia, M. Grunewald, B. Klein, J. Lellouch, A. Marinov, J. Mccartin, A.A. Ocampo Rios, D. Ryckbosch, N. Strobbe, F. Thyssen, M. Tytgat, L. Vanelderen, P. Verwilligen, S. Walsh, E. Yazgan, N. Zaganidis

Université Catholique de Louvain, Louvain-la-Neuve, Belgium

S. Basegmez, G. Bruno, L. Ceard, J. De Favereau De Jeneret, C. Delaere, T. du Pree, D. Favart, L. Forthomme, A. Giammanco[2], G. Grégoire, J. Hollar, V. Lemaitre, J. Liao, O. Militaru, C. Nuttens, D. Pagano, A. Pin, K. Piotrzkowski, N. Schul

Université de Mons, Mons, Belgium

N. Beliy, T. Caebergs, E. Daubie

Centro Brasileiro de Pesquisas Fisicas, Rio de Janeiro, Brazil

G.A. Alves, M. Correa Martins Junior, D. De Jesus Damiao, T. Martins, M.E. Pol, M.H.G. Souza

Universidade do Estado do Rio de Janeiro, Rio de Janeiro, Brazil

W.L. Aldá Júnior, W. Carvalho, A. Custódio, E.M. Da Costa, C. De Oliveira Martins, S. Fonseca De Souza, D. Matos Figueiredo, L. Mundim, H. Nogima, V. Oguri, W.L. Prado Da Silva, A. Santoro, S.M. Silva Do Amaral, L. Soares Jorge, A. Sznajder

2012 JINST 7 P10002

Instituto de Fisica Teorica, Universidade Estadual Paulista, Sao Paulo, Brazil
T.S. Anjos[3], C.A. Bernardes[3], F.A. Dias[4], T.R. Fernandez Perez Tomei, E. M. Gregores[3], C. Lagana, F. Marinho, P.G. Mercadante[3], S.F. Novaes, Sandra S. Padula

Institute for Nuclear Research and Nuclear Energy, Sofia, Bulgaria
V. Genchev[1], P. Iaydjiev[1], S. Piperov, M. Rodozov, S. Stoykova, G. Sultanov, V. Tcholakov, R. Trayanov, M. Vutova

University of Sofia, Sofia, Bulgaria
A. Dimitrov, R. Hadjiiska, A. Karadzhinova, V. Kozhuharov, L. Litov, B. Pavlov, P. Petkov

Institute of High Energy Physics, Beijing, China
J.G. Bian, G.M. Chen, H.S. Chen, C.H. Jiang, D. Liang, S. Liang, X. Meng, J. Tao, J. Wang, J. Wang, X. Wang, Z. Wang, H. Xiao, M. Xu, J. Zang, Z. Zhang

State Key Lab. of Nucl. Phys. and Tech., Peking University, Beijing, China
C. Asawatangtrakuldee, Y. Ban, S. Guo, Y. Guo, W. Li, S. Liu, Y. Mao, S.J. Qian, H. Teng, S. Wang, B. Zhu, W. Zou

Universidad de Los Andes, Bogota, Colombia
A. Cabrera, B. Gomez Moreno, A.F. Osorio Oliveros, J.C. Sanabria

Technical University of Split, Split, Croatia
N. Godinovic, D. Lelas, R. Plestina[5], D. Polic, I. Puljak[1]

University of Split, Split, Croatia
Z. Antunovic, M. Dzelalija, M. Kovac

Institute Rudjer Boskovic, Zagreb, Croatia
V. Brigljevic, S. Duric, K. Kadija, J. Luetic, S. Morovic

University of Cyprus, Nicosia, Cyprus
A. Attikis, M. Galanti, J. Mousa, C. Nicolaou, F. Ptochos, P.A. Razis

Charles University, Prague, Czech Republic
M. Finger, M. Finger Jr.

Academy of Scientific Research and Technology of the Arab Republic of Egypt, Egyptian Network of High Energy Physics, Cairo, Egypt
Y. Assran[6], A. Ellithi Kamel[7], S. Khalil[8], M.A. Mahmoud[9], A. Radi[8,10]

National Institute of Chemical Physics and Biophysics, Tallinn, Estonia
A. Hektor, M. Kadastik, M. Müntel, M. Raidal, L. Rebane, A. Tiko

Department of Physics, University of Helsinki, Helsinki, Finland
V. Azzolini, P. Eerola, G. Fedi, M. Voutilainen

Helsinki Institute of Physics, Helsinki, Finland
S. Czellar, J. Härkönen, A. Heikkinen, V. Karimäki, R. Kinnunen, M.J. Kortelainen, T. Lampén, K. Lassila-Perini, S. Lehti, T. Lindén, P. Luukka, T. Mäenpää, T. Peltola, E. Tuominen, J. Tuominiemi, E. Tuovinen, D. Ungaro, L. Wendland

2012 JINST 7 P10002

Lappeenranta University of Technology, Lappeenranta, Finland

K. Banzuzi, A. Korpela, T. Tuuva

Laboratoire d'Annecy-le-Vieux de Physique des Particules, IN2P3-CNRS, Annecy-le-Vieux, France

D. Sillou

DSM/IRFU, CEA/Saclay, Gif-sur-Yvette, France

M. Besancon, S. Choudhury, M. Dejardin, D. Denegri, B. Fabbro, J.L. Faure, F. Ferri, S. Ganjour, A. Givernaud, P. Gras, G. Hamel de Monchenault, P. Jarry, E. Locci, J. Malcles, L. Millischer, J. Rander, A. Rosowsky, I. Shreyber, M. Titov

Laboratoire Leprince-Ringuet, Ecole Polytechnique, IN2P3-CNRS, Palaiseau, France

S. Baffioni, F. Beaudette, L. Benhabib, L. Bianchini, M. Bluj[11], C. Broutin, P. Busson, C. Charlot, N. Daci, T. Dahms, L. Dobrzynski, S. Elgammal, R. Granier de Cassagnac, M. Haguenauer, P. Miné, C. Mironov, C. Ochando, P. Paganini, D. Sabes, R. Salerno, Y. Sirois, C. Thiebaux, C. Veelken, A. Zabi

Institut Pluridisciplinaire Hubert Curien, Université de Strasbourg, Université de Haute Alsace Mulhouse, CNRS/IN2P3, Strasbourg, France

J.-L. Agram[12], J. Andrea, D. Bloch, D. Bodin, J.-M. Brom, M. Cardaci, E.C. Chabert, C. Collard, E. Conte[12], F. Drouhin[12], C. Ferro, J.-C. Fontaine[12], D. Gelé, U. Goerlach, P. Juillot, M. Karim[12], A.-C. Le Bihan, P. Van Hove

Centre de Calcul de l'Institut National de Physique Nucleaire et de Physique des Particules (IN2P3), Villeurbanne, France

F. Fassi, D. Mercier

Université de Lyon, Université Claude Bernard Lyon 1, CNRS-IN2P3, Institut de Physique Nucléaire de Lyon, Villeurbanne, France

C. Baty, S. Beauceron, N. Beaupere, M. Bedjidian, O. Bondu, G. Boudoul, D. Boumediene, H. Brun, J. Chasserat, R. Chierici[1], D. Contardo, P. Depasse, H. El Mamouni, A. Falkiewicz, J. Fay, S. Gascon, M. Gouzevitch, B. Ille, T. Kurca, T. Le Grand, M. Lethuillier, L. Mirabito, S. Perries, V. Sordini, S. Tosi, Y. Tschudi, P. Verdier, S. Viret

Institute of High Energy Physics and Informatization, Tbilisi State University, Tbilisi, Georgia

D. Lomidze

RWTH Aachen University, I. Physikalisches Institut, Aachen, Germany

G. Anagnostou, S. Beranek, M. Edelhoff, L. Feld, N. Heracleous, O. Hindrichs, R. Jussen, K. Klein, J. Merz, A. Ostapchuk, A. Perieanu, F. Raupach, J. Sammet, S. Schael, D. Sprenger, H. Weber, B. Wittmer, V. Zhukov[13]

RWTH Aachen University, III. Physikalisches Institut A, Aachen, Germany

M. Ata, J. Caudron, E. Dietz-Laursonn, M. Erdmann, A. Güth, T. Hebbeker, C. Heidemann, K. Hoepfner, T. Klimkovich, D. Klingebiel, P. Kreuzer, D. Lanske[†], J. Lingemann, C. Magass,

2012 JINST 7 P10002

M. Merschmeyer, A. Meyer, M. Olschewski, P. Papacz, H. Pieta, H. Reithler, S.A. Schmitz, L. Sonnenschein, J. Steggemann, D. Teyssier, M. Weber

RWTH Aachen University, III. Physikalisches Institut B, Aachen, Germany

M. Bontenackels, V. Cherepanov, M. Davids, G. Flügge, H. Geenen, M. Geisler, W. Haj Ahmad, F. Hoehle, B. Kargoll, T. Kress, Y. Kuessel, A. Linn, A. Nowack, L. Perchalla, O. Pooth, J. Rennefeld, P. Sauerland, A. Stahl, M.H. Zoeller

Deutsches Elektronen-Synchrotron, Hamburg, Germany

M. Aldaya Martin, W. Behrenhoff, U. Behrens, M. Bergholz[14], A. Bethani, K. Borras, A. Burgmeier, A. Cakir, L. Calligaris, A. Campbell, E. Castro, D. Dammann, G. Eckerlin, D. Eckstein, A. Flossdorf, G. Flucke, A. Geiser, J. Hauk, H. Jung[1], M. Kasemann, P. Katsas, C. Kleinwort, H. Kluge, A. Knutsson, M. Krämer, D. Krücker, E. Kuznetsova, W. Lange, W. Lohmann[14], B. Lutz, R. Mankel, I. Marfin, M. Marienfeld, I.-A. Melzer-Pellmann, A.B. Meyer, J. Mnich, A. Mussgiller, S. Naumann-Emme, J. Olzem, A. Petrukhin, D. Pitzl, A. Raspereza, P.M. Ribeiro Cipriano, M. Rosin, J. Salfeld-Nebgen, R. Schmidt[14], T. Schoerner-Sadenius, N. Sen, A. Spiridonov, M. Stein, J. Tomaszewska, R. Walsh, C. Wissing

University of Hamburg, Hamburg, Germany

C. Autermann, V. Blobel, S. Bobrovskyi, J. Draeger, H. Enderle, J. Erfle, U. Gebbert, M. Görner, T. Hermanns, R.S. Höing, K. Kaschube, G. Kaussen, H. Kirschenmann, R. Klanner, J. Lange, B. Mura, F. Nowak, N. Pietsch, C. Sander, H. Schettler, P. Schleper, E. Schlieckau, A. Schmidt, M. Schröder, T. Schum, H. Stadie, G. Steinbrück, J. Thomsen

Institut für Experimentelle Kernphysik, Karlsruhe, Germany

C. Barth, J. Berger, T. Chwalek, W. De Boer, A. Dierlamm, G. Dirkes, M. Feindt, J. Gruschke, M. Guthoff[1], C. Hackstein, F. Hartmann, M. Heinrich, H. Held, K.H. Hoffmann, S. Honc, I. Katkov[13], J.R. Komaragiri, T. Kuhr, D. Martschei, S. Mueller, Th. Müller, M. Niegel, A. Nürnberg, O. Oberst, A. Oehler, J. Ott, T. Peiffer, G. Quast, K. Rabbertz, F. Ratnikov, N. Ratnikova, M. Renz, S. Röcker, C. Saout, A. Scheurer, P. Schieferdecker, F.-P. Schilling, M. Schmanau, G. Schott, H.J. Simonis, F.M. Stober, D. Troendle, J. Wagner-Kuhr, T. Weiler, M. Zeise, E.B. Ziebarth

Institute of Nuclear Physics "Demokritos", Aghia Paraskevi, Greece

G. Daskalakis, T. Geralis, S. Kesisoglou, A. Kyriakis, D. Loukas, I. Manolakos, A. Markou, C. Markou, C. Mavrommatis, E. Ntomari

University of Athens, Athens, Greece

L. Gouskos, T.J. Mertzimekis, A. Panagiotou, N. Saoulidou, E. Stiliaris

University of Ioánnina, Ioánnina, Greece

I. Evangelou, C. Foudas[1], P. Kokkas, N. Manthos, I. Papadopoulos, V. Patras, F.A. Triantis

KFKI Research Institute for Particle and Nuclear Physics, Budapest, Hungary

A. Aranyi, G. Bencze, L. Boldizsar, C. Hajdu[1], P. Hidas, D. Horvath[15], A. Kapusi, K. Krajczar[16], F. Sikler[1], V. Veszpremi, G. Vesztergombi[16]

2012 JINST 7 P10002

Institute of Nuclear Research ATOMKI, Debrecen, Hungary
N. Beni, J. Molnar, J. Palinkas, Z. Szillasi

University of Debrecen, Debrecen, Hungary
J. Karancsi, P. Raics, Z.L. Trocsanyi, B. Ujvari

Panjab University, Chandigarh, India
S.B. Beri, V. Bhatnagar, N. Dhingra, R. Gupta, M. Jindal, M. Kaur, J.M. Kohli, M.Z. Mehta, N. Nishu, L.K. Saini, A. Sharma, A.P. Singh, J. Singh, S.P. Singh

University of Delhi, Delhi, India
Ashok Kumar, Arun Kumar, S. Ahuja, B.C. Choudhary, S. Malhotra, M. Naimuddin, K. Ranjan, V. Sharma, R.K. Shivpuri

Saha Institute of Nuclear Physics, Kolkata, India
S. Banerjee, S. Bhattacharya, S. Dutta, B. Gomber, Sa. Jain, Sh. Jain, R. Khurana, S. Sarkar

Bhabha Atomic Research Centre, Mumbai, India
R.K. Choudhury, D. Dutta, S. Kailas, V. Kumar, A.K. Mohanty[1], L.M. Pant, P. Shukla

Tata Institute of Fundamental Research - EHEP, Mumbai, India
T. Aziz, S. Ganguly, M. Guchait[17], A. Gurtu[18], M. Maity[19], G. Majumder, K. Mazumdar, G.B. Mohanty, B. Parida, A. Saha, K. Sudhakar, N. Wickramage

Tata Institute of Fundamental Research - HECR, Mumbai, India
S. Banerjee, S. Dugad, N.K. Mondal

Institute for Research in Fundamental Sciences (IPM), Tehran, Iran
H. Arfaei, H. Bakhshiansohi[20], S.M. Etesami[21], A. Fahim[20], M. Hashemi, H. Hesari, A. Jafari[20], M. Khakzad, A. Mohammadi[22], M. Mohammadi Najafabadi, S. Paktinat Mehdiabadi, B. Safarzadeh[23], M. Zeinali[21]

INFN Sezione di Bari [a], Università di Bari [b], Politecnico di Bari [c], Bari, Italy
M. Abbrescia[a,b], L. Barbone[a,b], C. Calabria[a,b], S.S. Chhibra[a,b], A. Colaleo[a], D. Creanza[a,c], N. De Filippis[a,c,1], M. De Palma[a,b], L. Fiore[a], G. Iaselli[a,c], L. Lusito[a,b], G. Maggi[a,c], M. Maggi[a], N. Manna[a,b], B. Marangelli[a,b], S. My[a,c], S. Nuzzo[a,b], N. Pacifico[a,b], A. Pompili[a,b], G. Pugliese[a,c], F. Romano[a,c], G. Selvaggi[a,b], L. Silvestris[a], G. Singh[a,b], S. Tupputi[a,b], G. Zito[a]

INFN Sezione di Bologna [a], Università di Bologna [b], Bologna, Italy
G. Abbiendi[a], A.C. Benvenuti[a], D. Bonacorsi[a], S. Braibant-Giacomelli[a,b], L. Brigliadori[a], P. Capiluppi[a,b], A. Castro[a,b], F.R. Cavallo[a], M. Cuffiani[a,b], G.M. Dallavalle[a], F. Fabbri[a], A. Fanfani[a,b], D. Fasanella[a,1], P. Giacomelli[a], C. Grandi[a], S. Marcellini[a], G. Masetti[a], M. Meneghelli[a,b], A. Montanari[a], F.L. Navarria[a,b], F. Odorici[a], A. Perrotta[a], F. Primavera[a], A.M. Rossi[a,b], T. Rovelli[a,b], G. Siroli[a,b], R. Travaglini[a,b]

INFN Sezione di Catania [a], Università di Catania [b], Catania, Italy
S. Albergo[a,b], G. Cappello[a,b], M. Chiorboli[a,b], S. Costa[a,b], R. Potenza[a,b], A. Tricomi[a,b], C. Tuve[a,b]

2012 JINST 7 P10002

INFN Sezione di Firenze [a], Università di Firenze [b], Firenze, Italy

G. Barbagli[a], V. Ciulli[a,b], C. Civinini[a], R. D'Alessandro[a,b], E. Focardi[a,b], S. Frosali[a,b], E. Gallo[a], S. Gonzi[a,b], M. Meschini[a], S. Paoletti[a], G. Sguazzoni[a], A. Tropiano[a,1]

INFN Laboratori Nazionali di Frascati, Frascati, Italy

L. Benussi, S. Bianco, S. Colafranceschi[24], F. Fabbri, D. Piccolo

INFN Sezione di Genova, Genova, Italy

P. Fabbricatore, R. Musenich

INFN Sezione di Milano-Bicocca [a], Università di Milano-Bicocca [b], Milano, Italy

A. Benaglia[a,b,1], F. De Guio[a,b], L. Di Matteo[a,b], S. Fiorendi[a,b], S. Gennai[a,1], A. Ghezzi[a,b], S. Malvezzi[a], R.A. Manzoni[a,b], A. Martelli[a,b], A. Massironi[a,b,1], D. Menasce[a], L. Moroni[a], M. Paganoni[a,b], D. Pedrini[a], S. Ragazzi[a,b], N. Redaelli[a], S. Sala[a], T. Tabarelli de Fatis[a,b]

INFN Sezione di Napoli [a], Università di Napoli "Federico II" [b], Napoli, Italy

S. Buontempo[a], C.A. Carrillo Montoya[a,1], N. Cavallo[a,25], A. De Cosa[a,b], O. Dogangun[a,b], F. Fabozzi[a,25], A.O.M. Iorio[a,1], L. Lista[a], M. Merola[a,b], P. Paolucci[a]

INFN Sezione di Padova [a], Università di Padova [b], Università di Trento (Trento) [c], Padova, Italy

P. Azzi[a], N. Bacchetta[a,1], P. Bellan[a,b], M. Bellato[a], D. Bisello[a,b], A. Branca[a], R. Carlin[a,b], P. Checchia[a], T. Dorigo[a], F. Gasparini[a,b], A. Gozzelino[a,26], K. Kanishchev[a,c], S. Lacaprara[a], I. Lazzizzera[a,c], M. Margoni[a,b], G. Maron[a,26], A.T. Meneguzzo[a,b], M. Nespolo[a,1], M. Passaseo[a], L. Perrozzi[a], N. Pozzobon[a,b], P. Ronchese[a,b], F. Simonetto[a,b], E. Torassa[a], M. Tosi[a,b,1], S. Vanini[a,b], S. Ventura[a], P. Zotto[a,b], G. Zumerle[a,b]

INFN Sezione di Pavia [a], Università di Pavia [b], Pavia, Italy

P. Baesso[a,b], U. Berzano[a], M. Gabusi[a,b], S.P. Ratti[a,b], C. Riccardi[a,b], P. Torre[a,b], P. Vitulo[a,b], C. Viviani[a,b]

INFN Sezione di Perugia [a], Università di Perugia [b], Perugia, Italy

M. Biasini[a,b], G.M. Bilei[a], B. Caponeri[a,b], L. Fanò[a,b], P. Lariccia[a,b], A. Lucaroni[a,b,1], G. Mantovani[a,b], M. Menichelli[a], A. Nappi[a,b], F. Romeo[a,b], A. Santocchia[a,b], S. Taroni[a,b,1], M. Valdata[a,b]

INFN Sezione di Pisa [a], Università di Pisa [b], Scuola Normale Superiore di Pisa [c], Pisa, Italy

P. Azzurri[a,c], G. Bagliesi[a], T. Boccali[a], G. Broccolo[a,c], R. Castaldi[a], R.T. D'Agnolo[a,c], R. Dell'Orso[a], F. Fiori[a,b], L. Foà[a,c], A. Giassi[a], A. Kraan[a], F. Ligabue[a,c], T. Lomtadze[a], L. Martini[a,27], A. Messineo[a,b], F. Palla[a], F. Palmonari[a], A. Rizzi[a,b], A.T. Serban[a], P. Spagnolo[a], R. Tenchini[a], G. Tonelli[a,b,1], A. Venturi[a,1], P.G. Verdini[a]

INFN Sezione di Roma [a], Università di Roma "La Sapienza" [b], Roma, Italy

L. Barone[a,b], F. Cavallari[a], D. Del Re[a,b,1], M. Diemoz[a], C. Fanelli[a,b], D. Franci[a,b], M. Grassi[a,1], E. Longo[a,b], P. Meridiani[a], F. Micheli[a,b], S. Nourbakhsh[a], G. Organtini[a,b], F. Pandolfi[a,b], R. Paramatti[a], S. Rahatlou[a,b], M. Sigamani[a], L. Soffi[a,b]

2012 JINST 7 P10002

INFN Sezione di Torino [a], Università di Torino [b], Università del Piemonte Orientale (Novara) [c], Torino, Italy

N. Amapane[a,b], R. Arcidiacono[a,c], S. Argiro[a,b], M. Arneodo[a,c], C. Biino[a], C. Botta[a,b], N. Cartiglia[a], R. Castello[a,b], M. Costa[a,b], N. Demaria[a], A. Graziano[a,b], C. Mariotti[a,1], S. Maselli[a], E. Migliore[a,b], V. Monaco[a,b], M. Musich[a], M.M. Obertino[a,c], N. Pastrone[a], M. Pelliccioni[a], A. Potenza[a,b], A. Romero[a,b], M. Ruspa[a,c], R. Sacchi[a,b], V. Sola[a,b], A. Solano[a,b], A. Staiano[a], A. Vilela Pereira[a]

INFN Sezione di Trieste [a], Università di Trieste [b], Trieste, Italy

S. Belforte[a], F. Cossutti[a], G. Della Ricca[a,b], B. Gobbo[a], M. Marone[a,b], D. Montanino[a,b,1], A. Penzo[a]

Kangwon National University, Chunchon, Korea

S.G. Heo, S.K. Nam

Kyungpook National University, Daegu, Korea

S. Chang, J. Chung, D.H. Kim, G.N. Kim, J.E. Kim, D.J. Kong, H. Park, S.R. Ro, D.C. Son

Chonnam National University, Institute for Universe and Elementary Particles, Kwangju, Korea

J.Y. Kim, Zero J. Kim, S. Song

Konkuk University, Seoul, Korea

H.Y. Jo

Korea University, Seoul, Korea

S. Choi, D. Gyun, B. Hong, M. Jo, H. Kim, T.J. Kim, K.S. Lee, D.H. Moon, S.K. Park, E. Seo, K.S. Sim

University of Seoul, Seoul, Korea

M. Choi, S. Kang, H. Kim, J.H. Kim, C. Park, I.C. Park, S. Park, G. Ryu

Sungkyunkwan University, Suwon, Korea

Y. Cho, Y. Choi, Y.K. Choi, J. Goh, M.S. Kim, B. Lee, J. Lee, S. Lee, H. Seo, I. Yu

Vilnius University, Vilnius, Lithuania

M.J. Bilinskas, I. Grigelionis, M. Janulis

Centro de Investigacion y de Estudios Avanzados del IPN, Mexico City, Mexico

H. Castilla-Valdez, E. De La Cruz-Burelo, I. Heredia-de La Cruz, R. Lopez-Fernandez, R. Magaña Villalba, J. Martínez-Ortega, A. Sánchez-Hernández, L.M. Villasenor-Cendejas

Universidad Iberoamericana, Mexico City, Mexico

S. Carrillo Moreno, F. Vazquez Valencia

Benemerita Universidad Autonoma de Puebla, Puebla, Mexico

H.A. Salazar Ibarguen

Universidad Autónoma de San Luis Potosí, San Luis Potosí, Mexico

E. Casimiro Linares, A. Morelos Pineda, M.A. Reyes-Santos

2012 JINST 7 P10002

University of Auckland, Auckland, New Zealand

D. Krofcheck

University of Canterbury, Christchurch, New Zealand

A.J. Bell, P.H. Butler, R. Doesburg, S. Reucroft, H. Silverwood

National Centre for Physics, Quaid-I-Azam University, Islamabad, Pakistan

M. Ahmad, M.I. Asghar, H.R. Hoorani, S. Khalid, W.A. Khan, T. Khurshid, S. Qazi, M.A. Shah, M. Shoaib

Institute of Experimental Physics, Faculty of Physics, University of Warsaw, Warsaw, Poland

G. Brona, M. Cwiok, W. Dominik, K. Doroba, A. Kalinowski, M. Konecki, J. Krolikowski

Soltan Institute for Nuclear Studies, Warsaw, Poland

H. Bialkowska, B. Boimska, T. Frueboes, R. Gokieli, M. Górski, M. Kazana, K. Nawrocki, K. Romanowska-Rybinska, M. Szleper, G. Wrochna, P. Zalewski

Laboratório de Instrumentação e Física Experimental de Partículas, Lisboa, Portugal

N. Almeida, P. Bargassa, A. David, P. Faccioli, P.G. Ferreira Parracho, M. Gallinaro, P. Musella, A. Nayak, J. Pela[1], P.Q. Ribeiro, J. Seixas, J. Varela, P. Vischia

Joint Institute for Nuclear Research, Dubna, Russia

I. Belotelov, A. Golunov, I. Golutvin, N. Gorbounov, I. Gramenitski, A. Kamenev, V. Karjavin, A. Kurenkov, A. Lanev, A. Makankin, P. Moisenz, V. Palichik, V. Perelygin, S. Shmatov, D. Smolin, S. Vasil'ev, A. Zarubin

Petersburg Nuclear Physics Institute, Gatchina (St Petersburg), Russia

S. Evstyukhin, V. Golovtsov, Y. Ivanov, V. Kim, P. Levchenko, V. Murzin, V. Oreshkin, I. Smirnov, V. Sulimov, L. Uvarov, S. Vavilov, A. Vorobyev, An. Vorobyev

Institute for Nuclear Research, Moscow, Russia

Yu. Andreev, A. Dermenev, S. Gninenko, N. Golubev, M. Kirsanov, N. Krasnikov, V. Matveev, A. Pashenkov, A. Toropin, S. Troitsky

Institute for Theoretical and Experimental Physics, Moscow, Russia

V. Epshteyn, M. Erofeeva, V. Gavrilov, M. Kossov[1], A. Krokhotin, N. Lychkovskaya, V. Popov, G. Safronov, S. Semenov, V. Stolin, E. Vlasov, A. Zhokin

Moscow State University, Moscow, Russia

A. Belyaev, E. Boos, M. Dubinin[4], L. Dudko, A. Ershov, A. Gribushin, V. Klyukhin, O. Kodolova, A. Markina, S. Obraztsov, M. Perfilov, S. Petrushanko, L. Sarycheva[†], V. Savrin, A. Snigirev

P.N. Lebedev Physical Institute, Moscow, Russia

V. Andreev, M. Azarkin, I. Dremin, M. Kirakosyan, A. Leonidov, G. Mesyats, S.V. Rusakov, A. Vinogradov

2012 JINST 7 P10002

State Research Center of Russian Federation, Institute for High Energy Physics, Protvino, Russia

I. Azhgirey, I. Bayshev, S. Bitioukov, V. Grishin[1], V. Kachanov, D. Konstantinov, A. Korablev, V. Krychkine, V. Petrov, R. Ryutin, A. Sobol, L. Tourtchanovitch, S. Troshin, N. Tyurin, A. Uzunian, A. Volkov

University of Belgrade, Faculty of Physics and Vinca Institute of Nuclear Sciences, Belgrade, Serbia

P. Adzic[28], M. Djordjevic, M. Ekmedzic, D. Krpic[28], J. Milosevic

Centro de Investigaciones Energéticas Medioambientales y Tecnológicas (CIEMAT), Madrid, Spain

M. Aguilar-Benitez, J. Alcaraz Maestre, P. Arce, C. Battilana, E. Calvo, M. Cerrada, M. Chamizo Llatas, N. Colino, B. De La Cruz, A. Delgado Peris, C. Diez Pardos, D. Domínguez Vázquez, C. Fernandez Bedoya, J.P. Fernández Ramos, A. Ferrando, J. Flix, M.C. Fouz, P. Garcia-Abia, O. Gonzalez Lopez, S. Goy Lopez, J.M. Hernandez, M.I. Josa, G. Merino, J. Puerta Pelayo, I. Redondo, L. Romero, J. Santaolalla, M.S. Soares, C. Willmott

Universidad Autónoma de Madrid, Madrid, Spain

C. Albajar, G. Codispoti, J.F. de Trocóniz

Universidad de Oviedo, Oviedo, Spain

J. Cuevas, J. Fernandez Menendez, S. Folgueras, I. Gonzalez Caballero, L. Lloret Iglesias, J. Piedra Gomez[29], J.M. Vizan Garcia

Instituto de Física de Cantabria (IFCA), CSIC-Universidad de Cantabria, Santander, Spain

J.A. Brochero Cifuentes, I.J. Cabrillo, A. Calderon, S.H. Chuang, J. Duarte Campderros, M. Felcini[30], M. Fernandez, G. Gomez, J. Gonzalez Sanchez, C. Jorda, P. Lobelle Pardo, A. Lopez Virto, J. Marco, R. Marco, C. Martinez Rivero, F. Matorras, F.J. Munoz Sanchez, T. Rodrigo, A.Y. Rodríguez-Marrero, A. Ruiz-Jimeno, L. Scodellaro, M. Sobron Sanudo, I. Vila, R. Vilar Cortabitarte

CERN, European Organization for Nuclear Research, Geneva, Switzerland

D. Abbaneo, E. Auffray, G. Auzinger, P. Baillon, A.H. Ball, D. Barney, C. Bernet[5], W. Bialas, G. Bianchi, P. Bloch, A. Bocci, H. Breuker, K. Bunkowski, T. Camporesi, G. Cerminara, T. Christiansen, J.A. Coarasa Perez, B. Curé, D. D'Enterria, A. De Roeck, S. Di Guida, M. Dobson, N. Dupont-Sagorin, A. Elliott-Peisert, B. Frisch, W. Funk, A. Gaddi, G. Georgiou, H. Gerwig, M. Giffels, D. Gigi, K. Gill, D. Giordano, M. Giunta, F. Glege, R. Gomez-Reino Garrido, P. Govoni, S. Gowdy, R. Guida, L. Guiducci, M. Hansen, P. Harris, C. Hartl, J. Harvey, B. Hegner, A. Hinzmann, H.F. Hoffmann, V. Innocente, P. Janot, K. Kaadze, E. Karavakis, K. Kousouris, P. Lecoq, P. Lenzi, C. Lourenço, T. Mäki, M. Malberti, L. Malgeri, M. Mannelli, L. Masetti, G. Mavromanolakis, F. Meijers, S. Mersi, E. Meschi, R. Moser, M.U. Mozer, M. Mulders, E. Nesvold, M. Nguyen, T. Orimoto, L. Orsini, E. Palencia Cortezon, E. Perez, A. Petrilli, A. Pfeiffer, M. Pierini, M. Pimiä, D. Piparo, G. Polese, L. Quertenmont, A. Racz, W. Reece, J. Rodrigues Antunes, G. Rolandi[31], T. Rommerskirchen, C. Rovelli[32], M. Rovere, H. Sakulin, F. Santanastasio, C. Schäfer, C. Schwick, I. Segoni, A. Sharma, P. Siegrist, P. Silva, M. Simon,

2012 JINST 7 P10002

P. Sphicas[33], D. Spiga, M. Spiropulu[4], M. Stoye, A. Tsirou, G.I. Veres[16], P. Vichoudis, H.K. Wöhri, S.D. Worm[34], W.D. Zeuner

Paul Scherrer Institut, Villigen, Switzerland

W. Bertl, K. Deiters, W. Erdmann, K. Gabathuler, R. Horisberger, Q. Ingram, H.C. Kaestli, S. König, D. Kotlinski, U. Langenegger, F. Meier, D. Renker, T. Rohe, J. Sibille[35]

Institute for Particle Physics, ETH Zurich, Zurich, Switzerland

L. Bäni, P. Bortignon, M.A. Buchmann, B. Casal, N. Chanon, Z. Chen, A. Deisher, G. Dissertori, M. Dittmar, M. Dünser, J. Eugster, K. Freudenreich, C. Grab, P. Lecomte, W. Lustermann, P. Martinez Ruiz del Arbol, N. Mohr, F. Moortgat, C. Nägeli[36], P. Nef, F. Nessi-Tedaldi, L. Pape, F. Pauss, M. Peruzzi, F.J. Ronga, M. Rossini, L. Sala, A.K. Sanchez, M.-C. Sawley, A. Starodumov[37], B. Stieger, M. Takahashi, L. Tauscher[†], A. Thea, K. Theofilatos, D. Treille, C. Urscheler, R. Wallny, H.A. Weber, L. Wehrli, J. Weng

Universität Zürich, Zurich, Switzerland

E. Aguilo, C. Amsler, V. Chiochia, S. De Visscher, C. Favaro, M. Ivova Rikova, B. Millan Mejias, P. Otiougova, P. Robmann, H. Snoek, M. Verzetti

National Central University, Chung-Li, Taiwan

Y.H. Chang, K.H. Chen, C.M. Kuo, S.W. Li, W. Lin, Z.K. Liu, Y.J. Lu, D. Mekterovic, R. Volpe, S.S. Yu

National Taiwan University (NTU), Taipei, Taiwan

P. Bartalini, P. Chang, Y.H. Chang, Y.W. Chang, Y. Chao, K.F. Chen, C. Dietz, U. Grundler, W.-S. Hou, Y. Hsiung, K.Y. Kao, Y.J. Lei, R.-S. Lu, D. Majumder, E. Petrakou, X. Shi, J.G. Shiu, Y.M. Tzeng, M. Wang

Cukurova University, Adana, Turkey

A. Adiguzel, M.N. Bakirci[38], S. Cerci[39], C. Dozen, I. Dumanoglu, E. Eskut, S. Girgis, G. Gokbulut, I. Hos, E.E. Kangal, G. Karapinar, A. Kayis Topaksu, G. Onengut, K. Ozdemir, S. Ozturk[40], A. Polatoz, K. Sogut[41], D. Sunar Cerci[39], B. Tali[39], H. Topakli[38], D. Uzun, L.N. Vergili, M. Vergili

Middle East Technical University, Physics Department, Ankara, Turkey

I.V. Akin, T. Aliev, B. Bilin, S. Bilmis, M. Deniz, H. Gamsizkan, A.M. Guler, K. Ocalan, A. Ozpineci, M. Serin, R. Sever, U.E. Surat, M. Yalvac, E. Yildirim, M. Zeyrek

Bogazici University, Istanbul, Turkey

M. Deliomeroglu, E. Gülmez, B. Isildak, M. Kaya[42], O. Kaya[42], S. Ozkorucuklu[43], N. Sonmez[44]

National Scientific Center, Kharkov Institute of Physics and Technology, Kharkov, Ukraine

L. Levchuk

University of Bristol, Bristol, United Kingdom

F. Bostock, J.J. Brooke, E. Clement, D. Cussans, H. Flacher, R. Frazier, J. Goldstein, M. Grimes, G.P. Heath, H.F. Heath, L. Kreczko, S. Metson, D.M. Newbold[34], K. Nirunpong, A. Poll, S. Senkin, V.J. Smith, T. Williams

2012 JINST 7 P10002

Rutherford Appleton Laboratory, Didcot, United Kingdom

L. Basso[45], K.W. Bell, A. Belyaev[45], C. Brew, R.M. Brown, D.J.A. Cockerill, J.A. Coughlan, K. Harder, S. Harper, J. Jackson, B.W. Kennedy, E. Olaiya, D. Petyt, B.C. Radburn-Smith, C.H. Shepherd-Themistocleous, I.R. Tomalin, W.J. Womersley

Imperial College, London, United Kingdom

R. Bainbridge, G. Ball, R. Beuselinck, O. Buchmuller, D. Colling, N. Cripps, M. Cutajar, P. Dauncey, G. Davies, M. Della Negra, W. Ferguson, J. Fulcher, D. Futyan, A. Gilbert, A. Guneratne Bryer, G. Hall, Z. Hatherell, J. Hays, G. Iles, M. Jarvis, G. Karapostoli, L. Lyons, A.-M. Magnan, J. Marrouche, B. Mathias, R. Nandi, J. Nash, A. Nikitenko[37], A. Papageorgiou, M. Pesaresi, K. Petridis, M. Pioppi[46], D.M. Raymond, S. Rogerson, N. Rompotis, A. Rose, M.J. Ryan, C. Seez, P. Sharp, A. Sparrow, A. Tapper, S. Tourneur, M. Vazquez Acosta, T. Virdee, S. Wakefield, N. Wardle, D. Wardrope, T. Whyntie

Brunel University, Uxbridge, United Kingdom

M. Barrett, M. Chadwick, J.E. Cole, P.R. Hobson, A. Khan, P. Kyberd, D. Leslie, W. Martin, I.D. Reid, P. Symonds, L. Teodorescu, M. Turner

Baylor University, Waco, U.S.A.

K. Hatakeyama, H. Liu, T. Scarborough

The University of Alabama, Tuscaloosa, U.S.A.

C. Henderson

Boston University, Boston, U.S.A.

A. Avetisyan, T. Bose, E. Carrera Jarrin, C. Fantasia, A. Heister, J. St. John, P. Lawson, D. Lazic, J. Rohlf, D. Sperka, L. Sulak

Brown University, Providence, U.S.A.

S. Bhattacharya, D. Cutts, A. Ferapontov, U. Heintz, S. Jabeen, G. Kukartsev, G. Landsberg, M. Luk, M. Narain, D. Nguyen, M. Segala, T. Sinthuprasith, T. Speer, K.V. Tsang

University of California, Davis, Davis, U.S.A.

R. Breedon, G. Breto, M. Calderon De La Barca Sanchez, M. Caulfield, S. Chauhan, M. Chertok, J. Conway, R. Conway, P.T. Cox, J. Dolen, R. Erbacher, M. Gardner, R. Houtz, W. Ko, A. Kopecky, R. Lander, O. Mall, T. Miceli, R. Nelson, D. Pellett, J. Robles, B. Rutherford, M. Searle, J. Smith, M. Squires, M. Tripathi, R. Vasquez Sierra

University of California, Los Angeles, Los Angeles, U.S.A.

V. Andreev, K. Arisaka, D. Cline, R. Cousins, J. Duris, S. Erhan, P. Everaerts, C. Farrell, J. Hauser, M. Ignatenko, C. Jarvis, C. Plager, G. Rakness, P. Schlein[†], J. Tucker, V. Valuev, M. Weber

University of California, Riverside, Riverside, U.S.A.

J. Babb, R. Clare, J. Ellison, J.W. Gary, F. Giordano, G. Hanson, G.Y. Jeng[47], H. Liu, O.R. Long, A. Luthra, H. Nguyen, S. Paramesvaran, J. Sturdy, S. Sumowidagdo, R. Wilken, S. Wimpenny

University of California, San Diego, La Jolla, U.S.A.

W. Andrews, J.G. Branson, G.B. Cerati, S. Cittolin, D. Evans, F. Golf, A. Holzner, R. Kelley, M. Lebourgeois, J. Letts, I. Macneill, B. Mangano, S. Padhi, C. Palmer, G. Petrucciani, H. Pi,

2012 JINST 7 P10002

M. Pieri, R. Ranieri, M. Sani, I. Sfiligoi, V. Sharma, S. Simon, E. Sudano, M. Tadel, Y. Tu, A. Vartak, S. Wasserbaech[48], F. Würthwein, A. Yagil, J. Yoo

University of California, Santa Barbara, Santa Barbara, U.S.A.

D. Barge, R. Bellan, C. Campagnari, M. D'Alfonso, T. Danielson, K. Flowers, P. Geffert, J. Incandela, C. Justus, P. Kalavase, S.A. Koay, D. Kovalskyi[1], V. Krutelyov, S. Lowette, N. Mccoll, V. Pavlunin, F. Rebassoo, J. Ribnik, J. Richman, R. Rossin, D. Stuart, W. To, J.R. Vlimant, C. West

California Institute of Technology, Pasadena, U.S.A.

A. Apresyan, A. Bornheim, J. Bunn, Y. Chen, E. Di Marco, J. Duarte, M. Gataullin, Y. Ma, A. Mott, H.B. Newman, C. Rogan, V. Timciuc, P. Traczyk, J. Veverka, R. Wilkinson, Y. Yang, R.Y. Zhu

Carnegie Mellon University, Pittsburgh, U.S.A.

B. Akgun, R. Carroll, T. Ferguson, Y. Iiyama, D.W. Jang, S.Y. Jun, Y.F. Liu, M. Paulini, J. Russ, H. Vogel, I. Vorobiev

University of Colorado at Boulder, Boulder, U.S.A.

J.P. Cumalat, M.E. Dinardo, B.R. Drell, C.J. Edelmaier, W.T. Ford, A. Gaz, B. Heyburn, E. Luiggi Lopez, U. Nauenberg, J.G. Smith, K. Stenson, K.A. Ulmer, S.R. Wagner, S.L. Zang

Cornell University, Ithaca, U.S.A.

L. Agostino, J. Alexander, A. Chatterjee, N. Eggert, L.K. Gibbons, B. Heltsley, W. Hopkins, A. Khukhunaishvili, B. Kreis, N. Mirman, G. Nicolas Kaufman, J.R. Patterson, A. Ryd, E. Salvati, W. Sun, W.D. Teo, J. Thom, J. Thompson, J. Vaughan, Y. Weng, L. Winstrom, P. Wittich

Fairfield University, Fairfield, U.S.A.

A. Biselli, G. Cirino, D. Winn

Fermi National Accelerator Laboratory, Batavia, U.S.A.

S. Abdullin, M. Albrow, J. Anderson, G. Apollinari, M. Atac, J.A. Bakken, L.A.T. Bauerdick, A. Beretvas, J. Berryhill, P.C. Bhat, I. Bloch, K. Burkett, J.N. Butler, V. Chetluru, H.W.K. Cheung, F. Chlebana, S. Cihangir, W. Cooper, D.P. Eartly, V.D. Elvira, S. Esen, I. Fisk, J. Freeman, Y. Gao, E. Gottschalk, D. Green, O. Gutsche, J. Hanlon, R.M. Harris, J. Hirschauer, B. Hooberman, H. Jensen, S. Jindariani, M. Johnson, U. Joshi, B. Klima, S. Kunori, S. Kwan, C. Leonidopoulos, D. Lincoln, R. Lipton, J. Lykken, K. Maeshima, J.M. Marraffino, S. Maruyama, D. Mason, P. McBride, T. Miao, K. Mishra, S. Mrenna, Y. Musienko[49], C. Newman-Holmes, V. O'Dell, J. Pivarski, R. Pordes, O. Prokofyev, T. Schwarz, E. Sexton-Kennedy, S. Sharma, W.J. Spalding, L. Spiegel, P. Tan, L. Taylor, S. Tkaczyk, L. Uplegger, E.W. Vaandering, R. Vidal, J. Whitmore, W. Wu, F. Yang, F. Yumiceva, J.C. Yun

University of Florida, Gainesville, U.S.A.

D. Acosta, P. Avery, D. Bourilkov, M. Chen, S. Das, M. De Gruttola, G.P. Di Giovanni, D. Dobur, A. Drozdetskiy, R.D. Field, M. Fisher, Y. Fu, I.K. Furic, J. Gartner, S. Goldberg, J. Hugon, B. Kim, J. Konigsberg, A. Korytov, A. Kropivnitskaya, T. Kypreos, J.F. Low, K. Matchev, P. Milenovic[50], G. Mitselmakher, L. Muniz, R. Remington, A. Rinkevicius, M. Schmitt, B. Scurlock, P. Sellers, N. Skhirtladze, M. Snowball, D. Wang, J. Yelton, M. Zakaria

2012 JINST 7 P10002

Florida International University, Miami, U.S.A.

V. Gaultney, L.M. Lebolo, S. Linn, P. Markowitz, G. Martinez, J.L. Rodriguez

Florida State University, Tallahassee, U.S.A.

T. Adams, A. Askew, J. Bochenek, J. Chen, B. Diamond, S.V. Gleyzer, J. Haas, S. Hagopian, V. Hagopian, M. Jenkins, K.F. Johnson, H. Prosper, S. Sekmen, V. Veeraraghavan, M. Weinberg

Florida Institute of Technology, Melbourne, U.S.A.

M.M. Baarmand, B. Dorney, M. Hohlmann, H. Kalakhety, I. Vodopiyanov

University of Illinois at Chicago (UIC), Chicago, U.S.A.

M.R. Adams, I.M. Anghel, L. Apanasevich, Y. Bai, V.E. Bazterra, R.R. Betts, J. Callner, R. Cavanaugh, C. Dragoiu, L. Gauthier, C.E. Gerber, D.J. Hofman, S. Khalatyan, G.J. Kunde[51], F. Lacroix, M. Malek, C. O'Brien, C. Silkworth, C. Silvestre, D. Strom, N. Varelas

The University of Iowa, Iowa City, U.S.A.

U. Akgun, E.A. Albayrak, B. Bilki[52], W. Clarida, F. Duru, S. Griffiths, C.K. Lae, E. McCliment, J.-P. Merlo, H. Mermerkaya[53], A. Mestvirishvili, A. Moeller, J. Nachtman, C.R. Newsom, E. Norbeck, J. Olson, Y. Onel, F. Ozok, S. Sen, E. Tiras, J. Wetzel, T. Yetkin, K. Yi

Johns Hopkins University, Baltimore, U.S.A.

B.A. Barnett, B. Blumenfeld, S. Bolognesi, A. Bonato, D. Fehling, G. Giurgiu, A.V. Gritsan, Z.J. Guo, G. Hu, P. Maksimovic, S. Rappoccio, M. Swartz, N.V. Tran, A. Whitbeck

The University of Kansas, Lawrence, U.S.A.

P. Baringer, A. Bean, G. Benelli, O. Grachov, R.P. Kenny Iii, M. Murray, D. Noonan, S. Sanders, R. Stringer, G. Tinti, J.S. Wood, V. Zhukova

Kansas State University, Manhattan, U.S.A.

A.F. Barfuss, T. Bolton, I. Chakaberia, A. Ivanov, S. Khalil, M. Makouski, Y. Maravin, S. Shrestha, I. Svintradze

Lawrence Livermore National Laboratory, Livermore, U.S.A.

J. Gronberg, D. Lange, D. Wright

University of Maryland, College Park, U.S.A.

A. Baden, M. Boutemeur, B. Calvert, S.C. Eno, J.A. Gomez, N.J. Hadley, R.G. Kellogg, M. Kirn, T. Kolberg, Y. Lu, M. Marionneau, A.C. Mignerey, A. Peterman, K. Rossato, P. Rumerio, A. Skuja, J. Temple, M.B. Tonjes, S.C. Tonwar, E. Twedt

Massachusetts Institute of Technology, Cambridge, U.S.A.

B. Alver, G. Bauer, J. Bendavid, W. Busza, E. Butz, I.A. Cali, M. Chan, V. Dutta, G. Gomez Ceballos, M. Goncharov, K.A. Hahn, Y. Kim, M. Klute, Y.-J. Lee, W. Li, P.D. Luckey, T. Ma, S. Nahn, C. Paus, D. Ralph, C. Roland, G. Roland, M. Rudolph, G.S.F. Stephans, F. Stöckli, K. Sumorok, K. Sung, D. Velicanu, E.A. Wenger, R. Wolf, B. Wyslouch, S. Xie, M. Yang, Y. Yilmaz, A.S. Yoon, M. Zanetti

2012 JINST 7 P10002

University of Minnesota, Minneapolis, U.S.A.

S.I. Cooper, P. Cushman, B. Dahmes, A. De Benedetti, G. Franzoni, A. Gude, J. Haupt, S.C. Kao, K. Klapoetke, Y. Kubota, J. Mans, N. Pastika, V. Rekovic, R. Rusack, M. Sasseville, A. Singovsky, N. Tambe, J. Turkewitz

University of Mississippi, University, U.S.A.

L.M. Cremaldi, R. Godang, R. Kroeger, L. Perera, R. Rahmat, D.A. Sanders, D. Summers

University of Nebraska-Lincoln, Lincoln, U.S.A.

E. Avdeeva, K. Bloom, S. Bose, J. Butt, D.R. Claes, A. Dominguez, M. Eads, P. Jindal, J. Keller, I. Kravchenko, J. Lazo-Flores, H. Malbouisson, S. Malik, G.R. Snow

State University of New York at Buffalo, Buffalo, U.S.A.

U. Baur, A. Godshalk, I. Iashvili, S. Jain, A. Kharchilava, A. Kumar, S.P. Shipkowski, K. Smith, Z. Wan

Northeastern University, Boston, U.S.A.

G. Alverson, E. Barberis, D. Baumgartel, M. Chasco, D. Trocino, D. Wood, J. Zhang

Northwestern University, Evanston, U.S.A.

A. Anastassov, A. Kubik, N. Mucia, N. Odell, R.A. Ofierzynski, B. Pollack, A. Pozdnyakov, M. Schmitt, S. Stoynev, M. Velasco, S. Won

University of Notre Dame, Notre Dame, U.S.A.

L. Antonelli, D. Berry, A. Brinkerhoff, M. Hildreth, C. Jessop, D.J. Karmgard, J. Kolb, K. Lannon, W. Luo, S. Lynch, N. Marinelli, D.M. Morse, T. Pearson, R. Ruchti, J. Slaunwhite, N. Valls, M. Wayne, M. Wolf, J. Ziegler

The Ohio State University, Columbus, U.S.A.

B. Bylsma, L.S. Durkin, C. Hill, P. Killewald, K. Kotov, T.Y. Ling, D. Puigh, M. Rodenburg, C. Vuosalo, G. Williams

Princeton University, Princeton, U.S.A.

N. Adam, E. Berry, P. Elmer, D. Gerbaudo, V. Halyo, P. Hebda, J. Hegeman, A. Hunt, E. Laird, D. Lopes Pegna, P. Lujan, D. Marlow, T. Medvedeva, M. Mooney, J. Olsen, P. Piroué, X. Quan, A. Raval, H. Saka, D. Stickland, C. Tully, J.S. Werner, A. Zuranski

University of Puerto Rico, Mayaguez, U.S.A.

J.G. Acosta, X.T. Huang, A. Lopez, H. Mendez, S. Oliveros, J.E. Ramirez Vargas, A. Zatserklyaniy

Purdue University, West Lafayette, U.S.A.

E. Alagoz, V.E. Barnes, D. Benedetti, G. Bolla, D. Bortoletto, M. De Mattia, A. Everett, L. Gutay, Z. Hu, M. Jones, O. Koybasi, M. Kress, A.T. Laasanen, N. Leonardo, V. Maroussov, P. Merkel, D.H. Miller, N. Neumeister, I. Shipsey, D. Silvers, A. Svyatkovskiy, M. Vidal Marono, H.D. Yoo, J. Zablocki, Y. Zheng

Purdue University Calumet, Hammond, U.S.A.

S. Guragain, N. Parashar

2012 JINST 7 P10002

Rice University, Houston, U.S.A.

A. Adair, C. Boulahouache, V. Cuplov, K.M. Ecklund, F.J.M. Geurts, B.P. Padley, R. Redjimi, J. Roberts, J. Zabel

University of Rochester, Rochester, U.S.A.

B. Betchart, A. Bodek, Y.S. Chung, R. Covarelli, P. de Barbaro, R. Demina, Y. Eshaq, A. Garcia-Bellido, P. Goldenzweig, Y. Gotra, J. Han, A. Harel, D.C. Miner, G. Petrillo, W. Sakumoto, D. Vishnevskiy, M. Zielinski

The Rockefeller University, New York, U.S.A.

A. Bhatti, R. Ciesielski, L. Demortier, K. Goulianos, G. Lungu, S. Malik, C. Mesropian

Rutgers, the State University of New Jersey, Piscataway, U.S.A.

S. Arora, O. Atramentov, A. Barker, J.P. Chou, C. Contreras-Campana, E. Contreras-Campana, D. Duggan, D. Ferencek, Y. Gershtein, R. Gray, E. Halkiadakis, D. Hidas, D. Hits, A. Lath, S. Panwalkar, M. Park, R. Patel, A. Richards, K. Rose, S. Salur, S. Schnetzer, C. Seitz, S. Somalwar, R. Stone, S. Thomas

University of Tennessee, Knoxville, U.S.A.

G. Cerizza, M. Hollingsworth, S. Spanier, Z.C. Yang, A. York

Texas A&M University, College Station, U.S.A.

R. Eusebi, W. Flanagan, J. Gilmore, T. Kamon[54], V. Khotilovich, R. Montalvo, I. Osipenkov, Y. Pakhotin, A. Perloff, J. Roe, A. Safonov, T. Sakuma, S. Sengupta, I. Suarez, A. Tatarinov, D. Toback

Texas Tech University, Lubbock, U.S.A.

N. Akchurin, C. Bardak, J. Damgov, P.R. Dudero, C. Jeong, K. Kovitanggoon, S.W. Lee, T. Libeiro, P. Mane, Y. Roh, A. Sill, I. Volobouev, R. Wigmans

Vanderbilt University, Nashville, U.S.A.

E. Appelt, E. Brownson, D. Engh, C. Florez, W. Gabella, A. Gurrola, M. Issah, W. Johns, P. Kurt, C. Maguire, A. Melo, P. Sheldon, B. Snook, S. Tuo, J. Velkovska

University of Virginia, Charlottesville, U.S.A.

M.W. Arenton, M. Balazs, S. Boutle, S. Conetti, B. Cox, B. Francis, S. Goadhouse, J. Goodell, R. Hirosky, A. Ledovskoy, C. Lin, C. Neu, J. Wood, R. Yohay

Wayne State University, Detroit, U.S.A.

S. Gollapinni, R. Harr, P.E. Karchin, C. Kottachchi Kankanamge Don, P. Lamichhane, M. Mattson, C. Milstène, A. Sakharov

University of Wisconsin, Madison, U.S.A.

M. Anderson, M. Bachtis, D. Belknap, J.N. Bellinger, J. Bernardini, L. Borrello, D. Carlsmith, M. Cepeda, S. Dasu, J. Efron, E. Friis, L. Gray, K.S. Grogg, M. Grothe, R. Hall-Wilton, M. Herndon, A. Hervé, P. Klabbers, J. Klukas, A. Lanaro, C. Lazaridis, J. Leonard, R. Loveless, A. Mohapatra, I. Ojalvo, G.A. Pierro, I. Ross, A. Savin, W.H. Smith, J. Swanson

2012 JINST 7 P10002

†: Deceased
1: Also at CERN, European Organization for Nuclear Research, Geneva, Switzerland
2: Also at National Institute of Chemical Physics and Biophysics, Tallinn, Estonia
3: Also at Universidade Federal do ABC, Santo Andre, Brazil
4: Also at California Institute of Technology, Pasadena, U.S.A.
5: Also at Laboratoire Leprince-Ringuet, Ecole Polytechnique, IN2P3-CNRS, Palaiseau, France
6: Also at Suez Canal University, Suez, Egypt
7: Also at Cairo University, Cairo, Egypt
8: Also at British University, Cairo, Egypt
9: Also at Fayoum University, El-Fayoum, Egypt
10: Now at Ain Shams University, Cairo, Egypt
11: Also at Soltan Institute for Nuclear Studies, Warsaw, Poland
12: Also at Université de Haute-Alsace, Mulhouse, France
13: Also at Moscow State University, Moscow, Russia
14: Also at Brandenburg University of Technology, Cottbus, Germany
15: Also at Institute of Nuclear Research ATOMKI, Debrecen, Hungary
16: Also at Eötvös Loránd University, Budapest, Hungary
17: Also at Tata Institute of Fundamental Research - HECR, Mumbai, India
18: Now at King Abdulaziz University, Jeddah, Saudi Arabia
19: Also at University of Visva-Bharati, Santiniketan, India
20: Also at Sharif University of Technology, Tehran, Iran
21: Also at Isfahan University of Technology, Isfahan, Iran
22: Also at Shiraz University, Shiraz, Iran
23: Also at Plasma Physics Research Center, Science and Research Branch, Islamic Azad University, Teheran, Iran
24: Also at Facoltà Ingegneria Università di Roma, Roma, Italy
25: Also at Università della Basilicata, Potenza, Italy
26: Also at Laboratori Nazionali di Legnaro dell' INFN, Legnaro, Italy
27: Also at Università degli studi di Siena, Siena, Italy
28: Also at Faculty of Physics of University of Belgrade, Belgrade, Serbia
29: Also at University of Florida, Gainesville, U.S.A.
30: Also at University of California, Los Angeles, Los Angeles, U.S.A.
31: Also at Scuola Normale e Sezione dell' INFN, Pisa, Italy
32: Also at INFN Sezione di Roma; Università di Roma "La Sapienza", Roma, Italy
33: Also at University of Athens, Athens, Greece
34: Also at Rutherford Appleton Laboratory, Didcot, United Kingdom
35: Also at The University of Kansas, Lawrence, U.S.A.
36: Also at Paul Scherrer Institut, Villigen, Switzerland
37: Also at Institute for Theoretical and Experimental Physics, Moscow, Russia
38: Also at Gaziosmanpasa University, Tokat, Turkey
39: Also at Adiyaman University, Adiyaman, Turkey
40: Also at The University of Iowa, Iowa City, U.S.A.
41: Also at Mersin University, Mersin, Turkey
42: Also at Kafkas University, Kars, Turkey
43: Also at Suleyman Demirel University, Isparta, Turkey
44: Also at Ege University, Izmir, Turkey
45: Also at School of Physics and Astronomy, University of Southampton, Southampton, United Kingdom

2012 JINST 7 P10002

46: Also at INFN Sezione di Perugia; Università di Perugia, Perugia, Italy
47: Also at University of Sydney, Sydney, Australia
48: Also at Utah Valley University, Orem, U.S.A.
49: Also at Institute for Nuclear Research, Moscow, Russia
50: Also at University of Belgrade, Faculty of Physics and Vinca Institute of Nuclear Sciences, Belgrade, Serbia
51: Also at Los Alamos National Laboratory, Los Alamos, U.S.A.
52: Also at Argonne National Laboratory, Argonne, U.S.A.
53: Also at Erzincan University, Erzincan, Turkey
54: Also at Kyungpook National University, Daegu, Korea

2012 JINST 7 P10002